Vz-GAL: Probing Cold Molecular Gas in Dusty Star-forming Galaxies at z=1-6

Citation for the original published paper (version of record):
Prajapati, P., Riechers, D., Cox, P. et al (2026). Vz-GAL: Probing Cold Molecular Gas in Dusty Star-forming Galaxies at z=1-6. Astrophysical Journal, Supplement Series, 282(2).
http://dx.doi.org/10.3847/1538-4365/ae27d4

The Astrophysical Journal Supplement Series, 282:40 (38pp), 2026 February https://doi.org/10.3847/1538-4365/ae27d4

Vz-GAL: Probing Cold Molecular Gas in Dusty Star-forming Galaxies at $z = 1$–6

Prachi Prajapati[1,2,22], Dominik Riechers[1], Pierre Cox[3], Axel Weiss[2], Amélie Saintonge[2], Bethany Jones[1], Tom J. L. C. Bakx[4], Stefano Berta[5], Paul van der Werf[6], Roberto Neri[5], Kirsty M. Butler[4], Asantha Cooray[7], Diana Ismail[8], Andrew J. Baker[9,10], Edoardo Borsato[11], Andrew Harris[12], Rob Ivison[13,14], Matthew Lehnert[3,15], Lucia Marchetti[16,17,18], Hugo Messias[19,20], Alain Omont[3], Catherine Vlahakis[21], and Chentao Yang[4]

[1] Institute for Astrophysics, University of Cologne, Zülpicher Straße 77, 50937 Cologne, Germany; prajapati@ph1.uni-koeln.de
[2] Max Planck Institute for Radio Astronomy (MPIfR), Auf dem Hügel 69, 53121 Bonn, Germany
[3] Sorbonne Université, Université Paris 6 and CNRS, Institut d'Astrophysique de Paris, 98 bis boulevard Arago, 75014 Paris, France
[4] Department of Space, Earth & Environement, Chalmers University of Technology, Chalmersplatsen 4, Gothenburg SE-412 96, Sweden
[5] Institut de Radioastronomie Millimétrique (IRAM), 300 rue de la Piscine, 38406, Saint-Martin-d'Hères, France
[6] Leiden Observatory, Leiden University, PO Box 9513, 2300 RA Leiden, The Netherlands
[7] University of California Irvine, Department of Physics & Astronomy, FRH 2174, Irvine, CA 92697, USA
[8] Université de Strasbourg, CNRS, Observatoire astronomique de Strasbourg, UMR 7550, 67000 Strasbourg, France
[9] Department of Physics and Astronomy, Rutgers University, New Brunswick, NJ 08854-8019, USA
[10] Department of Physics and Astronomy, University of the Western Cape, Bellville 7535, Cape Town, South Africa
[11] Dipartimento di Fisica e Astronomia "G. Galilei," Università di Padova, vicolo dell'Osservatorio 3, I-35122 Padova, Italy
[12] Department of Astronomy, University of Maryland, College Park, MD 20742, USA
[13] Institute for Astronomy, University of Edinburgh, Royal Observatory, Blackford Hill, Edinburgh EH9 3HJ, UK
[14] School of Cosmic Physics, Dublin Institute for Advanced Studies, 31 Fitzwilliam Place, Dublin D02 XF86, Ireland
[15] Université Lyon 1, ENS de Lyon, Centre de Recherche Astrophysique de Lyon (UMR5574), 69230, Saint-Genis-Laval, France
[16] Department of Astronomy, University of Cape Town, 7701 Rondebosch, Cape Town, South Africa
[17] INAF—Istituto di Radioastronomia, via Gobetti 101, I-40129 Bologna, Italy
[18] The Inter-University Institute for Data Intensive Astronomy (IDIA), Department of Astronomy, University of Cape Town, 7701 Rondebosch, Cape Town, South Africa
[19] European Southern Observatory, Alonso de Córdova 3107, Casilla 19001, Vitacura, Santiago, Chile
[20] Joint ALMA Observatory, Vitacura, Santiago 763-0355, Chile
[21] National Radio Astronomy Observatory, 520 Edgemont Road, Charlottesville, VA 22901, USA

Received 2025 September 25; revised 2025 November 24; accepted 2025 December 1; published 2026 January 23

Abstract

We present the first results of Vz-GAL, a high-redshift CO(J = 1–0) large survey with the Karl G. Jansky Very Large Array, targeting 92 Herschel-selected, infrared-luminous, dusty star-forming galaxies at redshifts 1–6. These sources are selected based on having redshifts and mid-/high-J CO transitions from the NOrthern Extended Millimeter Array z–GAL survey. We successfully detect CO(J = 1–0) emission in 90/92 galaxies at the expected positions and redshifts, including nine tentative detections at 2σ–3σ significance, and CO(J = 2–1) emission in 10 of these galaxies. The CO(J = 1–0) luminosities suggest apparent gas masses in the range $\mu M_{\rm H_2}$ = (2–20) × 10^{11} ($\alpha_{\rm CO}$/4.0) $M_\odot$, which implies gas depletion times of 50–600 Myr. These timescales show similar spread as local ULIRGs, suggesting a self-regulatory mechanism that maintains a consistent star formation rate per unit gas mass in starbursts across redshifts. To quantify the contribution of "excitation correction" factors to gas mass estimates, we calculate median CO line brightness temperature ratios of $r_{21} = 0.88 \pm 0.25$, $r_{31} = 0.61 \pm 0.22$, $r_{41} = 0.49 \pm 0.15$, $r_{51} = 0.47 \pm 0.13$, and $r_{61} = 0.28 \pm 0.13$. Accounting for these corrections results in a reduced scatter in "gas mass–star formation rate" relations. We also find a median log ($L'_{\rm [CI](^3P_1-^3P_0)}/L'_{\rm CO(J=1-0)}$) = -0.71 ± 0.12 for a subsample of 23 sources, consistent with the ratios derived for local star-forming galaxies. Together, our findings are in agreement with common conditions in the cold gas reservoirs among star-forming galaxies over a broad range in star formation modes, efficiencies, and scales.

Unified Astronomy Thesaurus concepts: High-redshift galaxies (734); Galaxy evolution (594); Starburst galaxies (1570); CO line emission (262); Molecular gas (1073); Interstellar medium (847); Star formation (1569)

Materials only available in the online version of record: machine-readable tables

1. Introduction

Submillimeter or infrared selected dusty star-forming galaxies (DSFGs) in the early Universe play a vital role in understanding galaxy formation and evolution. Many of these massive, dust-enshrouded systems—undergoing intense star formation—host infrared luminosities ($L_{8-1000\mu m}$) above 10^{12}–$10^{13} L_\odot$. While such infrared-luminous DSFGs are rare in the local Universe, they are relatively more abundant at high redshifts (high-z), contributing significantly to the comoving star formation rate density (SFRD) at its peak at redshift $z = 1$–3 (e.g., B. Magnelli et al. 2013; P. Madau & M. Dickinson 2014; N. Bourne et al. 2017; B. Hatsukade et al. 2018; J. A. Zavala et al. 2021). The understanding of these galaxies is therefore essential for exploring the processes that drive star formation and the role of dust in the early Universe (A. W. Blain et al. 2002; C. M. Casey et al. 2014; J. A. Hodge & E. da Cunha 2020).

---

[22] Doctoral Researcher at International Max Planck Research School (IMPRS) for Astronomy & Astrophysics.

Remarkably, the brightest DSFGs are typically triggered by major mergers (e.g., L. J. Tacconi et al. 2008; D. A. Riechers et al. 2017), which are short-lived, with starburst phases lasting about 100 Myr. During this period, their star formation rates (SFRs) can exceed 1000 $M_\odot$ yr^{-1} in the most exceptional cases, far surpassing most intensely star-forming galaxies in the local Universe; i.e., ultraluminous infrared galaxies (ULIRGs; D. B. Sanders & I. F. Mirabel 1996). The significant number of DSFGs at high redshifts, along with their diverse nature, makes it crucial to characterize their properties within the broader context of galaxy formation and evolution.

Observing the far-infrared spectral transitions of multiphase gas and the underlying continuum of DSFGs is of particular importance for understanding their obscured star formation. Star-forming activity is typically fueled by cold molecular gas reservoirs in galaxies (e.g., Y. Gao & P. M. Solomon 2004; S. Koyama et al. 2017; A. Saintonge & B. Catinella 2022). Alongside regulating the star formation, extended cold gas environments also influence the gas inflow and feedback processes within and around the galaxies. Molecular gas in local galaxies has an excellent probe of both the total star-forming gas masses extended over large spatial scales and the evolutionary mechanisms (e.g., A. K. Leroy et al. 2013; R. Genzel et al. 2015; A. Saintonge et al. 2017). Furthermore, the cold molecular gas history of the Universe has already been shown to reflect the evolution of the cosmic SFRD up to redshift 7 (see, e.g., D. A. Riechers et al. 2019; R. Decarli et al. 2020; F. Walter et al. 2020, for an overview). Therefore, studying the cold molecular gas of DSFGs at high-z is essential.

The most abundant molecule after molecular hydrogen, ^{12}C^{16}O (carbon monoxide; hereafter, CO) is a widely used tracer of molecular gas (i.e., H_2). The rotational ground-state transition, CO($J = 1 \rightarrow J = 0$), hereafter referred to as CO(1–0), is emitted by any molecular gas with densities $\gtrsim 10^2$ cm^{-3}. Even if the Boltzmann tail in the velocity distribution of the molecules ensures the presence of some molecules in higher-J states, these levels are significantly less populated than the ground state at lower densities. However, this may not be true for dense, highly excited environments, where the partition function is shifted toward higher-J levels. At high-z, the cosmic microwave background (CMB) also contributes in driving the partition function away from the prevailing conditions found in the local Universe (see details in E. da Cunha et al. 2013; K. C. Harrington et al. 2021).

Although challenging and limited to very few galaxies (C. L. Carilli et al. 2002; T. R. Greve et al. 2004; D. A. Riechers et al. 2006, 2009, 2010b) until the advent of the Karl G. Jansky Very Large Array (VLA) upgrade (e.g., R. J. Ivison et al. 2011; D. A. Riechers et al. 2011b, 2011c, 2011d; A. I. Harris et al. 2012; C. E. Sharon et al. 2016), observations of the CO(1–0) line ($\nu_{\rm rest} = 115.271$ GHz) are crucial to robustly calibrate total molecular gas masses using a CO–H_2 conversion factor, $\alpha_{\rm CO}$ (see Appendix A for more details). This conversion avoids an additional uncertainty related to the line excitation, which affects the higher-J CO lines. Furthermore, combining CO(1–0) data with higher-J CO transitions provides the anchor for studies of the gas excitation via the CO spectral line energy distribution (SLED) from which one can determine the physical properties of the molecular gas including its kinetic temperature and density (e.g., A. Weiß et al. 2005b, 2007; D. A. Riechers et al. 2006, 2010b, 2013; J. S. Spilker et al. 2014; C. Yang et al. 2017; K. C. Harrington et al. 2021, 2025). Such modeling can further benefit from observations of the atomic carbon fine-structure transitions, namely [CI](1−0) and [CI](2−1), to better constrain the excitation conditions in these extreme sources (e.g., G. Gururajan et al. 2023; M. Frias Castillo et al. 2024).

Most studies of the molecular gas in high-z galaxies to date are based on mid- to high-J CO lines (e.g., F. Valentino et al. 2020; S. Berta et al. 2023; M. Hagimoto et al. 2023), which limits our understanding of the cold gas reservoirs due to the lack of systematic CO(1–0) observations. Following a pilot program that targeted 14 galaxies (F. Stanley et al. 2023), we have therefore taken up a CO(1–0) large survey, VLA Vz-GAL, targeting 92 Herschel-selected DSFGs at redshifts between 1 and 6. All 106 of these galaxies have higher-J CO line observations and robust spectroscopic redshifts from the NOrthern Extended Millimeter Array (NOEMA) z–GAL program (R. Neri et al. 2020; P. Cox et al. 2023).

In Section 2, we describe the observations and data reduction. In Section 3, we report the CO(1–0) spectra, total intensity maps, and integrated properties of the line and underlying continuum. This section also includes additional CO(2–1) results of 10 targets. Section 4 discusses the implications of these results, in particular, addressing total molecular gas masses, depletion times, gas-to-dust mass comparison, and CO line ratios. We also compare [CI](1−0) to CO(1–0) line luminosities for 23 DSFGs with available [CI] observations from the z–GAL (R. Neri et al. 2020; P. Cox et al. 2023). Finally, Section 5 summarizes the main findings of this paper and highlights the scope to utilize this large sample for a number of studies in the future.

A spatially flat Lambda cold dark matter cosmology with $H_0 = 67.4$ km s^{-1} Mpc^{-1}, $\Omega_{\rm M} = 0.315$, and $\Omega_\Lambda = (1 - \Omega_{\rm M})$ has been adopted in the calculation of luminosity distances (D_L) throughout this paper (Planck Collaboration et al. 2020).

2. Sample, Observations, and Data

Large surveys over the past 15 yr have significantly increased the number of detections of DSFGs. In particular, the Herschel Space Observatory (G. L. Pilbratt et al. 2010) conducted extensive surveys at 70–500 μm, covering over 1000 deg^2, leading to the discovery of several hundreds of thousands of DSFGs (S. Eales et al. 2010; D. Lutz et al. 2011; S. J. Oliver et al. 2012; M. P. Viero et al. 2014; H. Nayyeri et al. 2016a; T. J. L. C. Bakx et al. 2018; B. A. Ward et al. 2022). In addition, other surveys such as the all-sky Planck-HFI (R. Cañameras et al. 2015; Planck Collaboration et al. 2015) and the South Pole Telescope (SPT) surveys (J. D. Vieira et al. 2010; J. E. Carlstrom et al. 2011; A. Weiß et al. 2013) have uncovered additional sources at the bright end of the same population.

Accurate spectroscopic redshifts are essential for conducting detailed follow-up studies of multiphase gas in high-z DSFGs. Since the first detections of submillimeter galaxies (SMGs) and thanks to extensive efforts from various research groups using ground-based submillimeter facilities, spectroscopic redshifts for about 400 DSFGs are now available, spanning a wide range from $1.5 < z < 7$ (e.g., T. R. Greve et al. 2005; A. Weiß et al. 2009; F. Walter et al. 2012; D. A. Riechers et al. 2013, 2010a, 2017, 2021; R. Cañameras et al. 2015; R. Neri et al. 2020; C. Reuter et al. 2020; K. C. Harrington et al. 2021; S. A. Urquhart et al. 2022; P. Cox et al. 2023, and references therein).

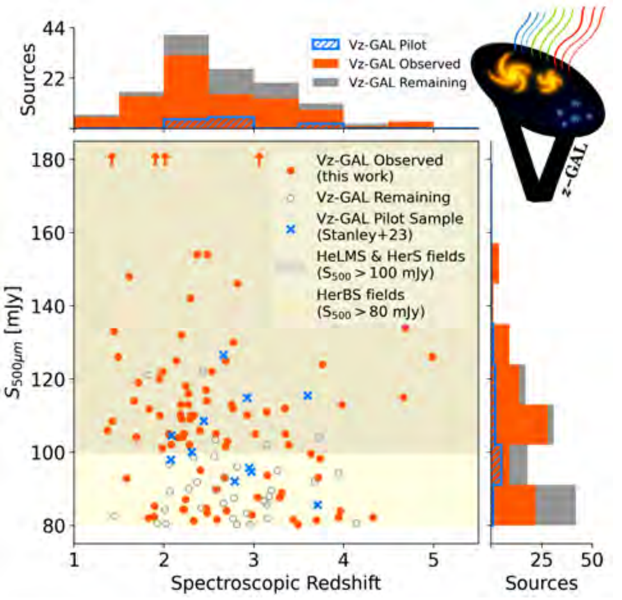

Figure 1. Herschel/SPIRE 500 μm flux densities ($S_{500\mu m}$) of the Vz-GAL DSFGs (this work) compared to the pilot program (F. Stanley et al. 2023) with respect to their spectroscopic redshifts based on the z–GAL project. We show only 11 data points, although the pilot sample contains 14 DSFGs, because HerBS-43, HerBS-70, and HerBS-95 each consist of two spatial components that are unresolved in the Herschel data. The histograms show fluxes of the Vz-GAL sample; shown in gray are the remaining observations not executed to date. In the central portion, the filled area in silver ($S_{500\mu m} > 100$ mJy) indicates the flux selection criteria for the HeLMS and HerS targets. The area in yellow (i.e., $S_{500\mu m} > 80$ mJy) shows the lower flux cut that was used to select the HerBS sources. Orange data points and arrows (the latter for $S_{500\mu m} > 180$ mJy) represent sources from this work in comparison to the DSFGs from pilot sample shown as blue crosses. Sources not yet observed are mostly in the $S_{500\mu m} = 80$–100 mJy regime and hence selected from the GAMA fields. This incompleteness is largely due to scheduling restrictions in certain LST ranges and thus random beyond the $S_{500\mu m}$ distribution. As a result, based on the homogeneous selection of the parent sample, the survey is representative and nearly complete down to $S_{500\mu m} = 100$ mJy, while the redshift–$S_{500\mu m}$ space is relatively evenly incomplete in the $S_{500\mu m} = 80$–100 mJy regime based on the observations not yet executed.

2.1. NOEMA z–GAL Spectroscopic Survey

The NOEMA z–GAL project (R. Neri et al. 2020; P. Cox et al. 2023) is to date the largest spectroscopic redshift survey of high-z DSFGs, having measured redshifts for 135 DSFGs based on mid to high-J CO transitions, mainly from CO(2−1) to CO(5−4), with some sources seen in [CI] and H_2O emission lines. These submillimeter/infrared bright galaxies ($L_{8-1000\mu m} \gtrsim 10^{12.5} L_\odot$) were originally selected based on simple flux cuts of the Herschel 500 μm flux density ($S_{500\mu m}$; Figure 1) of the HerMES Large Mode Survey and Stripe 82 Survey (HeLMS and HerS; H. Nayyeri et al. 2016a) and the Herschel Bright Sources sample (HerBS) detected in the H-ATLAS survey (T. J. L. C. Bakx et al. 2018). These selection criteria were $S_{500\mu m} \geqslant 100$ mJy for the HeLMS and HerS galaxies, and $S_{500\mu m} \geqslant 80$ mJy for the HerBS sources, respectively, after the removal of known low-redshift and nonthermal sources. The sample is complete in the selected fields, with the exception of sources for which redshifts were already known at the time z–GAL was initiated.

Detailed studies of selected sources in the parent sample from which the z–GAL sample was drawn have revealed a large diversity, e.g., numerous lensed galaxies (e.g., M. Negrello et al. 2010, 2017; A. Conley et al. 2011; D. A. Riechers et al. 2011c; R. S. Bussmann et al. 2013, 2015; J. L. Wardlow et al. 2013; H. Nayyeri et al. 2016b; T. J. L. C. Bakx et al. 2020b), active galactic nuclei (AGNs; e.g., F. Stanley et al. 2023), hyperluminous galaxies with luminosities exceeding 10^{13} $L_\odot$ (e.g., R. J. Ivison et al. 2013; D. A. Riechers et al. 2013, 2017; I. Oteo et al. 2016), and plausible galaxy mergers and protocluster environments (e.g., D. A. Riechers et al. 2014; R. S. Bussmann et al. 2015; I. Oteo et al. 2018; C. Gómez-Guijarro et al. 2019; T. J. L. C. Bakx et al. 2024). Similar discoveries were made in the Planck and SPT samples (e.g., R. Cañameras et al. 2015; J. S. Spilker et al. 2016; K. C. Harrington et al. 2017; T. B. Miller et al. 2018; N. Sulzenauer et al. 2025), with differences in the relative distributions that can likely be explained due to the different selection functions.

The spectroscopic redshifts of the z–GAL sources are in the range $1 < z < 6$ with a median value of $z = 2.56 \pm 0.10$ (P. Cox et al. 2023), centered approximately on the peak epoch of "galaxy growth" with the highest SFR per unit comoving volume. These data served as a foundation for studies reporting on the dust properties of the DSFGs and their evolution with redshift (D. Ismail et al. 2023), and the physical properties of the galaxies using higher-J CO lines (S. Berta et al. 2023). However, in order to obtain a better understanding of the physical conditions of the cold molecular gas in these DSFGs, measurements of the CO(1–0) emission line are essential as reported here.

2.2. VLA Vz-GAL CO(1–0) Sample Selection, Observations, and Data

Using the NSF's K. G. Jansky VLA, a first study of the CO(1–0) emission in 14 DSFGs (`VLA/20A-083`; PI: Riechers) in the redshift range $2 < z < 4$, from the z–GAL pilot sample (R. Neri et al. 2020), was conducted by F. Stanley et al. (2023). We here present the results of the continuation of this effort as a VLA Large Program, Vz-GAL,[23] to measure molecular gas in the entire z–GAL sample as traced by CO(1–0) transition, and also observe CO(2–1) for the z–GAL targets beyond $z = 3.6$.

The observations presented here as part of the Vz-GAL large program (`VLA/23B-169` and `VLA/25A-099`; PI: Riechers) were carried out during semesters 2023B and 2025A. In total, we observed 92/135 bright, dusty galaxies with over 210 hr of VLA integration time. Together with the 14 DSFGs from the pilot sample (F. Stanley et al. 2023), this covers 106/135 z–GAL sources in CO(1–0) emission line and the underlying continuum. Observations of the remaining sources were not executed to date and, hence, will be the focus of future efforts. The Vz-GAL targets were selected from the z–GAL sample and, therefore, follow the same selection criteria, with the only additional constraint of the sources not yet observed (see Figure 1).

Together with the targets of the pilot project, the sample of high-z galaxies presented in this paper quintuples the existing CO(1–0) detections of Herschel-selected bright DSFGs with $S_{500\mu m} \geqslant 80$ mJy, including lensed galaxies (22 sources in total; D. A. Riechers et al. 2011c, 2013; A. I. Harris et al. 2012; H. Fu et al. 2013; R. J. Ivison et al. 2013; T. K. D. Leung et al. 2019; T. J. L. C. Bakx et al. 2020a) and is equivalent to the total number of available CO(1–0) detections for high-z

---

[23] Vz-GAL website: https://vzgal.uni-koeln.de/

DSFGs spread across more heterogeneous samples (e.g., R. J. Ivison et al. 2011; D. A. Riechers 2011, 2011e; M. Aravena et al. 2016; C. E. Sharon et al. 2016; K. C. Harrington et al. 2019; M. Frias Castillo et al. 2023, and references therein). Many from such heterogeneous samples are JCMT/SCUBA or SCUBA-2 selected DSFGs (e.g., unlensed dusty galaxies with $S_{850\mu\mathrm{m}} > 7.5$ mJy from M. Frias Castillo et al. 2023).

To maximize detection efficiency by minimizing phase noise and source resolution, we used the most compact D configuration[24] of the VLA to observe the CO(1–0) emission line in the selected dusty galaxies. Their robust spectroscopic redshifts of $1.4 < z < 5.4$ are covered using the `Ku` (2 cm), `K` (1 cm), `Ka` (0.9 cm), and `Q` (0.7 cm) band receivers of the VLA. We also utilized our remaining, approved time for 2025A in its subsequent semester (with C configuration) to repeat the CO(1–0) observations for two of the sources, namely HeLMS-57 and HerBS-204, to improve their signal-to-noise ratio (SNR) after combination with the previously observed D array data.

Furthermore, we observed 10 of these Vz-GAL galaxies at redshifts $z > 3.6$ in CO(2–1) ($\nu_{\mathrm{rest}} = 230.542$ GHz), using the VLA `Ka/Q` band receivers. These are all z–GAL sources where such observations are possible with the VLA at reasonable system temperatures. The WIDAR correlator was configured in 8-bit mode to maximize line sensitivity, achieving 2 MHz spectral resolution ($\sim$12–36 km s^{-1} per channel across different bands) in dual polarization over a 2 GHz bandwidth. Exposure times were optimized for line detections and not for the underlying continuum. The desired spectral line in each observation set was typically centered in one of the 128 MHz sub-bands of 1 GHz intermediate frequency (IF) bands/sessions, with the second IF band placed either adjacent to the first one for enhancing continuum sensitivity or at a sufficiently different frequency for measuring the spectral index or covering other faint lines. Throughout this paper, we use the acronym IF1 for the IF band at lower frequencies and IF2 for the other one.

Standard VLA flux/bandpass calibrators (3C48, 3C138, 3C147, and 3C286) were used to perform flux calibration. Note that during the observations, quasar 3C138 was in a flaring state, which affected one set of observations (see Section 3.1). Phase calibrators in the proximity of respective science targets were selected from the VLA calibrator catalog.

3. Data Reduction and Measurements

3.1. Data Reduction

The data were reduced, calibrated, and imaged using `CASA v6.4.1` (J. P. McMullin et al. 2007) on two high-performance computers in Cologne, namely CHEOPS[25] and RAMSES.[26] Manual flagging was necessary to remove radio frequency interference, bad baselines, and nonfunctional antennas for all sources. The measured flux densities of the flux calibrators agreed with their R. A. Perley & B. J. Butler (2017) models to within 10%–15% accuracy. However, the flaring flux calibrator 3C138 affected CO(1–0) observation of HerS-11, one of the DSFGs from our sample. To correct for this, we rescaled its observed flux densities using `getcalmodvla`[27] in `CASA v6.7`.

Following the calibration process, we split apart the calibrated target data from calibrators using the `CASA` task `split`. We generated spectral cubes for each of the targets and manually cleaned their integrated-intensity (moment-0) maps using `tclean`. The default baseline weighting scheme, `natural`, was used in `tclean` and the data were averaged to a resolution of 6 MHz (on average $\sim$60 km s^{-1}). The CO emission of our targets is mostly unresolved or only marginally resolved (see Section 3.2), with angular resolutions between $1\farcs2$ and $5\farcs2$. Our observations for objects that required long exposure times were divided into multiple sets, which we combined using `concat` to improve the SNR while imaging. For HeLMS-57 and HerBS-204, the D- and additional C-configuration data were combined using `concat` after being `split` with a common uv-range of 0–125 $k\lambda$ and 0–82 $k\lambda$, respectively. This step ensured that the spatial scales were matched between the two array setups, and the SNR was improved across the combined datasets. Although retaining the full uv-range of C-array data might have led to better angular resolution, we noticed the increased noise due to phase instability for the longer baselines, leading us to combine only the common uv-range.

Continuum subtraction was performed using `uvcontsub`, and clean continuum maps were generated in multifrequency synthesis (`mfs`) mode of `tclean` using line-free channels for the sources with continuum detections over $2\sigma_c$, where σ_c is the rms noise across the averaged bandwidth. For targets with continuum detections in both IF1 and IF2, we combined the line-free channels from both IFs to create a continuum map at the mean central frequency of both using the `tclean mfs` mode. We further use the `CASA` 2D Gaussian fitting task `imfit` to estimate the total continuum flux densities for cases with continuum above $2\sigma_c$ (see the tables in Appendix A). For nondetections with SNR below 2, we provide $3\sigma_c$ upper limits using the clean continuum maps, assuming the emission to be unresolved. Please refer to Appendix A for details on continuum measurements.

3.2. CO Spectral Line Measurements

We partially resolve some lensed DSFGs and systems with multiple galaxies at the same spectroscopic redshift in the VLA data—see the list of these sources and details in Appendix B. Therefore, we choose two different methods to extract the spectra: (i) peak pixel spectrum extraction for unresolved targets, and (ii) 2σ contours based extraction for resolved systems—σ being the rms noise of the moment-0 map—as this level is high enough to limit noise contamination while still inclusive enough to capture faint, extended line emission that would be systematically missed at more conservative thresholds. For case (ii), we iterated the flux extraction process for defining the extraction region used. Here, the initial spectra are extracted from a large circular aperture centered on the z–GAL based target coordinates, encompassing the source emission. We defined line channels to be used for the moment-0 maps from here. Having the map created using `CARTA v4.1.0` (A. Comrie et al. 2024), we redefined the extraction regions based on its 2σ contours and

---

[24] https://science.nrao.edu/facilities/vla/docs/manuals/oss/performance/resolution

[25] https://itcc.uni-koeln.de/hpc/hpc/technische-details

[26] https://itcc.uni-koeln.de/hpc/hpc/ramses

[27] https://casadocs.readthedocs.io/en/latest/api/tt/casatasks.calibration.getcalmodvla.html

repeated the steps until the 2σ contours converged. Finally using `CASA tclean`, we created total intensity (moment-0) maps directly from the `split` target visibilities for all DSFGs, regardless of their different spectral extraction methods.

The CO(1–0) and CO(2–1) moment-0 maps of all of the V*z*-GAL sources are presented in Appendix B. Of the 92 DSFGs covered by the observations, CO(1–0) emission is detected at $>5\sigma$ significance for 57 targets, at $>3\sigma$ significance for 81 targets, and $>2\sigma$ significance for 90 targets. We consider the nine sources recovered at 2σ–3σ significance to be tentative detections, but due to the known redshifts and positions, the probability of false positives is low compared to random 2σ–3σ peaks in the data cubes. Statistically, we expect less than one false detection among these tentative identifications, but more sensitive observations are required to confirm them. The remaining two sources—HeLMS-44 ($z = 1.37$) and HerBS-53 ($z = 1.42$)—show no significant emission, with CO(1–0) signal levels below 2σ in the VLA `Q` band. These nondetections are due to high noise at their redshifted CO(1–0) frequencies near the upper edge of the 40–50 GHz band.

Three sources with multiple spatial components (HerBS-109, HerBS-187, and HerBS-194) show only a partial CO(1–0) detection; i.e., we detected only one of their components above 2σ level. Please note that HerBS-109 does not have available infrared luminosity (S. Berta et al. 2023), and out of its three spatial components, we only detected the southern one. Although we provide the CO(1–0) line properties of its southern component in Appendix A, we avoid using this target in the analyses presented in Section 4. Otherwise, the statistical results in Section 4 incorporate limits from all of the partial- and nondetections, wherever relevant.

Furthermore, all 10 DSFGs with additional CO(2–1) data (HeLMS-19, HeLMS-24, HeLMS-27, HeLMS-36, HeLMS-45, HerS-11, HerBS-78, HerBS-177, HerBS-179, and HerBS-185) were successfully detected with at least an SNR of 3, with only HeLMS-27 and HerBS-179 showing tentative 2σ–3σ detections.

Besides moment-0 maps, we show in Appendix B the CO line spectra and their Gaussian fits for all 92 targets. We compare these spectra to higher-*J* CO lines detected with NOEMA (P. Cox et al. 2023) for each source. As no mid-/high-*J* CO lines were previously detected for HeLMS-49, we instead compare the CO(1–0) line profile with that of [CI](1–0). Approximately 30% of the sources show double-peaked line profiles. Among these, the sources with significant overlap between two fitted Gaussian profiles show the extracted flux values to be consistent (within error bars) with those derived using only a single Gaussian fit to the same profile. We choose to use the results of a single Gaussian fit in these cases to avoid larger uncertainties on the integrated line fluxes due to more fitting parameters. However, for sources with well-separated peaks—velocity separation $(v_2 - v_1) \geqslant 1.25 \times \sqrt{{\sigma_1}^2 + {\sigma_2}^2}$)—we fit them with two separate Gaussian profiles and sum their fluxes to derive the total line flux. Here, σ_1 and σ_2 are the standard deviations of two Gaussians fitted to two different line components of a double-peaked profile. The integrated properties of the measured CO(1–0) and CO(2–1) spectra are listed in Appendix A.

Overall, the CO(1–0) line profiles have consistent widths and shapes with those seen at higher-*J* CO levels. Qualitative notes on individual galaxies with differences in this comparison (e.g., HerS-13) and with newly resolved spatial components (e.g., HeLMS-32) are given in Appendix B.

3.2.1. CO Line Luminosity and Gas Mass Derivation

To date, integrated CO(1–0) line luminosities, $L'_{\mathrm{CO(1-0)}}$, have been used in the literature for robustly calibrating total molecular gas masses, $M_{\mathrm{H_2}}$, for targets with unknown excitation conditions. With CO(1–0) observations, we avoid uncertainties related to the conversion from higher-*J* CO emission lines to the ground state. Relations between the observables and these physical quantities used in our calculation are as follows (see P. M. Solomon et al. 1997, for details):

$$L'_{\mathrm{CO}} = 3.25 \times 10^7 \times \frac{I_{\mathrm{CO}} \cdot {D_L}^2}{\nu^2_{\mathrm{CO,rest}} \cdot (1+z)}\ [\mathrm{K\ km\ s^{-1}\ pc^2}] \quad (1)$$

$$M_{\mathrm{H_2}} = \alpha_{\mathrm{CO}} \times L'_{\mathrm{CO(1-0)}}\ [M_\odot] \quad (2)$$

where, $I_{\mathrm{CO}} = S_{\mathrm{peak}}\Delta v$ is the measured CO line flux in Jy km s^{-1}, D_L is the luminosity distance in Mpc, $\nu_{\mathrm{CO,rest}}$ is the rest frequency of the CO line in GHz, and α_{CO} is the CO–H$_2$ conversion factor. Here, Δv and S_{peak} are the FWHM and peak intensity of the spectral line, respectively. For double-peaked spectra, we adopt the net FWHM as following:

$$\text{net FWHM} = \Delta s + [0.5 \times (\Delta v_1 + \Delta v_2)] \quad (3)$$

where Δs is the separation between two fitted Gaussians of a double-peaked line. Further, Δv_1 and Δv_2 are their respective FWHMs. In such cases, the S_{peak} of the double-Gaussian line fit corresponds to the derived total line flux divided by the net FWHM.

Using this robustly calibrated relation, we list the $L'_{\mathrm{CO(1-0)}}$ and the derived gas masses adopting a Milky Way–like α_{CO} of 4 $M_\odot$ (K km s^{-1} pc^2)$^{-1}$ in Appendix A. From now on, we will refer to the α_{CO} value without the units attached, for the ease of reading. We discuss the choice of adopting the Milky Way–like conversion factor in Appendix A.

As we do not have derived values for the lensing magnification factor μ for the full sample, we report the line luminosities and gas masses of all of the sources without applying a correction for μ. However, we indicate the "candidate" lensed DSFGs with a special marker in the tables in the Appendix A.

The V*z*-GAL DSFGs have CO(1–0) line luminosities in the range $\mu L'_{\mathrm{CO(1-0)}} \sim (0.5 - 5) \times 10^{11}$ K km s^{-1} pc^2, and have gas masses $\mu M_{\mathrm{H_2}}$ ranging from 2×10^{11} $(\alpha_{\mathrm{CO}}/4.0)\,M_\odot$ to 20×10^{11} $(\alpha_{\mathrm{CO}}/4.0)\,M_\odot$. For the sake of completeness, we also tabulate these properties for the DSFGs from the V*z*-GAL pilot program (F. Stanley et al. 2023), adopting the same α_{CO} conversion factor (see Appendix A).

4. Results and Discussion

In this section, we present the implications of the CO(1–0) results discussing first the correlation between the total infrared and CO line luminosities (Sections 4.1 and 4.2), followed by the redshift evolution of the gas depletion time presented in Section 4.3. Further, we combine our CO(1–0) and CO(2–1) results with the mid-/high-*J* CO transitions from P. Cox et al. (2023) to calculate the CO line ratios (Section 4.4). Here we also derive empirical relations between the CO(1−0), CO(2−1), and CO(3−2) line luminosities to

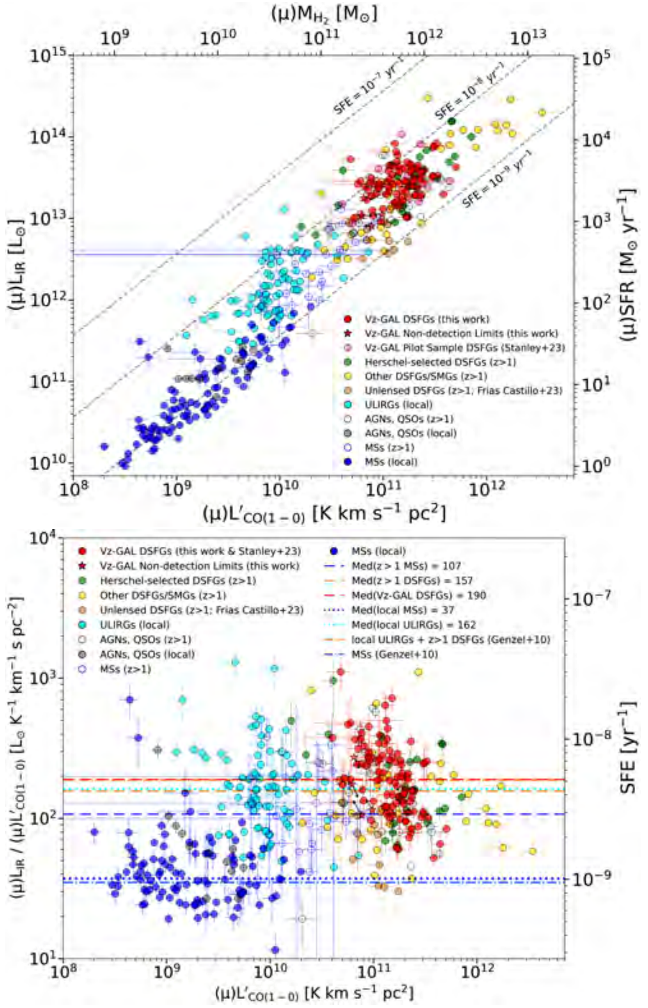

Figure 2. Upper panel: a proxy for the Kennicutt–Schmidt (K-S) relation of the Vz-GAL sample in terms of the infrared (8–1000 μm) luminosity ($L_{\rm IR}$; S. Berta et al. 2023) and the CO(1–0) line luminosity ($L'_{\rm CO(1-0)}$; see this work and F. Stanley et al. 2023). Dashed diagonals present constant star formation efficiency (SFE) lines with SFR [$M_\odot$ yr^{-1}] = 1.09 × $10^{-10} L_{\rm IR}[L_\odot]$ and $\alpha_{\rm CO} = 4\,M_\odot$ (K km s^{-1} pc^2)$^{-1}$. Here, we highlight the Vz-GAL pilot sample from F. Stanley et al. (2023) separately to illustrate its consistency with our measurements. However, in the subsequent statistical analyses and corresponding figures, the 14 pilot galaxies are combined with our 92 DSFGs and treated as a single, unified Vz-GAL sample. Lower panel: ratio of the infrared to CO(1–0) luminosity, a proxy for star formation efficiency (SFE), vs. the CO line luminosity (without lensing correction) as a probe for molecular gas mass. Relations derived by R. Genzel et al. (2010) are shown with dashed–dotted lines for comparison, upscaling their far-infrared luminosities $L_{\rm FIR}$ (50–300 μm) to $L_{\rm IR}$ (8–1000 μm) using $L_{\rm IR}/L_{\rm FIR} \sim 1.3$ (J. Graciá-Carpio et al. 2008) to match our plot. In both panels, we also show literature data points with available CO(1–0) observations: high-z Herschel-selected DSFGs (D. A. Riechers et al. 2011c; A. I. Harris et al. 2012; H. Fu et al. 2013; R. J. Ivison et al. 2013; K. C. Harrington et al. 2019; T. K. D. Leung et al. 2019; T. J. L. C. Bakx et al. 2020a), other distant DSFGs and submillimeter galaxies (SMGs; T. R. Greve et al. 2004; D. A. Riechers et al. 2008, 2011a, 2011b, 2013; C. L. Carilli et al. 2010; A. I. Harris et al. 2010; R. J. Ivison et al. 2011; B. H. C. Emonts et al. 2011, 2014; A. M. Swinbank et al. 2011; A. P. Thomson et al. 2012; C. E. Sharon et al. 2013, 2015, 2016; M. Aravena et al. 2016; K. C. Harrington et al. 2017; H. Dannerbauer et al. 2019; M. Frias Castillo et al. 2023), high-z AGNs/QSOs (C. L. Carilli & A. W. Blain 2002; G. F. Lewis et al. 2002; D. A. Riechers et al. 2006, 2009, 2011a, 2020; M. Aravena et al. 2008; J. Wagg et al. 2010; J.-F. Lestrade et al. 2011; C. E. Sharon et al. 2016), distant MS galaxies (M. Aravena et al. 2012, 2014; G. Rudnick et al. 2017; C. Gómez-Guijarro et al. 2019; M. Kaasinen et al. 2019; D. A. Riechers et al. 2020), local ULIRGs (P. M. Solomon et al. 1997; A. Chung et al. 2009; F. Combes et al. 2011; A. Gowardhan et al. 2018), and nearby massive MS galaxies ($M_* > 10^{10}\,M_\odot$; J. E. Geach et al. 2011; A. Saintonge et al. 2017; V. Villanueva et al. 2017; L. Dunne et al. 2021).

compare our statistical trends in scaling relations with those derived using the z–GAL data. Finally, Section 4.5 presents the gas-to-dust mass ratios of our sample, and Section 4.6 explores a correlation between the line luminosities of [CI](1−0) and CO(1−0). We summarize this discussion by listing the physical conditions of the interstellar medium (ISM) under which the calibration of total molecular gas masses, based only on CO(1–0) observations, might be challenging (Section 4.7).

4.1. $L'_{\rm CO(1-0)} - L_{\rm IR}$ Correlation

The Kennicutt–Schmidt (K-S) relation or star formation law in galaxies is defined as the relation between the gas surface density and the SFR surface density (M. Schmidt 1959; R. C. Kennicutt 1989). For most of the high-z galaxies with unavailable spatially resolved observations, a comparison between the integrated $L'_{\rm CO}$ (as a proxy for $M_{\rm gas}$) and total infrared luminosity ($L_{\rm IR}$, a proxy for SFR) serves as a proxy for the K-S relation. Although the $L'_{\rm CO} - L_{\rm IR}$ correlation is not strictly the same as the K-S law, it is beneficial to check the scaling relation over a large redshift range. Based solely on observables, the relative positions of different galaxy populations in this diagram provide qualitative insights into underlying physical conditions—such as variations in gas and dust temperatures and densities. The trends in CO–H$_2$ conversion factor ($\alpha_{\rm CO}$), hypothesized to depend on these physical properties, can also be qualitatively discussed using this correlation. In the literature, $\alpha_{\rm CO}$ has commonly been adopted with a bimodal distribution (see details in Appendix A).

The total infrared luminosities ($L_{\rm IR}$; 8–1000 μm) used in this work are derived by integrating a modified blackbody (MBB) function. In a preceding z–GAL paper, S. Berta et al. (2023) transformed the Herschel- and NOEMA-observed 50–1000 μm luminosities (D. Ismail et al. 2023) of our DSFGs into 8–1000 μm luminosities using $L_{50-1000\mu{\rm m}}/L_{8-1000\mu{\rm m}} = 0.7 \pm 0.1$. These 8–1000 μm infrared luminosities ($L_{\rm IR}$), which are connected to SFRs and/or dust temperatures, have been used in all of the upcoming analyses.

Figure 2 presents the distribution in the $L'_{\rm CO(1-0)} - L_{\rm IR}$ plane of all of the Vz-GAL DSFGs, including the sources from the pilot program (F. Stanley et al. 2023). For comparison, we added nearby and high-z galaxies from the literature with available CO(1–0) observations (see caption of Figure 2 for references). There appears to be a systematic offset in the $L_{\rm IR}/L'_{\rm CO(1-0)}$ ratios between SFR−M_* main-sequence (MS) galaxies at low and high redshifts, local ULIRGs, and distant DSFGs. This ratio is a proxy for SFR per unit gas mass (i.e., star formation efficiencies, SFEs), and such an offset may suggest differences in their SFEs (and/or dust temperatures assuming the same gas mass; see G. E. Magdis et al. 2012). On the other hand, the overall trend across statistically significant samples remains relatively smooth without evidence for a clear bimodality. High-z DSFGs follow similar SFE lines and spread as local ULIRGs (upper panel of Figure 2), perhaps implying comparable gas/dust temperatures and densities, and conditions that are more extreme than those in MS galaxies. This likely reflects their denser star-forming regions and more intense radiation fields associated with starburst activity, which result in warmer dust temperatures, higher $L_{\rm IR}$, and elevated SFEs compared to local disks (e.g., D. A. Riechers et al. 2021). Thus, the observed distributions in Figure 2 (upper panel) do not provide evidence for assuming a bimodal conversion factor rather than continuous variation in $\alpha_{\rm CO}$

across these populations, driven by their underlying physical conditions. They, however, also cannot rule out a constant $\alpha_{\rm CO}$.

In Figure 2 (lower panel), we examine the $L_{\rm IR}/L'_{\rm CO(1-0)}$ ratio, a proxy for SFE, as a function of $L'_{\rm CO(1-0)}$ to further explore the observed offset. This ratio reflects variations in gas density and temperature across galaxy populations, which in turn may affect the $\alpha_{\rm CO}$. Here, although the $L_{\rm IR}/L'_{\rm CO(1-0)}$ ratio is independent of the lensing magnification factor (μ) under the assumption of no differential lensing between the emission coming from dust and gas, the apparent $L'_{\rm CO(1-0)}$ of the high-z DSFGs are ∼1 dex higher than local ULIRGs. This can be at least partially explained by the lensed nature of the majority of the high-z galaxies. It is however worth noting that 79% of our sample shows $\mu L'_{\rm CO(1-0)}$ values in agreement with those explored by M. Frias Castillo et al. (2023) for unlensed DSFGs at $z = 2$–5. Assuming an average magnification factor of $\mu = 7$ (see, e.g., R. S. Bussmann et al. 2015) for our sample, leading to $L'_{\rm CO(1-0)} \sim (0.7 - 7) \times 10^{10}$ K km s^{-1} pc^2, we still infer marginally larger cold gas reservoirs in our high-z DSFGs than those seen in local ULIRGs.

While the local star-forming disks have a median ratio ∼3× lower than high-z MS galaxies (see also N. Scoville et al. 2016), local starbursts ($z \sim 0$ ULIRGs) and high-z DSFGs are observed to exhibit similar ratios. However, local ULIRGs are known to be more compact than high-z DSFGs and possibly have higher IR surface brightness (e.g., P. M. Solomon et al. 1992; Y. Gao & P. M. Solomon 2004). The fact that, despite these differences, their observed $L_{\rm IR}/L'_{\rm CO\,(1-0)}$ ratios are consistent with distant DSFGs suggests that the star formation processes operating in these two populations are self-regulated. In other words, an internally regulated mechanism is likely responsible for maintaining the SFR per unit molecular gas mass within a small range across these two populations.

Both the highly star-forming populations (local ULIRGs and high-z DSFGs) have ∼4.3× higher $L_{\rm IR}/L'_{\rm CO(1-0)}$ ratios than local MS galaxies. However, these ratios are only about 1.5× higher than those of MS galaxies from the early Universe. Our results confirm this trend, also observed by R. Genzel et al. (2010), with improved statistics. R. Genzel et al. (2010) interpreted such higher ratios as evidence for more rapid or efficient star formation (see their Figure 2).

It is also important to note that this offset may arise from warmer dust temperatures ($T_{\rm d}$) in the highly star-forming galaxies, both at low and high redshifts (see, e.g., G. E. Magdis et al. 2012; M. Béthermin et al. 2013). For instance, assuming a constant gas and dust mass across local disks and ULIRGs, we can model the galaxy's emission as a blackbody, where $L_{\rm IR} \propto {T_{\rm d}}^4$, when optically thick at all wavelengths (G. E. Magdis et al. 2012; S. Jin et al. 2022). Alternatively, if we treat the emission as that of a graybody in the thin limit, this relationship approximately becomes $L_{\rm IR} \propto {T_{\rm d}}^{4.5}$. Under this assumption, the observed offset in the $L_{\rm IR}/L'_{\rm CO(1-0)}$ ratios between these two populations could be explained by increasing the dust temperature in starbursts (3–8)× compared to local disks—as the $L_{\rm IR}$ of starbursts are on average ∼1.5–4 dex higher. This temperature difference may also be connected to a more efficient star formation process.[28]

4.2. Redshift Evolution of $L_{\rm IR}/L'_{\rm CO\,(1-0)}$ Ratio, a Proxy for Star Formation Efficiency

The integrated $L_{\rm IR}/L'_{\rm CO\,(1-0)}$ ratio is a proxy for the star formation efficiency (SFE) of galaxies. Given an available molecular gas reservoir, SFE measures the efficiency at which stars form out of this material. This is formulated as SFE = (SFR/$M_{\rm gas}$), where the SFR is related to the rest-frame 8–1000 μm total infrared luminosity ($L_{\rm IR}$) using a relation from R. C. Kennicutt (1989) as shown below, corrected for a G. Chabrier (2003) initial mass function.

$$\mathrm{SFR}[M_\odot\ \mathrm{yr}^{-1}] = 1.09 \times 10^{-10} L_{\rm IR}[L_\odot] \tag{4}$$

We caution the reader that the integrated measurements presented here average over the smaller-scale variations in physical conditions within each galaxy, providing a global SFR.

With our comprehensive CO(1–0) observations, we examine the redshift evolution of the $L_{\rm IR}/L'_{\rm CO\,(1-0)}$ ratio, a direct observational proxy for SFE (see upper panel of Figure 3). This approach avoids assumptions about $\alpha_{\rm CO}$, which affect SFE estimates through uncertainties in $M_{\rm gas}$. The $L_{\rm IR}/L'_{\rm CO\,(1-0)}$ ratio shows no significant trend with redshift when comparing high-z DSFGs to local ($z \sim 0$) ULIRGs, though the scatter increases at $z > 2$, and the number statistics become limited at $z > 4$. Notably, the Vz-GAL sample and other Herschel-selected sources exhibit relatively less scatter than the rest of the distant DSFGs collected from the literature. Our 500 μm-selected DSFGs appear to be marginally shifted toward the higher end of this ratio compared to other distant, dusty galaxies. This could reflect source selection effects, plausibly leading to different dust temperatures for a fixed gas mass.[29]

As discussed in Section 4.1, the Vz-GAL sources show consistency with the local ULIRG samples over a wide redshift range, owing to their high SFRs per available gas mass and/or elevated dust temperatures. This result confirms the similarity in their star-forming environments. Furthermore, a clear distinction between MS galaxies and starbursts is evident in the local Universe, but this separation is poorly constrained beyond $z \sim 2$, where MS galaxy data are sparse. Therefore, it remains uncertain whether DSFGs and MS galaxies at early cosmic epochs have (1) similar SFEs or gas depletion times, and/or (2) comparable dust heating mechanisms.

4.3. Redshift Evolution of Gas Depletion Timescales

The inverse of the star formation efficiency (SFE) is defined as the molecular gas depletion time, $\tau_{\rm dep} = (M_{\rm gas}/\mathrm{SFR})$, which is a measure of the duration it would take for the gas reservoir to be depleted by the ongoing SFR. This definition assumes an absence of external processes (e.g., gas accretion, outflows, or AGN feedback) affecting the present gas reservoir and a constant SFR throughout the star-forming period. This timescale ($\tau_{\rm dep}$) is useful to investigate galaxy evolution in the

---

[28] In addition to thermal and photoelectric heating, possibilities of other dust heating mechanisms cannot be neglected, e.g., cosmic-ray heating, shock heating, and gas-dust collisional heating.

[29] To avoid the $T_{\rm d} - z$ degeneracy (see C. M. Casey et al. 2014), we consider the galaxies around cosmic noon (z = 2–3). This includes all of the DSFGs with different selection criteria, and MS galaxies in the given redshift range. We plot their $L_{\rm IR}$ versus $L_{\rm IR}/L'_{\rm CO}(1-0)$ ratios in Appendix B, which do not show significant variation across various samples, despite the differences in (i) the selection criteria, (ii) observed IR luminosities (hence, $T_{\rm d}$), and/or (iii) lensing factors. The median ratios for these galaxy populations are comparable within a factor of 2, except for a few outliers (see Appendix B).

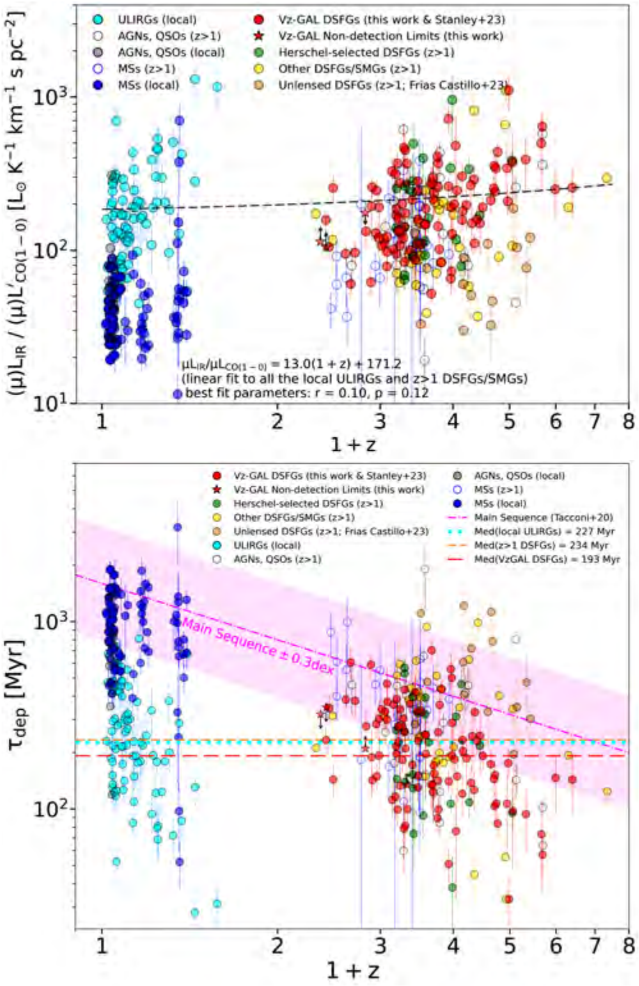

Figure 3. Upper panel: redshift evolution of the total infrared (8–1000 μm) to CO(1–0) luminosity ratio $L_{\rm IR}/L'_{\rm CO}(1-0)$ as a proxy for SFE. The linear fit shown with a dashed black line considers all of the high-z DSFGs and local ULIRGs, which shows no confirmation of a linear trend. We choose to plot the redshift in log-scale here to highlight the variation across MS galaxies and ULIRGs at $z\sim 0$. Lower panel: variation of the gas depletion time ($\tau_{\rm dep}$) as a function of redshift when assuming $M_{\rm H_2}=4L'_{\rm CO}(1-0)$ (see Section 3.2.1) and SFR $=1.09\times 10^{-10}L_{\rm IR}$ (see Section 4.2). The dashed red line is the median $\tau_{\rm dep}$ for the Vz-GAL sources, which is compared to that of local ULIRGs (cyan dotted line) and all DSFGs including the Vz-GAL sample (dashed orange line). The SFR−M_* main sequence (MS) shown as magenta dashed line is based on Figure 7 from L. J. Tacconi et al. (2020), which varies as $\tau_{\rm dep}=1.6\times(1+z)^{-1}$. Both panels include the literature data points mentioned in the caption of Figure 2. Please note that a gap in CO(1–0) observations (rest-frame 115 GHz) around $z=1$ is due to the current observational limitation at corresponding redshifted frequencies.

early Universe. In Appendix A, we list the depletion times of our targeted DSFGs.

Figure 3 (lower panel) shows the redshift evolution of the gas depletion time ($\tau_{\rm dep}$). The observed $\tau_{\rm dep}$ values (∼50–600 Myr) align with those reported for other DSFGs in the literature for the adopted $\alpha_{\rm CO}$ (e.g., C. L. Carilli et al. 2010; C. E. Sharon et al. 2016; S. Berta et al. 2023; F. Stanley et al. 2023), and are consistent with typical values found in local ULIRGs undergoing intense starbursts, as also reflected in the scaling relations in Figure 2. The median $\tau_{\rm dep}$ for high-z DSFGs is comparable to that of local ULIRGs, suggesting that these high-z galaxies are equally efficient at star formation. In other words, the $\tau_{\rm dep}$ in high-z dusty systems are not disproportionately higher than local ULIRGs, although they seem to have more molecular gas available. As discussed in Section 4.1, this infers a plausible balance of internal processes within these galaxy populations that regulates the SFR per available unit molecular gas mass. Notably, at higher redshifts ($z>3.5$), the Vz-GAL DSFGs exhibit somewhat shorter depletion timescales—indicative of elevated SFEs—compared to both local MS galaxies and ULIRGs. However, this apparent trend remains tentative due to the limited sample size at these redshifts.

About 42% of our sample lies within 0.3 dex of the empirical main sequence (MS) defined by L. J. Tacconi et al. (2020) at corresponding redshifts. The majority fall below the MS, consistent with their observed higher SFRs (upper panel of Figure 2) and enhanced SFEs (upper panel of Figure 3) compared to local MS galaxies. On the other hand, high-z MS galaxies from the literature follow the empirical trend from L. J. Tacconi et al. (2020) when compared with their local counterparts. We note that many of the local MS galaxies have known observational $\alpha_{\rm CO}$ values that are higher (e.g., A. Saintonge et al. 2017) than the assumed conversion factor of 4 $M_\odot$ (K km s^{-1} pc^2)$^{-1}$ in Figure 3 (lower panel), making them evenly spread on the MS if corrected.

Overall, Figure 3 confirms that high-z DSFGs plausibly represent a heterogeneous population encompassing a broad range of dusty, star-forming systems. This population likely includes both galaxies experiencing extreme starburst activity, analogous to local ULIRGs, as well as systems that lie within the scatter of the empirical star-forming MS. It may also be possible that DSFGs at high redshifts are more-massive versions of local, giant MS galaxies that are undergoing starburst episodes, making their integrated SFEs comparable to local ULIRGs. The high-z MS galaxies are already expected to exhibit relatively shorter gas depletion times compared to local MS galaxies (L. J. Tacconi et al. 2020). However, measurements of stellar masses to derive the distance from the star-forming MS (ΔMS) and better estimates of the $\alpha_{\rm CO}$ conversion factor for our sample will be necessary to extract detailed inferences (see also discussion in S. Berta et al. 2023). In addition, better statistics at $z>4$ will be beneficial to confirm the consistent, plausible decreasing trend in $\tau_{\rm dep}$ with redshift, which would indicate that infrared-luminous, dusty galaxies at earlier epochs had increasingly higher SFEs than seen in local massive MS galaxies and ULIRGs.

4.4. CO Line Ratios

The relative line luminosities of various rotational transitions of the CO molecule, tracing the molecular gas (H$_2$), depend on the gas excitation conditions. As can be seen in Equation (2) and the existing literature, the CO(1–0) transition is robustly calibrated as an anchor point to derive the total molecular gas masses, and is also important to measure precise CO line ratios. Also known as CO brightness temperature ratios, these are defined as follows:

$$r_{J1}=\frac{L'_{{\rm CO}(J\to J-1)}}{L'_{{\rm CO}(1-0)}}, \quad (5)$$

where, J is an index of the upper level in CO($J\to J$–1) transition, whose line luminosity is $L'_{{\rm CO}(J\to J-1)}$.

For optically thick and thermalized gas, all of the CO rotational levels are equally excited and the brightness temperature ($T_{\rm b}$) of all of these levels is the same. This leads to

Table 1
CO Line Brightness Temperature Ratios

$J_{\rm up}$	V*z*-GAL (SNR>5)		V*z*-GAL (full)		CW 13	H21 LPs
	Median	Mean	Median	Mean	DSFGs	Mean
1	1	1	1	1	1	1
2	0.88 ± 0.25	1.00 ± 0.25	0.88	0.99	0.85	0.88 ± 0.07
3	0.61 ± 0.22	0.65 ± 0.22	0.61	0.66	0.66	0.69 ± 0.12
4	0.49 ± 0.15	0.54 ± 0.15	0.49	0.55	0.46	0.52 ± 0.14
5	0.47 ± 0.13	0.54 ± 0.13	0.45	0.51	0.39	0.37 ± 0.15
6	0.28 ± 0.13	0.36 ± 0.13	0.28	0.37	0.30	0.25 ± 0.14
7	…	…	0.59[a]	0.50[a]	0.27	0.17 ± 0.12

Note. Ratios for the V*z*-GAL sample in the first two columns are only with the DSFGs detected above 5σ significance in both CO lines. Their statistical error bars are the (unscaled) median absolute deviation (MAD) of the respective distributions. The subsequent two columns with line ratios of the full V*z*-GAL sample are also consistent. CW 13 DSFGs are from C. L. Carilli & F. Walter (2013). H21 LPs are the Planck-identified lensed galaxies from K. C. Harrington et al. (2021).

[a] r_{71} is based on only three source statistics, and all of these have CO(1–0) detection with $2 < \mathrm{SNR} < 5$ (see the text for details).

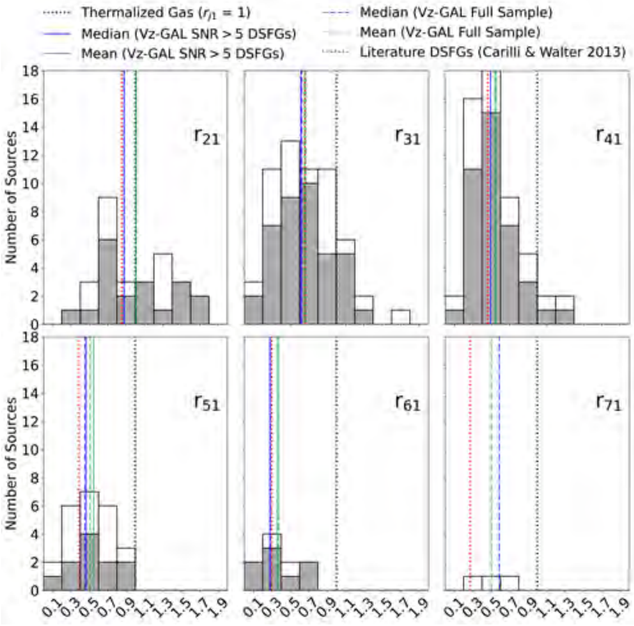

Figure 4. CO line ratio histograms for the V*z*-GAL sample. The shaded histograms in gray are with the sources detected above 5σ significance, and the white histograms show the rest of our targets that have SNR > 2. The ratios show mostly subthermal excitation of the mid-/high-*J* CO lines, indicating the importance of CO(1–0) as an anchor point and as a robustly calibrated molecular gas mass tracer. The values compiled by C. L. Carilli & F. Walter (2013) are plotted for comparison (red dotted lines). Optically thick and thermalized gas with $r_{J1} = 1$ is shown as black dashed lines in each subplot.

$r_{J1} = 1$ for all of the values of J (hence, $I_{\rm CO} \propto J^2$; see Figure 5). In practice, these ratios exhibit significant variation—particularly as a function of the gas excitation temperature ($T_{\rm ex}$) and the molecular hydrogen number density ($n_{\rm H_2}$; e.g., A. Weiß et al. 2005b; D. A. Riechers et al. 2011b, 2011d; K. C. Harrington et al. 2021). For example, the brightness temperature ratios of high-*J* CO levels (say, $J \gtrsim 6$) are typically elevated when the system has intense radiation field and/or shock-excited hot/dense gas due to stellar feedback processes, such as supernovae or outflows. In contrast, the population/occupancy of CO molecules in lower-*J* levels dominate in Milky Way–like normal star-forming disks (D. J. Fixsen et al. 1999; N. Sulzenauer et al. 2021; K. C. Harrington et al. 2025). In this way, the observed CO line ratios inform us about the physical properties, namely temperature and density, of the star-forming gas.

In Figure 4, we show the statistical distribution of CO line ratios of the V*z*-GAL sample up to $J = 7$. We observe mostly subthermal excitation ($r_{J1} < 1$) for our targets. The median line ratios for the targets detected above 5σ confidence in both the CO rotational levels involved with the respective line ratio are presented in Table 1. Our values with improved statistics and high-SNR measurements confirm those derived by C. L. Carilli & F. Walter (2013) and K. C. Harrington et al. (2021). The computed r_{31} here is also in agreement with the values derived by C. E. Sharon et al. (2016) and C. Yang et al. (2017). Our median r_{71} is $\sim$2.5× higher than the value presented by C. L. Carilli & F. Walter (2013), albeit this is using only three V*z*-GAL DSFGs (HeLMS-19, HerS-11, and HerBS-185) with available CO(7−6) spectra. These galaxies, with CO(1–0) detection below 5σ significance, have r_{71} of 0.59 ± 0.17, 0.65 ± 0.36, and 0.26 ± 0.11, respectively. Therefore, the derived median will need better statistics and deeper observations to be confirmed (see the lower-right panel of Figure 4). Further, we find no apparent trend between any of the CO line ratios and redshift within the V*z*-GAL sample ($1 < z < 6$) as also observed by C. E. Sharon et al. (2016) for r_{31} in a sample of 14 galaxies at $z = 2$–3.

These brightness temperature ratios reiterate the importance of CO(1–0) observations, given that the subthermal line ratios can lead to additional uncertainties in the total molecular gas masses derived based on higher-*J* CO levels. For example, gas masses estimated from the CO(3−2) observations may lead to an underestimation by (40 ± 22)%, under unknown excitation, compared to the values derived based on the CO(1–0) line. CO(2−1), seems to serve as a better $L'_{\rm CO(1-0)}$ tracer than CO(3−2), as it shows line ratios (r_{21}) close to unity, which has also been noticed in integrated measurements of massive local galaxies (e.g., xCOLD-GASS sources from A. Saintonge et al. 2017). We discuss this further in Section 4.4.1.

In Appendix B, we list the sources with unusually low ratios ($r_{J1} < 0.2$). Further, we observed superthermal line ratios ($r_{J1} > 1$ for $2 < J < 4$) for a few V*z*-GAL DSFGs (see statistics in Figure 4); however, these ratios are consistent with being $r_{J1} \leqslant 1$ (subthermal) when considering the associated uncertainties in the flux calibration of line measurements (see Appendix B). Superthermal ratios are expected to arise if the gas has a highly excited partition function. This implies that, in such environments, the relative columns in the $J = 0$ and $J = 1$

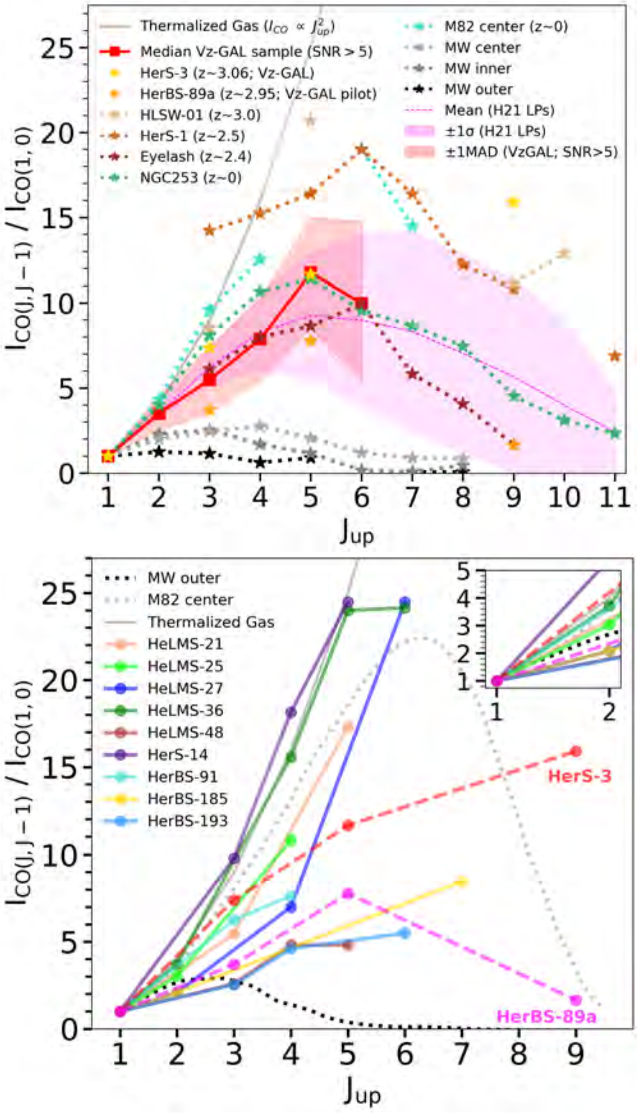

Figure 5. Upper panel: median CO SLED of the V*z*-GAL sample (solid red curve) compared to sources from the literature including: five high-*z* DSFGs, HerS-3 at $z = 3.061$ (this work and P. Cox et al. 2025), HerBS-89a at $z = 2.95$ (S. Berta et al. 2021), HLSW-01 at $z = 2.96$ (D. A. Riechers et al. 2011c; K. S. Scott et al. 2011), HerS-1 at $z = 2.55$ (K. C. Harrington et al. 2019; B. Liu et al. 2022), and the Cosmic Eyelash at $z = 2.32$ (A. L. R. Danielson et al. 2011; A. M. Swinbank et al. 2011); local starbursts NGC 253 (F. P. Israel et al. 1995; M. J. F. Rosenberg et al. 2014; J. P. Pérez-Beaupuits et al. 2018) and M82 center (A. Weiß et al. 2005b); and the Milky Way, where we adopted the line fluxes of three different regions from D. J. Fixsen et al. (1999), namely the central star-forming zone (MW center), the inner disk (MW inner), and the outer disk (MW outer). The magenta-shaded region is based on the model-derived median line ratios of Planck-identified lensed galaxies (H21 LPs; K. C. Harrington et al. 2021), which is in good agreement with our V*z*-GAL median values (region shaded in red). Lower panel: CO SLEDs of 11 individual high-*z* DSFGs from our V*z*-GAL sample in comparison with the Milky Way and local starburst M82. This plot highlights the variety of excitation conditions across the V*z*-GAL large sample. SLED modeling for two of these galaxies, namely HerS-3 and HerBS-89a, has already been presented by P. Cox et al. (2025) and S. Berta et al. (2021), respectively. The gray solid curve in both panels shows optically thick and thermalized gas condition of the CO SLED. All of the line fluxes ($I_{\rm CO}$) used here are in the units of Jy km s^{-1}.

levels are lower than those under Milky Way–like conditions because a significant fraction of the gas is in higher excited states. Under high excitation conditions, since the opacity in the CO(1–0) line is expected to be lower than that of the higher-*J* transitions (at least securely up to $J \sim 4$), the CO(1–0) line is apparently the first to get optically thin, making the line ratios superthermal. The confirmation of such ratios will need detailed investigation using semiempirical models and/or better observations of low-SNR targets.[30]

In the upper panel of Figure 5, we compare the median CO line ratios of the V*z*-GAL sample to SLEDs of five high-*z* DSFGs (HerS-3, HerBS-89a, HLSW-01, HerS-1, and the Cosmic Eyelash), two local starburst galaxies (NGC 253 and M82), and the Milky Way—all with available CO(1–0) observations. These results summarize that the median CO SLED of the V*z*-GAL sample ($1 < z < 6$), peaking at $J \sim 5$, follows a similar behavior as depicted by the local starburst NGC 253 and the Cosmic Eyelash, one of the extreme DSFGs. K. C. Harrington et al. (2021) also observe model-based SLEDs peaking between $J = 4$ and $J = 6$ for most of their Planck-identified high-*z* lensed DSFGs. Such a peak at $J > 4$ confirms a presence of warm/dense gas component in our targeted DSFGs along with the cold gas traced by CO(1–0) and other low-*J* levels. This warm/dense gas seem to dominate the CO SLEDs of these DSFGs. Such dense star-forming environments are also found close to the Galactic central molecular zone (see, e.g., M. Kohno & Y. Sofue 2024). Note that each median CO line ratio contributing to the V*z*-GAL CO SLED in the upper panel of Figure 5 is based on different sample sizes, depending on the availability of higher-*J* CO observations across the NOEMA bands. As a result, the median CO SLED does not necessarily reflect the excitation properties of any individual V*z*-GAL source and might be affected by redshift-dependent selection biases.

Overall, we notice a wide range of excitation conditions within high-*z* DSFGs, some also resembling the dense cores/center of local starbursts like M82. To better represent this variety, we depict the observed, well-sampled CO SLEDs of 11 V*z*-GAL DSFGs in the lower panel of Figure 5. It is clear from this presentation that the V*z*-GAL sample includes high-*z* dusty galaxies with a noticeable spread in excitation conditions.

4.4.1. *A Comparison to z–GAL Results: Empirical Relations between CO(1−0), CO(2−1), and CO(3−2) Line Luminosity*

V*z*-GAL is a systematic CO(1–0) large survey of dusty galaxies in the early Universe, spanning the redshift range $1 < z < 6$. For this sample, S. Berta et al. (2023) investigated trends in the scaling relations based on the detected lowest-*J* level of the higher-*J* CO lines using NOEMA. In the absence of CO(1–0) observations, they consistently used either CO(2–1) or CO(3–2) to estimate gas masses and depletion timescales for most of these high-*z* DSFGs. The line ratios they adopted from C. L. Carilli & F. Walter (2013) are consistent with our findings (see Table 1). Similarly, M. Hagimoto et al. (2023) examined a sample of 71 Herschel-selected DSFGs (Herschel-BEARS) at $1.5 < z < 4.5$ in the southern sky, utilizing mid/high-*J* CO lines and K. C. Harrington et al. (2021) line ratios. The statistical trends in the scaling relation shown in the upper panel of Figure 2 confirm the results from these studies, given that the ratios they assumed are in agreement with our robustly

---

[30] One of the plausible reasons that could contribute to the scatter observed in histograms presented in Figure 4 might be gravitational lensing. Although differential magnification may not have a significant impact, the placement of caustics relative to the gas distribution might affect what we see while observing the regions of highest surface infrared brightness, given that these DSFGs are among the brightest high-*z* sources in the Herschel catalogs.

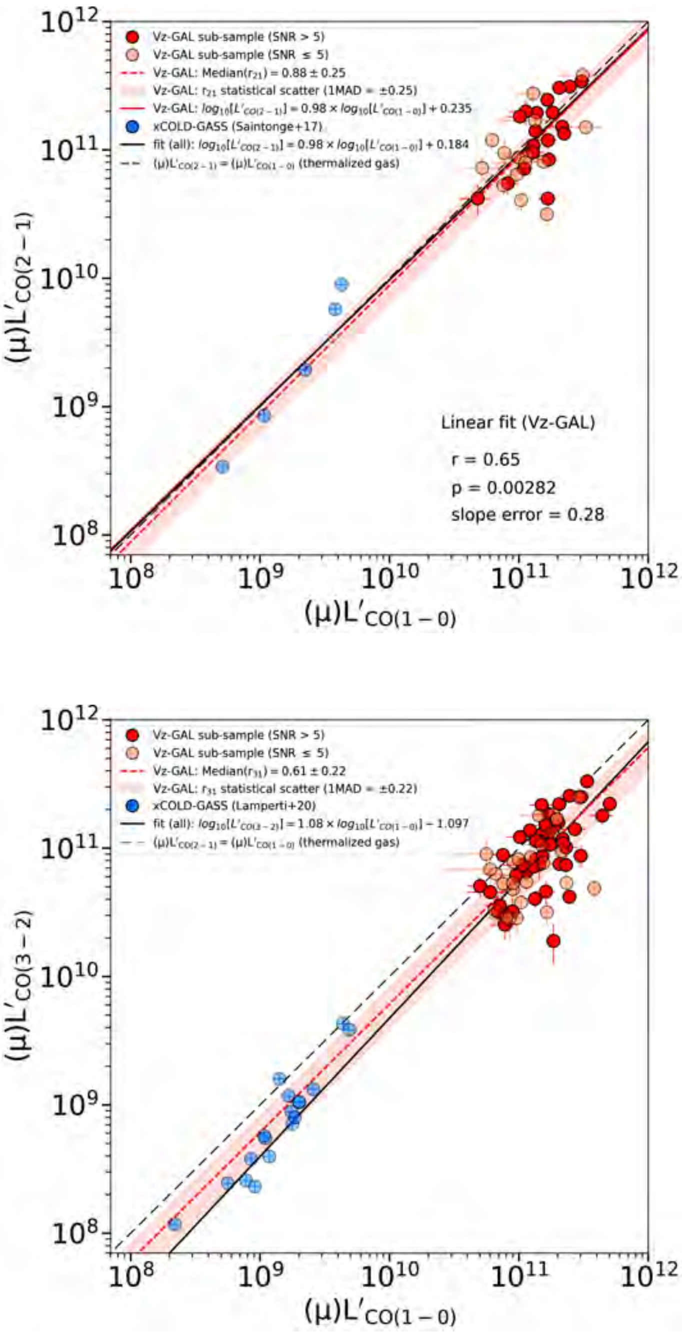

Figure 6. Upper panel: comparison of the CO(1–0) and CO(2–1) line fluxes for the V*z*-GAL DSFGs where both lines have been measured—with CO(2–1) from this work for the $z > 3$ sources and the rest from P. Cox et al. (2023). The data points with SNR > 5 are highlighted in dark red, for which the linear fit and median/mean values are presented. The results for the high-*z* DSFGs are compared to massive ($M_* > 10^{10} M_\odot$) local MS galaxies selected from the xCOLD-GASS survey (A. Saintonge et al. 2017; see the text for details). Lower panel: the same as the upper panel, but with a comparison of CO(3−2) with CO(1−0). Here, CO(3−2) data of the xCOLD-GASS sample is from I. Lamperti et al. (2020). In both upper and lower panels, the left panel shows an empirical correlation between the higher-*J* CO line and CO(1–0) luminosities. The slope of the best linear fits agrees with the sample median within the error bars. Local galaxies are overplotted as blue data points. The right panel shows the redshift distribution of the higher-*J* CO line to CO(1–0) ratio (i.e., r_{21}). Median and mean values are shown with red and green dashed lines, respectively. xCOLD-GASS median is shown using a blue dashed line, in agreement with the V*z*-GAL median within error bars. The shaded region in blue represents the spread in r_{21} or r_{31} for local galaxies (A. Saintonge et al. 2017; I. Lamperti et al. 2020; A. K. Leroy et al. 2022). In all of the plots, the black dashed line shows the optically thick and thermalized gas condition ($r_{J1} = 1$).

measured CO line ratios. To further analyze these low/mid-*J* CO levels, here we derive correlations with $L'_{\rm CO\,(1-0)}$.

As shown in Figure 4, the median ratio of CO(2–1) to CO(1–0) line luminosity is observed to be close to unity ($r_{21} = 0.88 \pm 0.25$). This indicates that the molecular gas masses, which are derived based on CO(2–1) observations, will be closer to the ones derived using Equation (2) and are less uncertain than those derived using higher-*J* CO lines that are mostly observed to have subthermal line ratios. To investigate a plausible relation between the line intensities of these two low-*J* CO levels, we plot $L'_{\rm CO(2-1)}$ versus $L'_{\rm CO(1-0)}$ for 34 V*z*-GAL sources for which both CO(1–0) and CO(2–1) observations are available from this study (V*z*-GAL) and the *z*–GAL survey (upper-left panel of Figure 6). We derive a

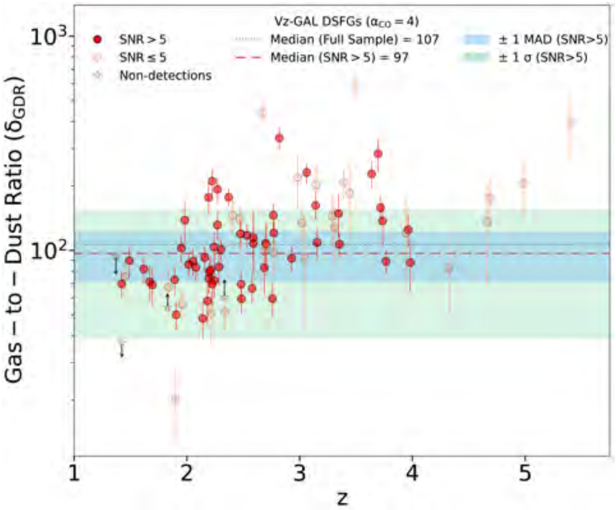

Figure 7. Gas-to-dust mass ratio ($\delta_{\rm GDR}$) of the V*z*-GAL sample using $\alpha_{\rm CO} = 4M_\odot({\rm K\ km\ s^{-1}\ pc^2})^{-1}$ and Milky Way–like κ_ν. The median $\delta_{\rm GDR}$ of the full sample is shown with a dotted black line, and the median for the targets is shown with a signal-to-noise ratio (SNR) > 5 with a dashed red line. The shaded green and blue regions highlight the 1σ and (unscaled) 1 MAD (median absolute deviation) ranges for the sources with SNR > 5, respectively.

strong linear correlation in log-space with a slope of 0.98 ± 0.28 and a y-intercept of 0.24. The statistical median- or mean-r_{21} of our DSFGs (within the error bars) agrees with the criteria posed by optically thick and thermalized gas conditions, suggesting $r_{21} \sim 1$.

Similar comparisons for large galaxy samples with available observations of both CO(1–0) and CO(2–1) exist for local (U)LIRGs (I. Montoya Arroyave et al. 2023) and nearby star-forming galaxies (J. S. den Brok et al. 2021; A. K. Leroy et al. 2022; R. P. Keenan et al. 2025), but are scarce at higher redshifts. However, CO(2–1) has been used to derive gas mass properties of high-z galaxies in the absence of CO(1–0) data (see, e.g., R. Genzel et al. 2010; M. S. Bothwell et al. 2013; J. D. Silverman et al. 2018; F. Valentino et al. 2018; L. J. Tacconi et al. 2020, and references therein). Our homogeneous target selection now confirms the usability of CO(2–1) as an alternative calibrator for gas mass derivation (Equation (2)) for the to-date largest DSFG sample.

In the upper-right panel of Figure 6, we explore the redshift evolution of r_{21}, which shows no trend. Our derived median for the V*z*-GAL DSFGs is consistent with the value found for the massive, local MS galaxies with $M_* > 10^{10} M_\odot$ (xCOLD-GASS; A. Saintonge et al. 2017). Similar r_{21} values have also been observed in the local Universe, particularly around galactic nuclei (i.e., inner kiloparsec region; J. Braine & F. Combes 1992; A. Weiß et al. 2005b). A. K. Leroy et al. (2022) compiled the low-J CO observations of local galaxies with different stellar masses to find a median r_{21} of 0.64 with the inclusion of the xCOLD-GASS sample from A. Saintonge et al. (2017). They derived the 16th and 84th percentile values of this r_{21} to be 0.52 and 0.91, respectively. A. K. Leroy et al. (2022) attributed these results to biases due to sample selection. In particular, they expected higher r_{21} values in the high-SFR galaxies, as could be the case for massive galaxies from A. Saintonge et al. (2017). This has been recently confirmed by R. P. Keenan et al. (2025) using detailed CO(2–1) measurements of the xCOLD-GASS galaxies and a more extended AMISS galaxy sample. It is also consistent with the results for local (U)LIRGs (see, e.g., I. Montoya Arroyave et al. 2023) and our intensely star-forming high-z DSFGs, having r_{21} close to unity.

In Figure 6 (lower panel), we present the $L'_{\rm CO(3-2)} - L'_{\rm CO(1-0)}$ correlation for 73 V*z*-GAL DSFGs with the CO(3−2) luminosities from *z*–GAL. This plot primarily shows subthermal r_{31} values for our targets, which aligns with the trends observed in massive, high-SFR, local main-sequence galaxies from the xCOLD-GASS sample (I. Lamperti et al. 2020). Our results for r_{31} are also consistent with those explored for a sample of about 40 ULIRGs in the local Universe (I. Montoya Arroyave et al. 2023). Further, we find no apparent redshift evolution here.

4.5. Gas-to-dust Mass Ratios

Gas-to-dust mass ratios ($\delta_{\rm GDR} = M_{\rm H_2}/M_{\rm dust}$) provide crucial insights on the evolutionary state and star formation activity of galaxies. Figure 7 presents the $\delta_{\rm GDR}$ of our high-z dusty galaxies. Dust masses ($M_{\rm dust}$) are from D. Ismail et al. (2023), which were calculated using B. T. Draine et al. (2014) templates with Milky Way–like absorption cross section per unit dust mass (κ_ν). Assuming solar metallicity environments in our high-z dusty galaxies, we adopt these dust masses, and also use a Milky Way–like CO–H_2 conversion factor to derive gas masses ($M_{\rm H_2}$) and subsequently $\delta_{\rm GDR}$. For the V*z*-GAL DSFGs detected above 5σ significance, we find a median $\delta_{\rm GDR} \sim 100$ using $\alpha_{\rm CO} = 4$ and Milky Way–like κ_ν. Within the ± 1 MAD around the median $\delta_{\rm GDR}$, our ratios agree with the values explored in the literature for local/high-z dusty starbursts (e.g., K. C. Harrington et al. 2019; R. Herrero-Illana et al. 2019; G. Popping et al. 2023) and the values derived in the *z*–GAL study (S. Berta et al. 2023), after adapting to their choice of $\alpha_{\rm CO}$.

More importantly, our median gas-to-dust mass ratio of about 100 for the chosen values of $\alpha_{\rm CO} = 4$ and $\kappa_{850} = 0.047\ {\rm m^2\ kg^{-1}}$ (B. T. Draine et al. 2014; D. Ismail et al. 2023) leads to a ratio $\kappa_{\rm H} = \delta_{\rm GDR}/\kappa_{850}$ of 2130 ${\rm kg\ m^{-2}}$, which is consistent with the mid-range of extragalactic determinations, $\kappa_{\rm H} = 1500-2200\ {\rm kg\ m^{-2}}$, used by L. Dunne et al. (2022) for metal-rich, dusty galaxies across redshifts. This is, in turn, also in agreement with measurements of the diffuse ISM in the Milky Way.

A broad distribution ($\delta_{\rm GDR} \sim$ 50–300) within this sample highlights inherent differences in the metallicities and star-forming environment of individual DSFGs as also observed in their gas depletion times (see Figure 3). Local LIRGs and non-LIRG spiral galaxies also show a similarly broad distribution in gas-to-dust mass ratios in the literature (e.g., A. K. Leroy et al. 2011; R. Herrero-Illana et al. 2019).

While we see a range in $\delta_{\rm GDR}$ (hence, also in metallicities but not exclusively; see G. Popping et al. 2023) for the V*z*-GAL DSFGs, many of them are expected to have supersolar metallicity given their dusty nature (L. Dunne et al. 2022; S. Berta et al. 2023). We note that the ratios for the V*z*-GAL sample are mostly consistent with the Milky Way and other local disks with similar metallicity (and $\alpha_{\rm CO} \sim 4$), though they tend to lie at the lower end of the typical $\delta_{\rm GDR}$ range known for these MS galaxies (e.g., P. Andreani et al. 1995; V. Zubko et al. 2004; A. Rémy-Ruyer et al. 2014). In other words, about 50% of our sample (with SNR > 5) showing $\delta_{\rm GDR} < 100$ (Figure 7) indicates a possibility of them having supersolar metallicity plausibly due to larger dust masses. However, there are caveats in derivations of dust masses that need to be addressed.

Although CO(1–0) observations help reduce the uncertainty related to the excitation ladder of the CO molecule by providing direct measurements of $L'_{\rm CO\,(1-0)}$, interpreting the gas-to-dust mass ratio remains challenging due to two more sources of uncertainty: (1) the gas mass dependence on the choice of $\alpha_{\rm CO}$, and (2) the dust mass estimation from the spectral energy distribution fitting that depends on the dust temperature ($T_{\rm d}$) and an assumption on κ_ν. For our 500 μm-selected V*z*-GAL sample, D. Ismail et al. (2023) derived the dust masses—that are used in Figure 7—using the optically thin approximation of the MBB to fit the cold dust component. This may lead to lower dust temperatures and higher $M_{\rm dust}$, as both are degenerate. As explained by D. Ismail et al. (2023), this could be improved with spatially resolved observations from which one can estimate the sizes of the DSFGs, which will be useful in combination with more precise GMBB (general MBB, optically thick) models. In general, we expect the GMBB models to provide higher dust temperatures and lower $M_{\rm dust}$. A reasonable $\delta_{\rm GDR}$ range could still be obtained with our chosen $\alpha_{\rm CO}$ and κ_ν, if the dust masses were lower. However, as such, we do not regard this finding as a strong evidence for a Milky Way–like $\alpha_{\rm CO}$.

4.6. Comparison to [CI](1−0)

The atomic carbon fine-structure emission line, [CI](1−0) ($\nu_{\rm rest} = 492.16$ GHz), has been explored as a promising tracer of extended cold gas in distant DSFGs due to its observed linear correlation with CO(1–0) (e.g., F. P. Israel et al. 1995; P. P. Papadopoulos & T. R. Greve 2004; A. Weiß et al. 2005a; L. Dunne et al. 2021, 2022; G. Gururajan et al. 2023; M. Frias Castillo et al. 2024). As a three-level system, [CI] allows us to determine $T_{\rm ex}$ of the gas by observing the [CI](1−0) and [CI](2−1) ($\nu_{\rm rest} = 809.34$ GHz) transitions. Importantly, the availability of both [CI] and CO(1–0) observations helps in narrowing down the range in the possible values of the physical properties (density and temperature) related to the gas excitation in DSFGs with well-sampled CO SLEDs.

To date, most of the high-*z* DSFGs detected in [CI] lines from the literature do not have CO(1–0) observations, leading to an uncertainty in their [CI]/CO ratios due to adopted CO line ratios ($r_{J,J-1}$; $J \geqslant 2$) (see Section 4.4). We conduct a [CI](1−0)/CO (1–0) ratio comparison in a robust and statistically meaningful sample of 23 V*z*-GAL DSFGs with [CI](1−0) from R. Neri et al. (2020) and P. Cox et al. (2023). As depicted in Figure 8, we find a median ratio (with unscaled MAD error bars) of log ($L'_{\rm [CI]\,(1-0)}/L'_{\rm CO\,(1-0)}$) = -0.71 ± 0.12, which is consistent with the values of -0.62 ± 0.14 (other high-*z* DSFGs) and -0.74 ± 0.12 (local ULIRGs) found by M. Frias Castillo et al. (2024) and I. Montoya Arroyave et al. (2023), respectively. The values presented by M. Frias Castillo et al. (2024) are based on twelve 850 μm-selected unlensed DSFGs at $2 < z < 5$. In addition, our ratios also agree with local MS galaxies that show a global $\log(L'_{\rm [CI]\,(1-0)}/L'_{\rm CO\,(1-0)}) \sim -0.85$ (e.g., C. D. Wilson 1997; D. Liu et al. 2023) and other heterogeneous samples of 16 high-*z* galaxies (see Figure 8 and its caption), confirming the linear relation between [CI] and CO ground states across redshifts for various galaxy populations, irrespective of the expected differences in their excitation conditions.

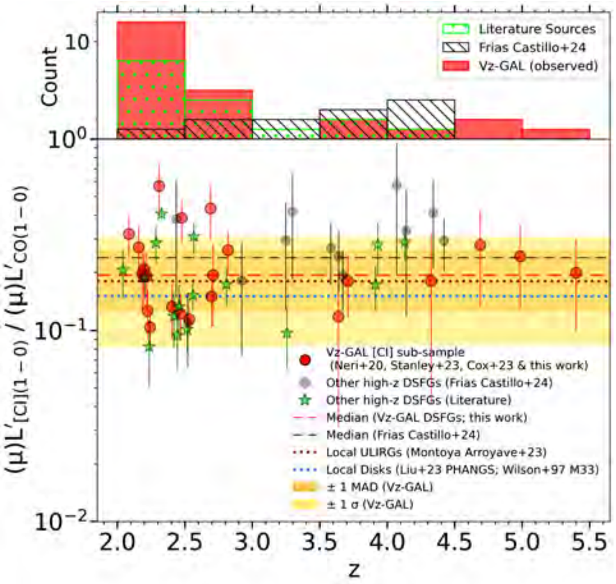

Figure 8. Comparison of the CO(1–0) line luminosity with the luminosity of an alternative cold gas tracer, [CI](1−0), for 23 V*z*-GAL targets. The other 12 high-*z* DSFGs from M. Frias Castillo et al. (2024) are shown as gray points with detections of both the lines. More heterogeneous literature points for 16 dusty galaxies at $z > 1$ are shown with green asterisk markers that have both [CI](1–0) (F. Walter et al. 2011; S. Alaghband-Zadeh et al. 2013; H. Dannerbauer et al. 2019; N. P. H. Nesvadba et al. 2019; L. Dunne et al. 2022) and CO(1–0) (D. A. Riechers et al. 2006, 2009, 2011a; J.-F. Lestrade et al. 2011; A. P. Thomson et al. 2012; S. Alaghband-Zadeh et al. 2013; H. Dannerbauer et al. 2019; K. C. Harrington et al. 2019; L. Dunne et al. 2022) observations. The red and black dashed lines show the median ratios for the V*z*-GAL and M. Frias Castillo et al. (2024) data points that are compared to the values derived for local ULIRGs (I. Montoya Arroyave et al. 2023) and star-forming MS galaxies (C. D. Wilson 1997; D. Liu et al. 2023) in brown and blue dotted lines, respectively. The histogram above the main plot summarizes the redshift distribution and statistical significance of our subsample compared to the literature.

Furthermore, we find no redshift evolution of [CI]/CO ratio based on the available statistics (Figure 8). Similar ratios across populations at a wide range of redshifts therefore point to a common baseline state of the ISM, upon which different star formation modes, efficiencies, and scales are built—highlighting that the [CI](1−0) is also a usable mass estimator.[31] The similarity in the [CI](1−0)/CO(1−0) line luminosity ratio between V*z*-GAL and local MS galaxies disfavors the usage of two different CO–H$_2$ conversion factors ($\alpha_{\rm CO}$) for these two galaxy populations (and in turn also for local ULIRGs); i.e., a bimodal behavior. This motivated our choice of $\alpha_{\rm CO} = 4$ throughout the statistical analyses of the V*z*-GAL large sample (see Section 3.2.1 and Appendix A).

The lack of redshift evolution is also interesting given that CO(1–0) ($T_{\rm ex} \sim 5$ K) has lower excitation temperature than [CI](1−0) ($T_{\rm ex} \sim 24$ K), making it plausibly more susceptible to excitation by the increasingly warm CMB toward high-*z* (e.g., E. da Cunha et al. 2013). In addition, we observe only a marginal increase in the [CI]/CO ratios of ULIRGs and high-*z* DSFGs compared to local star-forming MS galaxies (Figure 8), suggesting broadly similar ISM conditions, despite the fact that these systems exhibit significantly higher CO(1–0)

---

[31] Apparently, abundance variations of [CI] are expected to be minor across different source selections. It, therefore, still works in favor of [CI](1–0) in cases where [CI] can be optically thin—for which a line intensity is expected to vary linearly with abundance.

luminosities (Figure 2), elevated star formation efficiencies, and shorter depletion timescales (Figure 3). Detailed investigations of these aspects need the support from semiempirical radiative transfer models to understand the star formation and gas excitation conditions.

4.7. CO(1–0): The Best Gas Mass Tracer?

The molecular gas masses we derived in this work are best calibrated by the canonical tracer, CO(1–0), since $\alpha_{\rm CO}$ is calibrated on CO(1–0) line luminosity. However, in many local and high-z, actively star-forming galaxies, lower-J transitions like CO(1–0) and CO(2–1) are found to be thermalized and saturated; i.e., their brightness temperature ratio is $r_{21} \sim 1$ (A. Saintonge et al. 2017; K. C. Harrington et al. 2021; A. K. Leroy et al. 2022, R. P. Keenan et al. 2025, and this work), owing to their high optical depth. In such cases, the brightness temperature ($T_{\rm b}$) of these transitions closely approaches the kinetic temperature ($T_{\rm kin}$) of the gas, modulo corrections due to the CMB. Consequently, these low-J CO lines become insensitive to the molecular gas columns for such extreme environments. In other words, although gas masses are robustly calibrated using CO(1–0) line luminosity as per Equation (2), this ground-state CO transition may not be the best column density tracer.

The linear dependence between the [CI](1–0) and CO(1–0) line luminosities (Section 4.6) suggests that perhaps [CI](1–0) is also optically thick in such extreme environments and is expected to have similar limitation as CO(1–0). However, the luminosity of [CI](1–0) can be explored to complement CO observations in statistically large samples of actively star-forming galaxies. For each high-z DSFG, the "best calibration" of column density and total gas masses therefore will be obtained by modeling multiple lines (and continuum) observations together (e.g., K. C. Harrington et al. 2021).

5. Conclusions

We presented the first results from the Vz-GAL VLA Large Program. Out of the targeted 92 submillimeter/infrared bright ($L_{8-1000\mu\rm m} > 10^{12}$–$10^{13} L_{\odot}$), dusty star-forming galaxies (DSFGs), 90 are detected above a significance level above 2σ, including 57 with an SNR > 5. Only two DSFGs remain undetected with signal levels below 2σ. When combined with the 14 DSFGs from the pilot survey (F. Stanley et al. 2023), our full sample comprises 106 galaxies, making Vz-GAL the largest CO(1–0) survey of DSFGs in the early Universe to date.

We derive molecular gas masses based on CO(1–0), along with gas scaling relations, gas-to-dust mass ratios, and CO line ratios for this large, homogeneous sample—quintupling the existing CO(1–0) statistics of Herschel-selected galaxies in the early Universe. Effectively, our sample size doubles all of the available high-redshift CO(1–0) measurements combined from the literature, which have rather heterogeneous selection methods. Additionally, we report CO(2–1) line luminosities for 10 Vz-GAL DSFGs, and investigate [CI]/CO line ratios for 23 galaxies using [CI](1–0) measurements from the NOEMA z–GAL survey (R. Neri et al. 2020; P. Cox et al. 2023). We summarize the key findings as follows:

1. We obtain CO(1–0)-derived gas masses (using a Milky Way–like CO–H$_2$ conversion factor $\alpha_{\rm CO} = 4$) for the Vz-GAL galaxies of $M_{\rm H_2} = (2 - 20) \times 10^{11} M_{\odot}$, which are not corrected for gravitational lensing.
2. We find no evidence supporting a bimodal conversion factor ($\alpha_{\rm CO}$). Further, the data do not exclude the possibility that a single $\alpha_{\rm CO}$ applies to all galaxy populations.
3. Both local ULIRGs and high-z DSFGs are confirmed to exhibit more efficient star formation and/or have warmer dust temperatures than local MS galaxies. These two highly star-forming populations also show an internally self-regulated range in SFRs per unit gas mass.
4. Gas depletion timescales derived using $\alpha_{\rm CO} = 4$ for our sample are in the range 50–600 Myr, confirming that such high-z DSFGs are potentially a mixed population of starbursts and MS galaxies at those redshifts. Its confirmation, however, needs stellar masses to characterize the MS.
5. Robustly derived CO line ratios (Table 1) for the Vz-GAL sample confirm, with better statistics, the values explored by C. L. Carilli & F. Walter (2013), C. E. Sharon et al. (2016), C. Yang et al. (2017), and K. C. Harrington et al. (2021).
6. Although the median CO line ladder of Vz-GAL galaxies peaks around $J = 5$, a wide variety of gas excitation conditions are found across these high-z DSFGs.
7. The median gas-to-dust mass ratio ($\delta_{\rm GDR} = 100$) derived using Milky Way–like $\alpha_{\rm CO}$ and κ_{ν} is consistent with other extragalactic values explored for metal-rich, dusty galaxies (e.g., L. Dunne et al. 2022).
8. The consistency in the [CI](1–0)/CO(1–0) luminosity ratio values across redshifts in distant DSFGs, local ULIRGs, and star-forming MS galaxies suggests broadly similar conditions in their ISM, despite the differences in CO(1–0) line luminosities and gas depletion times.
9. CO(1–0)—the most robustly calibrated gas mass tracer—may not be the best indicator of the column density of gas. Therefore, the "best calibration" will require excitation modeling of multiple CO lines, with a potential inclusion of [CI](1–0) as a promising alternative tracer.

To summarize, Vz-GAL is a unique large sample of comprehensive CO(1–0) measurements of homogeneously selected high-z dusty galaxies. With available higher-J CO lines along with continuum measurements from both Herschel (covering the dust SED peak) and NOEMA (z–GAL survey), the Vz-GAL forms a basis for future studies involving the understanding of multiphase ISM of these galaxies in the early Universe. For example, more precise gas mass, temperature, density, opacity, and the $\alpha_{\rm CO}$ conversion factor can be obtained from a combination of CO, [CI], and continuum observations via semiempirical, turbulent gas modeling (see K. C. Harrington et al. 2021), where CO(1–0) observations are essential for anchoring the CO SLEDs. Our forthcoming modeling efforts—along with follow-up [CI] observations—will not only facilitate a full-fledged characterization of these high-z DSFGs but also allow for the exploration of redshift evolution with respect to the varying temperature of the CMB (e.g., E. da Cunha et al. 2013).

The Vz-GAL CO(1–0) statistics will remain unrivaled in the northern sky until the advent of the next generation VLA (ngVLA[32]), which will be capable in incorporating fainter

---

[32] https://ngvla.nrao.edu/

and/or more distant DSFGs (E. J. Murphy et al. 2018). Recent and future Atacama Large Millimeter/submillimeter Array (ALMA) upgrades (J. Carpenter et al. 2023), however, have a potential to expand such CO(1–0) and CO(2–1) studies to the southern fields. In particular, Band 1 of ALMA (35–50 GHz) shares a common frequency range mainly with the VLA `Q` band, allowing it to cover CO(1–0) at $1.3 < z < 2.3$ and CO(2–1) at $3.6 < z < 5.6$ with better sensitivity.

Acknowledgments

We thank the anonymous referee for providing helpful suggestions. We are grateful to the staff at National Radio Astronomy Observatory (NRAO) for making the observations of this V*z*-GAL Large Program possible. The Karl G. Jansky Very Large Array (VLA) of NRAO is supported by the National Science Foundation (NSF). We thank Viral Parekh (Observatory Scientist, NRAO) for helping with a flux-scaling process for the flaring calibrator 3C138. The V*z*-GAL project benefited from the *z*–GAL (ANR-AAPG2019) of the French National Research Agency (ANR). P.P. is a member of the International Max Planck Research School (IMPRS) in Astronomy and Astrophysics. P.P., D.R., and A.W. acknowledge the Collaborative Research Center 1601 (SFB 1601 subproject C1 and C2) funded by the Deutsche Forschungsgemeinschaft (DFG, German Research Foundation)—500700252. P.P. thanks N. Sulzenauer and D. Colombo, SFB 1601 collaborators from Bonn, for valuable discussions. L.M. acknowledges financial support from the South African Department of Science and Innovation's National Research Foundation under the ISARP RADIOMAP Joint Research Scheme (DSI-NRF grant No. 150551) and the CPRR Projects (DSI-NRF grant No. SRUG2204254729).

Facility: VLA

Software: CASA (J. P. McMullin et al. 2007), CARTA (A. Comrie et al. 2024); Python v3.13 packages[33]: Astropy (Astropy Collaboration et al. 2022), Matplotlib (J. D. Hunter 2007), Numpy (C. R. Harris et al. 2020), Pandas (The pandas development team 2020), Scipy (P. Virtanen et al. 2020).

Data Availability

The full data release from the V*z*-GAL VLA Large Program (LP), including calibrated data cubes, continuum-subtracted spectra, moment maps, and CO(1–0) line measurements for 106 DSFGs, is publicly available at the V*z*-GAL website.[34] The data are provided in standard FITS format with accompanying machine-readable tables for line fluxes and source properties. Raw visibilities from the VLA observations are accessible via the NRAO Science Data Archive[35] under project codes `VLA/20A-083` (pilot sample), `VLA/23B-169` (LP), and `VLA/25A-099` (LP).

In addition, all of the figures depicted in this paper are available at doi:10.5281/zenodo.17664164. This also includes original files of integrated-intensity maps and spectra of all of the V*z*-GAL targets from this work that are summarized in Appendix B.4.

Data Usage and Citation

Researchers using the V*z*-GAL data products in published work are kindly asked to cite this paper and acknowledge the V*z*-GAL team; a suggested acknowledgment is *"This publication makes use of products from the Vz-GAL Large Program (VLA/20A-083, 23B-169, and 25A-099), which is based on data taken with the National Science Foundation (NSF)'s Karl G. Jansky Very Large Array (VLA/NRAO), and partially funded through the German Science Foundation (DFG) Collaborative Research Center SFB 1601. The National Radio Astronomy Observatory (NRAO) is a facility of the NSF operated under cooperative agreement by Associated Universities, Inc."*

Appendix A

A.1. Choice of CO–H_2 Conversion Factor

Although CO(1–0) observations enable us to derive robustly calibrated gas masses by directly providing $L'_{\rm CO}(1-0)$ without a need for knowing the excitation of the CO line ladder, the derivation still depends on the choice of $\alpha_{\rm CO}$ (Equation (2)). This conversion factor is speculated to be a function of the physical properties of galaxies (e.g., gas density, kinetic temperature, velocity dispersion, metallicity) in theoretical and semiempirical models (see D. Narayanan 2011; K. C. Harrington et al. 2021). However, the accepted Galactic value of this conversion factor is $\alpha_{\rm CO} \sim 4.3\,M_\odot$ (K km s^{-1} pc^2)$^{-1}$ (hereafter without units attached for easy readability), which is also considered to be applicable for other main-sequence galaxies (e.g., L. J. Tacconi et al. 2008; C. L. Carilli & F. Walter 2013; K. Sandstrom et al. 2014; T. M. Hughes et al. 2017; D. A. Riechers et al. 2020; T.-M. Wang et al. 2022). In contrast, assuming $\alpha_{\rm CO} \sim 0.8$ for local ULIRGs and high-*z* DSFGs has been a common practice (e.g., L. J. Tacconi et al. 2008; D. A. Riechers et al. 2011d, 2013; C. L. Carilli & F. Walter 2013; C. M. Casey et al. 2014; C. E. Sharon et al. 2016). This is commonly motivated by D. Downes & P. M. Solomon (1998), who derived this average conversion factor for a sample of 10 local ULIRGs based on a comparison of their enclosed dynamical masses to the results from radiative transfer models. Based on these results, R. Genzel et al. (2010) and E. Daddi et al. (2010) adopted a bimodal behavior of $\alpha_{\rm CO}$. In other words, the bimodality refers to two distinct values of $\alpha_{\rm CO}$ for normal star-forming disks on the SFR$-M_*$ main sequence (MS) and for starbursts lying above the MS due to their typically shorter gas depletion timescales (and higher star formation efficiency).

The bimodality of $\alpha_{\rm CO}$ has been debated for the past decade and has also been countered by theoretical models predicting a rather smooth distribution of $\alpha_{\rm CO}$ based on physical conditions in galaxies (see D. Narayanan 2011; D. Narayanan et al. 2012a, 2012b). In addition, correlation analyses of ^{12}CO(1–0) and ^{13}CO(1–0) observations of the central molecular zone in the Milky Way shows lower conversion factors than those seen in the disk (D. J. Fixsen et al. 1999; M. Kohno & Y. Sofue 2024), supporting $\alpha_{\rm CO}$ dependence on the physical conditions. However, its conclusive observational evidence with large statistics across a wide redshift range has been unavailable. L. Dunne et al. (2022) also discard the bimodality of $\alpha_{\rm CO}$ due to its inferred requirement for a dust conversion factor bimodality, which has never been observed.

---

[33] https://docs.python.org/3.13/reference/index.html

[34] https://vzgal.uni-koeln.de/

[35] https://data.nrao.edu/

Overall, there is no clear consensus in the literature about what generic value of the $\alpha_{\rm CO}$ conversion factor fits all of the observations, especially at earlier cosmic epochs in the relative lack of resolved observations and knowledge about the physical properties of the environment within DSFGs. Although these dusty systems are expected to have Milky Way–like metallicities, a number of factors may lower the $\alpha_{\rm CO}$ values, such as: (1) high gas temperature and velocity dispersions leading to enhanced CO emission, (2) diffuse or overlapping gas leading to more luminous CO per unit H_2 mass, and (3) starburst modes like local ULIRGs. Studying the $\alpha_{\rm CO}$ conversion factor that is determined by a balance between all of these different physical conditions within high-z galaxies requires semiempirical models (e.g., A. Weiß et al. 2005a; K. C. Harrington et al. 2021) that also show different $\alpha_{\rm CO}$ values for cold and warm gas within a galaxy.

However, we caution the reader that there could be a plausible discrepancy with the $\alpha_{\rm CO} \sim 4$ in regard to dynamical masses ($M_{\rm dyn} = M_{\rm gas} + M_*$) of the local ULIRGs and high-z systems. A few studies (e.g., D. Downes & P. M. Solomon 1998; A. D. Bolatto et al. 2013) have already pointed out that the Milky Way–like conversion factor often leads to an inconsistency with observed dynamical masses. However, assumptions in terms of the "virial coefficient" in dynamical mass calculations also remain uncertain depending on the galaxy structure/geometry and kinematics (N. M. Förster Schreiber et al. 2009; A. Agnello et al. 2014). Detailed investigation of galaxies with known stellar masses and resolved gas dynamics is a way forward to further characterize the rotation curves and dynamical masses of such systems in the early Universe. This also helps further constrain the derived gas masses (hence, the CO–H_2 conversion factors), but is beyond the scope of this work.

Due to a lack of conclusive evidence against the simplest assumption of a Milky Way–like conversion factor, we use $\alpha_{\rm CO} = 4$ (including the contribution from helium; see Table 3) for the purpose of statistical analyses of our large sample presented in this paper. In addition to the Vz-GAL DSFGs, we also apply the same conversion factor to all different populations; e.g., other high-z DSFGs, local MS galaxies, and ULIRGs, that are used for a comparison in Section 4. This assumption, while averaging over the variation in physical conditions across these galaxies, helps to highlight any additional trends within these populations. This $\alpha_{\rm CO}$ gives gas-to-dust mass ratios similar to those seen in local sources with solar and supersolar metallicity (discussed in Section 4.5) that are consistent given that high-z DSFGs are dusty and already metal-rich.

A.2. Vz-GAL Continuum Measurements

Although our observations were not designed to detect continuum emission, ∼40% of the targets show radio continuum emission above $2\sigma_c$. In Appendix B, we show continuum contours (in blue) overlaid on the CO moment-0 maps. Nine sources (HeLMS-17 W, HeLMS-19, HeLMS-24, HeLMS-27, HeLMS-41, HerBS-72, HerBS-108, HerBS-183, and HerBS-188) are detected above $5\sigma_c$ significance. Five of them (HeLMS-19, HeLMS-41, HerBS-183, HerBS-185, and HerBS-188) show confirmed foreground radio sources along the line of sight in VLASS.[36] Several other DSFGs appear to have their continuum potentially contaminated by an overlapping radio source on the plane of the sky. In the case of HeLMS-51, the continuum emission is significantly offset by 4″ to the west from the CO(1–0)-emitting DSFG, in line with a similar component seen in the z–GAL data (P. Cox et al. 2023), possibly revealing an unrelated source in the observed field. In addition, we detect multiple other serendipitous sources in various target fields (see Table 2 and observed radio maps in Appendix B). Here we have colored the continuum contours in magenta for all of the cases of unrelated radio sources within the field. Please see the details in Section 3.1.

Table 2
Serendipitous Continuum Detections of Sources that Are Not Related to the Targeted Vz-GAL DSFGs

Target Field	Radio Source	Position [R.A., decl.]	$\nu_{\rm cont}$ (GHz)	$S_{\rm cont}$ (mJy)	Signal-to-noise Ratio (SNR)
HeLMS-49	RC	[23:37:22.09, −06:47:51.76]	35	0.10 ± 0.02	5.8
HeLMS-51	RC	[23:26:17.26, −2:53:17.87]	28	0.11 ± 0.03	4.1
HeLMS-57	RC1	[00:35:19.53, 07:28:14.08]	30	0.09 ± 0.02	3.4
...	RC2	[00:35:19.81, 07:27:55.17]	30	0.14 ± 0.02	2.9
...	...	...	38	0.19 ± 0.05	2.1
HerS-20	RC	[01:02:45.52, 01:05:54.65]	29	0.09 ± 0.02	5.7
HerBS-191	RC	[12:47:53.32, 32:25:00.90]	25	0.09 ± 0.02	2.5
HerBS-204	RC	[13:29:09.81, 30:10:16.49]	25	0.11 ± 0.02	4.4

---

[36] https://science.nrao.edu/vlass

A.3. Vz-GAL Spectral Line Measurements

Here in Tables 3 (CO(1–0), this work), 4 (CO(2–1), this work), and 5 (CO(1–0), pilot), we present the spectral line properties of the Vz-GAL sample as discussed in Section 3.2.1.

Table 3

V*z*-GAL (This Work): CO(1–0) Line and Underlying Continuum Properties, Molecular Gas Masses, and Gas Depletion Times

Source	z–GAL $z_{\rm spec}$	$S_{\rm peak}$ (mJy)	$\Delta v_{\rm FWHM}$ (km s^{-1})	$I_{\rm CO(1-0)}$ (Jy km s^{-1})	$\mu L'_{\rm CO(1-0)}$[a] (10^{11} L_l)	$\left[\frac{4.0}{\alpha_{\rm CO}}\right]\mu M_{\rm H_2}$ (10^{11} $M_\odot$)	$\tau_{\rm dep}$ (Myr)	$\nu_{\rm cont}$ (GHz)[b]		$S_{\rm cont}$ (mJy)[c]		Line Significance[d]
								IF1	IF2	IF1	IF2	
HeLMS-1	1.9047	2.42 ± 0.21	372 ± 38	0.96 ± 0.13	1.82 ± 0.25[e]	7.27 ± 1.00[e]	142.70 ± 21.70	30.7	39.5	0.03 ± 0.01	<0.13	6σ
HeLMS-3	1.4199	3.63 ± 0.39	576 ± 58	2.22 ± 0.33	2.47 ± 0.37[e]	9.87 ± 1.46[e]	233.73 ± 41.50	47.1	⋯	<0.33	⋯	5σ
HeLMS-11	2.4834	0.84 ± 0.10	745 ± 74	0.67 ± 0.10	2.01 ± 0.30[e]	8.03 ± 1.21[e]	231.14 ± 36.33	32.5	⋯	<0.12	⋯	7σ
HeLMS-12	2.3699	2.05 ± 0.13	554 ± 41	1.21 ± 0.12	3.36 ± 0.33[e]	13.4 ± 1.34[e]	365.08 ± 41.20	27.1	34.1	<0.10	<0.27	11σ
HeLMS-14	1.6168	2.65 ± 0.25	516 ± 52	1.45 ± 0.20	2.05 ± 0.28[e]	8.21 ± 1.13[e]	384.49 ± 59.68	43.5	⋯	<0.39	⋯	5σ
HeLMS-16	2.8187	1.12 ± 0.08	1136 ± 114	1.35 ± 0.17	5.05 ± 0.64	20.2 ± 2.54	436.02 ± 58.28	30.0	38.5	0.08 ± 0.02	<0.21	11σ
HeLMS-17 WE	…	…	…	0.88 ± 0.10	2.32 ± 0.38	9.28 ± 0.92	259.59 ± 38.27	27.1	34.9	0.16 ± 0.03	<0.11	…
W	2.2972	0.56 ± 0.07	816 ± 117	0.49 ± 0.09	1.29 ± 0.24[e]	5.16 ± 0.96[e]	…	…	…	…	…	5σ
E	2.2983	0.28 ± 0.05	1312 ± 273	0.39 ± 0.11	1.03 ± 0.29	4.12 ± 1.16	…	…	…	…	…	3σ
HeLMS-19	4.6880	0.43 ± 0.07	337 ± 64	0.15 ± 0.04	1.29 ± 0.34[e]	5.18 ± 1.34[e]	57.18 ± 15.18	20.7	⋯	1.18 ± 0.06	⋯	3σ
HeLMS-20	2.1947	0.56 ± 0.07	990 ± 100	0.59 ± 0.09	1.44 ± 0.22[e]	5.75 ± 0.90[e]	197.14 ± 31.98	27.9	35.9	<0.11	<0.18	6σ
HeLMS-21	2.7710	1.11 ± 0.10	315 ± 35	0.37 ± 0.05	1.35 ± 0.18[e]	5.40 ± 0.73[e]	99.59 ± 14.35	30.4	38.5	0.06 ± 0.02	<0.08	6σ
HeLMS-23	1.4888	2.18 ± 0.26	391 ± 54	0.91 ± 0.16	1.10 ± 0.19[e]	4.39 ± 0.78[e]	143.92 ± 31.12	45.6	⋯	<0.13	⋯	6σ
HeLMS-24	4.9841	0.53 ± 0.12	596 ± 153	0.34 ± 0.12	3.10 ± 1.10[e]	12.4 ± 4.42[e]	147.12 ± 53.35	19.7	⋯	0.08 ± 0.02	⋯	4σ
HeLMS-25	2.1408	0.30 ± 0.05	1095 ± 110	0.35 ± 0.07	0.82 ± 0.16	3.26 ± 0.65	112.08 ± 23.51	28.4	36.5	0.04 ± 0.01	<0.07	5σ
HeLMS-26 EW	…	…	…	0.26 ± 0.03	0.90 ± 0.10	3.59 ± 0.36	123.91 ± 31.19	31.1	38.5	<0.05	<0.10	…
E	2.6899	0.65 ± 0.12	216 ± 46	0.15 ± 0.02	0.52 ± 0.05	2.07 ± 0.21	…	…	…	…	…	4σ
W	2.6875	0.24 ± 0.07	442 ± 156	0.11 ± 0.01	0.38 ± 0.04	1.52 ± 0.15	…	…	…	…	…	2σ
HeLMS-27	3.7652	0.39 ± 0.03	554 ± 48	0.23 ± 0.03	1.37 ± 0.18[e]	5.49 ± 0.72[e]	83.79 ± 11.60	21.5[f]	⋯	0.05 ± 0.01	⋯	8σ
HeLMS-28	2.5327	1.06 ± 0.08	697 ± 70	0.79 ± 0.10	2.45 ± 0.31[e]	9.80 ± 1.25[e]	328.89 ± 44.78	32.1	⋯	<0.08	⋯	13σ
HeLMS-31	1.9495	1.48 ± 0.15	532 ± 53	0.84 ± 0.08	1.66 ± 0.17[e]	6.64 ± 0.66[e]	284.56 ± 45.81	30.2	38.9	<0.12	<0.26	6σ
HeLMS-32 CN1N2	…	…	…	0.60 ± 0.10	0.96 ± 0.15	3.84 ± 0.35	25.72 ± 3.00	41.9	⋯	<0.06	⋯	…
C	1.7153	0.47 ± 0.10	493 ± 49	0.25 ± 0.07	0.40 ± 0.11	1.60 ± 0.44	…	…	…	…	…	3σ
N1	1.7153	0.58 ± 0.10	346 ± 71	0.21 ± 0.06	0.34 ± 0.09	1.36 ± 0.36	…	…	…	…	…	3σ
N2	1.7153	0.89 ± 0.10	148 ± 19	0.14 ± 0.04	0.22 ± 0.06	0.88 ± 0.24	…	…	…	…	…	2σ
HeLMS-34	2.2715	1.82 ± 0.16	411 ± 41	0.80 ± 0.11	2.06 ± 0.28[e]	8.24 ± 1.14[e]	183.11 ± 28.18	27.3	35.0	0.09 ± 0.03	<0.22	10σ
HeLMS-35	1.6684	1.71 ± 0.21	627 ± 90	1.14 ± 0.21	1.70 ± 0.31[e]	6.82 ± 1.25[e]	605.63 ± 117.32	42.6	⋯	<0.18	⋯	5σ
HeLMS-36	3.9802	0.21 ± 0.04	330 ± 70	0.07 ± 0.02	0.48 ± 0.13	1.92 ± 0.52	33.07 ± 9.10	18.2	23.0	<0.05	<0.04	5σ
HeLMS-37	2.7576	0.48 ± 0.06	416 ± 60	0.21 ± 0.03	0.76 ± 0.08	3.04 ± 0.30	89.19 ± 9.00	30.5	38.5	<0.05	<0.07	6σ
HeLMS-38	2.1898	1.27 ± 0.19	513 ± 51	0.69 ± 0.12	1.68 ± 0.29[e]	6.73 ± 1.17[e]	216.66 ± 39.89	28.0	36.0	0.06 ± 0.02	<0.09	6σ
HeLMS-39	2.7658	0.79 ± 0.08	575 ± 58	0.48 ± 0.07	1.75 ± 0.25	6.99 ± 1.01	256.93 ± 39.50	30.4	38.5	<0.07	<0.08	6σ
HeLMS-40 W1W2	…	…	…	0.53 ± 0.05	2.18 ± 0.22	8.72 ± 0.88	19.71 ± 2.00	27.6	32.5	0.05 ± 0.01	<0.10	…
W1	3.1445	0.32 ± 0.05	786 ± 79	0.27 ± 0.05	1.01 ± 0.22	4.04 ± 0.88	…	…	…	…	…	4σ
W2	3.1395	0.39 ± 0.05	629 ± 63	0.26 ± 0.05	1.17 ± 0.22[e]	4.68 ± 0.88[e]	…	…	…	…	…	5σ
HeLMS-41	2.3353	0.42 ± 0.06	547 ± 86	0.24 ± 0.05	0.66 ± 0.14[e]	2.65 ± 0.54[e]	99.96 ± 21.54	30.7[f]	⋯	0.20 ± 0.02	⋯	4σ
HeLMS-42	1.9558	1.46 ± 0.15	249 ± 25	0.39 ± 0.06	0.77 ± 0.12[e]	3.08 ± 0.48[e]	149.63 ± 25.15	30.2	38.8	<0.06	<0.12	2σ
HeLMS-43	2.2912	0.44 ± 0.12	460 ± 146	0.22 ± 0.09	0.56 ± 0.24	2.26 ± 0.94	78.66 ± 33.29	27.1	34.8	<0.07	<0.07	4σ
HeLMS-44	1.3700	<2.3	385 ± 16[g]	<0.89	<1.04[e]	<4.16[e]	<341.40	48.0	⋯	<0.19	⋯	$<2\sigma$
HeLMS-45	5.3998	0.35 ± 0.08	847 ± 227	0.32 ± 0.11	3.28 ± 1.10[e]	13.1 ± 4.57[e]	143.78 ± 50.81	15.9	⋯	0.06 ± 0.01	⋯	3σ
HeLMS-46	2.5772	0.66 ± 0.07	673 ± 67	0.47 ± 0.07	1.52 ± 0.22[e]	6.07 ± 0.90[e]	250.42 ± 39.51	32.5	⋯	<0.07	⋯	7σ
HeLMS-47 NS	…	…	…	0.90 ± 0.07	2.24 ± 0.16	8.97 ± 0.66	276.59 ± 44.29	27.7	35.6	<0.07	<0.10	…

Table 3
(Continued)

Source	z–GAL $z_{\rm spec}$	$S_{\rm peak}$ (mJy)	$\Delta v_{\rm FWHM}$ (km s^{-1})	$I_{\rm CO(1-0)}$ (Jy km s^{-1})	$\mu L'_{\rm CO(1-0)}$[a] (10^{11} L_l)	$\left[\frac{4.0}{\alpha_{\rm CO}}\right]\mu M_{\rm H_2}$ (10^{11} $M_\odot$)	$\tau_{\rm dep}$ (Myr)	$\nu_{\rm cont}$ (GHz)[b]		$S_{\rm cont}$ (mJy)[c]		Line Significance[d]
								IF1	IF2	IF1	IF2	
N	2.2232	0.64 ± 0.10	834 ± 135	0.57 ± 0.06	1.42 ± 0.14	5.68 ± 0.57	…	…	…	…	…	5σ
S	2.2232	0.71 ± 0.14	439 ± 100	0.33 ± 0.03	0.82 ± 0.08	3.29 ± 0.33	…	…	…	…	…	4σ
HeLMS-48	3.3514	0.88 ± 0.08	647 ± 64	0.61 ± 0.08	3.00 ± 0.40[e]	12.0 ± 1.59[e]	329.52 ± 46.56	23.2[f]	...	0.05 ± 0.01	…	8σ
HeLMS-49 CS	…	…	…	0.54 ± 0.03	1.34 ± 0.09[e]	5.35 ± 0.38[e]	176.55 ± 26.14	35.3	…	<0.05	…	…
C	2.2154	0.66 ± 0.1	426 ± 74	0.30 ± 0.03	0.74 ± 0.07	2.97 ± 0.30	…	…	…	…	…	5σ
S	2.2154	0.42 ± 0.1	548 ± 144	0.24 ± 0.03	0.59 ± 0.06	2.38 ± 0.24	…	…	…	…	…	3σ
HeLMS-50	2.0532	0.45 ± 0.05	1387 ± 139	0.66 ± 0.10	1.44 ± 0.22	5.76 ± 0.87	331.50 ± 53.86	29.2	37.6	<0.04	<0.08	5σ
HeLMS-51	2.1559	0.64 ± 0.06	888 ± 89	0.60 ± 0.08	1.43 ± 0.19[e]	5.72 ± 0.76[e]	361.01 ± 51.70	28.3	36.3	<0.03	<0.07	8σ
HeLMS-52	2.2092	1.22 ± 0.14	235 ± 30	0.31 ± 0.05	0.75 ± 0.12[e]	3.01 ± 0.49[e]	99.59 ± 17.72	27.8	35.7	0.09 ± 0.02	<0.06	7σ
HeLMS-54	2.7070	0.40 ± 0.08	564 ± 130	0.24 ± 0.07	0.84 ± 0.24	3.35 ± 0.98	154.66 ± 46.98	30.9	38.5	<0.05	<0.08	4σ
HeLMS-55	2.2834	1.28 ± 0.21	428 ± 43	0.58 ± 0.11	1.52 ± 0.29[e]	6.09 ± 1.15[e]	304.62 ± 59.80	27.2	34.9	0.05 ± 0.02	<0.13	7σ
HeLMS-56 CNW	…	…	…	0.46 ± 0.05	2.33 ± 0.10	9.32 ± 0.50	231.38 ± 37.20	25.7	…	0.02 ± 0.01	…	…
C	3.3909	0.26 ± 0.03	726 ± 75	0.20 ± 0.02	1.01 ± 0.10[e]	4.04 ± 0.40[e]	…	…	…	…	…	2σ
N	3.3909	0.36 ± 0.13	353 ± 152	0.14 ± 0.02	0.71 ± 0.07	2.83 ± 0.28	…	…	…	…	…	2σ
W	3.3909	0.52 ± 0.16	212 ± 77	0.12 ± 0.01	0.61 ± 0.06	2.43 ± 0.24	…	…	…	…	…	2σ
HeLMS-57	1.9817	0.68 ± 0.10	915 ± 154	0.66 ± 0.08	1.34 ± 0.15	5.38 ± 0.55	302.70 ± 32.22	29.9	38.5	0.16 ± 0.03	<0.10	5σ
HerS-2	2.0149	1.99 ± 0.17	684 ± 68	1.45 ± 0.19	3.04 ± 0.40[e]	12.2 ± 1.59[e]	341.05 ± 48.49	29.6	38.0	<0.16	<0.35	9σ
HerS-3	3.0608	2.02 ± 0.14	330 ± 27	0.71 ± 0.08	3.03 ± 0.34[e]	12.1 ± 1.37[e]	149.77 ± 41.86	28.2	32.5	0.10 ± 0.03	<0.17	7σ
HerS-5	1.4491	1.74 ± 0.23	721 ± 72	1.33 ± 0.22	1.54 ± 0.25[e]	6.15 ± 1.01[e]	346.64 ± 66.31	46.4	…	<0.37	…	4σ
HerS-7	1.9838	0.82 ± 0.14	636 ± 124	0.55 ± 0.14	1.13 ± 0.29	4.53 ± 1.14	193.19 ± 50.56	29.9	38.4	<0.05	<0.10	5σ
HerS-8	2.2431	0.48 ± 0.05	687 ± 89	0.35 ± 0.06	0.89 ± 0.15	3.55 ± 0.61	133.52 ± 24.19	27.5	35.4	<0.04	<0.06	6σ
HerS-10	2.4690	1.43 ± 0.15	475 ± 48	0.72 ± 0.11	2.16 ± 0.33[e]	8.63 ± 1.31[e]	332.94 ± 53.67	32.5	…	<0.13	…	4σ
HerS-11	4.6618	0.22 ± 0.07	681 ± 269	0.16 ± 0.08	1.33 ± 0.67	5.31 ± 2.66	73.57 ± 37.17	19.8	…	<0.09	…	3σ
HerS-12	2.2707	0.58 ± 0.06	1187 ± 119	0.73 ± 0.11	1.89 ± 0.28[e]	7.57 ± 1.14[e]	275.14 ± 45.15	27.3	35.1	<0.06	<0.08	6σ
HerS-13	2.4759	0.87 ± 0.08	439 ± 50	0.41 ± 0.06	1.22 ± 0.18[e]	4.88 ± 0.72[e]	130.58 ± 21.04	32.5	…	0.09 ± 0.02	…	7σ
HerS-14	3.3441	0.35 ± 0.05	926 ± 174	0.34 ± 0.08	1.70 ± 0.40[e]	6.81 ± 1.58[e]	126.56 ± 30.02	27.0	32.5	0.04 ± 0.01	<0.04	5σ
HerS-15	2.3019	1.10 ± 0.09	743 ± 74	0.87 ± 0.11	2.30 ± 0.29[e]	9.21 ± 1.16[e]	433.83 ± 59.07	27.0	34.7	<0.12	<0.20	7σ
HerS-16	2.1971	1.08 ± 0.14	724 ± 72	0.83 ± 0.14	2.04 ± 0.34[e]	8.16 ± 1.36[e]	386.29 ± 69.04	27.9	35.9	0.06 ± 0.02	<0.23	9σ
HerS-17	3.0186	0.61 ± 0.09	682 ± 68	0.44 ± 0.08	1.85 ± 0.33[e]	7.40 ± 1.34[e]	184.76 ± 34.73	28.5	32.5	<0.08	<0.08	4σ
HerS-18 E	1.6926	1.12 ± 0.16	558 ± 92	0.66 ± 0.14	1.02 ± 0.22[e]	4.08 ± 0.86[e]	…	42.1	…	<0.12	…	5σ
HerS-20	2.0792	1.61 ± 0.14	339 ± 34	0.58 ± 0.08	1.29 ± 0.18[e]	5.14 ± 0.71[e]	300.15 ± 45.65	29.0	37.2	0.06 ± 0.01	<0.16	10σ
HerBS-46	1.8349	0.56 ± 0.11	938 ± 94	0.56 ± 0.12	0.99 ± 0.21	3.97 ± 0.85	276.96 ± 61.78	41.2	…	<0.10	…	4σ
HerBS-48	3.1438	0.42 ± 0.07	713 ± 144	0.32 ± 0.08	1.43 ± 0.39	5.70 ± 1.43	120.95 ± 30.84	27.6	32.5	<0.08	<0.07	4σ
HerBS-50	2.9280	0.54 ± 0.05	621 ± 62	0.36 ± 0.05	1.44 ± 0.20[e]	5.76 ± 0.80[e]	401.50 ± 20.85	29.2	32.5	<0.07	<0.06	5σ
HerBS-51	2.1827	0.62 ± 0.10	448 ± 87	0.30 ± 0.07	0.71 ± 0.17	2.85 ± 0.68	116.70 ± 28.42	36.6	…	<0.05	…	5σ
HerBS-53 EW	1.4229	<1.2	543 ± 87[g]	<0.65	<0.76[e]	<3.03[e]	<342.65	47.1	…	<0.18	…	$<2\sigma$
HerBS-65	2.6858	0.49 ± 0.08	529 ± 103	0.28 ± 0.07	0.95 ± 0.24	3.80 ± 0.96	134.36 ± 35.20	34.7[f]	…	<0.06	…	5σ
HerBS-72	3.6380	0.57 ± 0.06	550 ± 56	0.33 ± 0.05	1.89 ± 0.28[e]	7.55 ± 1.13[e]	173.91 ± 33.26	24.3	…	0.04 ± 0.01	…	8σ
HerBS-78	3.7344	0.40 ± 0.06	508 ± 88	0.22 ± 0.05	1.28 ± 0.30	5.10 ± 1.18	107.36 ± 26.91	23.8	…	<0.03	…	5σ
HerBS-91 CE	2.4047	0.72 ± 0.08	567 ± 78	0.43 ± 0.08	1.24 ± 0.23[e]	4.96 ± 0.91[e]	172.40 ± 33.57	33.3	…	<0.12	…	4σ
HerBS-105	2.6695	2.35 ± 0.14	448 ± 45	0.18 ± 0.04	0.62 ± 0.14[e]	2.48 ± 0.56[e]	704.17 ± 93.80	32.1	…	<0.06	…	2σ
HerBS-108	3.7168	0.53 ± 0.05	561 ± 56	0.32 ± 0.04	1.85 ± 0.23[e]	7.41 ± 0.94[e]	152.26 ± 20.74	21.6[f]	…	0.07 ± 0.01	…	8σ
HerBS-109 SNW	…	…	…	…	…	…	…	44.0	…	<0.21	…	…
S	1.5843	1.52 ± 0.16	750 ± 74	1.21 ± 0.13	1.64 ± 0.16	6.56 ± 0.66	…	…	…	…	…	2σ
NW	1.5850	<0.81	662 ± 84[g]	<0.57	<0.78	<3.10	…	…	…	…	…	$<2\sigma$
HerBS-116	3.1547	0.42 ± 0.06	799 ± 80	0.36 ± 0.06	1.61 ± 0.27	6.42 ± 1.08	203.76 ± 35.35	30.2[f]	…	<0.04	…	7σ
HerBS-126	2.5875	0.33 ± 0.07	941 ± 238	0.33 ± 0.11	1.07 ± 0.36	4.27 ± 1.42	196.91 ± 66.57	32.6	…	<0.05	…	5σ

Table 3
(Continued)

Source	z–GAL $z_{\rm spec}$	$S_{\rm peak}$ (mJy)	$\Delta v_{\rm FWHM}$ (km s^{-1})	$I_{\rm CO(1-0)}$ (Jy km s^{-1})	$\mu L'_{\rm CO(1-0)}$[a] (10^{11} L_l)	$\left[\frac{4.0}{\alpha_{\rm CO}}\right]\mu M_{\rm H_2}$ (10^{11} $M_\odot$)	$\tau_{\rm dep}$ (Myr)	$\nu_{\rm cont}$ (GHz)[b]		$S_{\rm cont}$ (mJy)[c]		Line Significance[d]
								IF1	IF2	IF1	IF2	
HerBS-129	3.3077	0.53 ± 0.12	720 ± 186	0.41 ± 0.14	1.97 ± 0.68[e]	7.88 ± 2.72[e]	245.27 ± 85.47	26.8	34.8	<0.09	<0.08	4σ
HerBS-136	3.2884	0.38 ± 0.06	589 ± 116	0.24 ± 0.06	1.14 ± 0.29	4.58 ± 1.15	137.99 ± 35.68	27.1	32.5	<0.06	<0.05	4σ
HerBS-137	3.0408	0.31 ± 0.11	429 ± 180	0.14 ± 0.08	0.60 ± 0.34[e]	2.40 ± 1.35[e]	76.25 ± 43.31	28.5	34.5	<0.08	<0.08	2σ
HerBS-143	2.2406	0.46 ± 0.05	1077 ± 148	0.53 ± 0.09	1.33 ± 0.23	5.33 ± 0.91	340.73 ± 61.08	36.0	…	<0.04	…	7σ
HerBS-157	1.8971	0.33 ± 0.13	787 ± 79	0.28 ± 0.11	0.52 ± 0.21	2.08 ± 0.83	189.09 ± 76.21	30.8	39.5	<0.07	<0.15	2σ
HerBS-162 SWNE	…	…	…	0.33 ± 0.02	0.99 ± 0.05	3.96 ± 0.30	…	33.6	…	<0.04	…	…
SW	2.4739	0.47 ± 0.12	305 ± 94	0.15 ± 0.02	0.45 ± 0.05	1.80 ± 0.20	…	…	…	…	…	3σ
NE	2.4742	0.42 ± 0.10	408 ± 116	0.18 ± 0.02	0.54 ± 0.05	2.16 ± 0.22	…	…	…	…	…	3σ
HerBS-165	2.2251	0.57 ± 0.08	516 ± 83	0.31 ± 0.07	0.78 ± 0.18	3.12 ± 0.70	228.60 ± 53.40	27.7	35.7	<0.05	<0.11	5σ
HerBS-167	2.2144	0.32 ± 0.06	952 ± 196	0.32 ± 0.09	0.80 ± 0.22	3.21 ± 0.89	273.64 ± 77.46	27.8	35.7	<0.05	<0.17	3σ
HerBS-169	2.6977	0.57 ± 0.09	535 ± 99	0.32 ± 0.08	1.13 ± 0.28	4.50 ± 1.11	171.30 ± 43.65	32.2	…	<0.04	…	5σ
HerBS-171	2.4793	0.48 ± 0.05	451 ± 59	0.23 ± 0.04	0.69 ± 0.12	2.77 ± 0.48	151.11 ± 27.69	32.6	…	<0.07	…	5σ
HerBS-176	2.9805	0.50 ± 0.10	894 ± 197	0.48 ± 0.14	1.95 ± 0.57[e]	7.79 ± 2.29[e]	288.20 ± 86.14	30.9[f]	…	<0.06	…	4σ
HerBS-177	3.9625	0.55 ± 0.06	571 ± 76	0.33 ± 0.06	2.16 ± 0.39[e]	8.66 ± 1.55[e]	176.11 ± 32.96	22.7	…	0.02 ± 0.01	…	9σ
HerBS-179	3.9423	0.53 ± 0.16	310 ± 109	0.17 ± 0.08	1.12 ± 0.51	4.49 ± 2.06	106.95 ± 49.23	22.8	…	0.05 ± 0.01	…	2σ
HerBS-183	1.8919	1.34 ± 0.16	624 ± 62	0.89 ± 0.14	1.67 ± 0.26[e]	6.67 ± 1.05[e]	590.04 ± 100.73	35.2[f]	…	0.39 ± 0.02	…	7σ
HerBS-185	4.3238	0.23 ± 0.06	632 ± 178	0.15 ± 0.06	1.15 ± 0.44[e]	4.59 ± 1.78[e]	93.92 ± 36.96	21.1	…	0.02 ± 0.01	…	4σ
HerBS-187 EW	…	…	…	…	…	…	>210.24	41.2	…	<0.13	…	…
E	1.8285	<0.25	591 ± 76[g]	<0.16	<0.28	<1.13	…	…	…	…	…	$<2\sigma$
W	1.8274	0.64 ± 0.11	517 ± 106	0.35 ± 0.09	0.62 ± 0.16	2.48 ± 0.64	…	…	…	…	…	3σ
HerBS-188	2.7675	0.24 ± 0.04	987 ± 192	0.25 ± 0.06	0.91 ± 0.22	3.65 ± 0.87	141.75 ± 34.77	34.5[f]	…	0.31 ± 0.03	…	4σ
HerBS-190	2.5890	0.52 ± 0.06	755 ± 107	0.42 ± 0.08	1.35 ± 0.26	5.41 ± 1.04	249.12 ± 49.96	32.7	…	<0.09	…	5σ
HerBS-191	3.4428	0.20 ± 0.05	1751 ± 490	0.37 ± 0.14	1.93 ± 0.72	7.72 ± 2.90	246.26 ± 93.48	25.4	…	0.04 ± 0.01	…	3σ
HerBS-193	3.6951	0.31 ± 0.03	849 ± 110	0.28 ± 0.05	1.62 ± 0.29	6.49 ± 1.16	144.84 ± 26.94	24.1	…	0.02 ± 0.01	…	6σ
HerBS-194 NS	…	…	…	…	…	…	>135.24	27.0	34.4	<0.05	<0.07	…
N	2.3335	0.26 ± 0.05	862 ± 194	0.24 ± 0.07	0.65 ± 0.19	2.60 ± 0.76	…	…	…	…	…	3σ
S	2.3316	<0.20	538 ± 140[g]	<0.12	<0.32	<1.30	…	…	…	…	…	$<2\sigma$
HerBS-204 EW	…	…	…	0.40 ± 0.08	2.12 ± 0.23	8.48 ± 0.90	190.78 ± 20.52	25.1	…	<0.04	…	…
E	3.4937	0.31 ± 0.08	581 ± 163	0.19 ± 0.03	1.01 ± 0.11	4.04 ± 0.41	…	…	…	…	…	3σ
W	3.4933	0.37 ± 0.08	536 ± 131	0.21 ± 0.07	1.11 ± 0.13	4.44 ± 0.45	…	…	…	…	…	3σ

Notes.

[a] Given in units of L_l = K km s^{-1} pc^2.

[b] For the targets with the values given only for IF1, it represents the central frequency of a continuous 2 GHz wide band, where the IF1 and IF2 are adjacent to each other. Please refer to Section 2.2 for more details.

[c] For continuum nondetections (SNR < 2), we provide the $3\sigma_c$ upper limits on the continuum flux densities (assuming an unresolved emission within a beam), where σ_c is the rms noise of a given continuum map.

[d] CO(1–0) or CO(2–1) line detection level in terms of σ, the rms noise of the integrated-intensity (moment-0) map.

[e] Line luminosities and gas masses of lensed DSFG candidates. Many of these targets have a known lensing factor $\mu > 1$ from E. Borsato et al. (2024).

[f] `CASA tclean mfs`-mode-based net central frequency for a combined continuum of individual IF1 and IF2 detections at two different central frequencies.

[g] For nondetections (SNR < 2) in CO(1−0), FWHM values are from z–GAL mid-J CO line results. The upper limit on the CO(1–0) line flux of HeLMS-44 has been derived using the linewidth from the z–GAL CO(2–1) spectrum.

(This table is available in machine-readable form in the online article.)

Table 4

Vz-GAL (This Work): CO(2–1) Line and Underlying Continuum Properties

Source	$z_{\rm spec}$	$S_{\rm peak}$ (mJy)	$\Delta v_{\rm FWHM}$ (km s^{-1})	$I_{\rm CO(2-1)}$ (Jy km s^{-1})	$\mu L'_{\rm CO(2-1)}$[a] (10^{11} L_l)	$\nu_{\rm cont}$ (GHz)[b]		$S_{\rm cont}$ (mJy)[c]		Line Significance[d]
						IF1	IF2	IF1	IF2	
HeLMS-19	4.6880	4.29 ± 0.45	288 ± 35	1.31 ± 0.21	2.76 ± 0.44[e]	41.1	⋯	0.87 ± 0.10	⋯	5σ
HeLMS-24	4.9841	2.26 ± 0.14	691 ± 50	1.66 ± 0.16	3.83 ± 0.37	34.4[f]	⋯	0.09 ± 0.02	⋯	11σ
HeLMS-27	3.7652	2.07 ± 0.56	599 ± 189	1.32 ± 0.12	1.95 ± 0.18[e]	43.0	48.2	<0.14	<0.35	2σ
HeLMS-36	3.9802	0.78 ± 0.15	309 ± 67	0.26 ± 0.07	0.42 ± 0.11	45.6	⋯	<0.15	⋯	3σ
HeLMS-45	5.3998	1.06 ± 0.10	515 ± 56	0.58 ± 0.08	1.51 ± 0.21	28.2	36.1	<0.09	<0.18	8σ
HerS-11	4.6618	1.66 ± 0.17	462 ± 55	0.82 ± 0.13	1.70 ± 0.27	41.2	⋯	<0.19	⋯	7σ
HerBS-78	3.7344	0.95 ± 0.29	639 ± 224	0.65 ± 0.06	0.96 ± 0.10	48.1	⋯	<0.18	⋯	3σ
HerBS-177	3.9625	1.49 ± 0.23	593 ± 104	0.94 ± 0.10	1.52 ± 0.15[e]	45.9	⋯	<0.13	⋯	5σ
HerBS-179	3.9423	1.23 ± 0.38	385 ± 137	0.50 ± 0.05	0.80 ± 0.10	46.1	⋯	<0.19	⋯	2σ
HerBS-185	4.3238	0.97 ± 0.15	469 ± 83	0.48 ± 0.11	0.90 ± 0.20[e]	42.7	⋯	<0.17	⋯	4σ

Notes.

[a] Given in units of L_l = K km s^{-1} pc^2.

[b] For the targets with the values given only for IF1, it represents the central frequency of a continuous 2 GHz wide band, where the IF1 and IF2 are adjacent to each other. Please refer to Section 2.2 for more details.

[c] For continuum nondetections (SNR < 2), we provide the $3\sigma_c$ upper limits on the continuum flux densities (assuming an unresolved emission within a beam), where σ_c is the rms noise of a given continuum map.

[d] CO(1–0) or CO(2–1) line detection level in terms of σ, the rms noise of the integrated-intensity (moment-0) map.

[e] Line luminosities and gas masses of lensed DSFG candidates. Many of these targets have a known lensing factor $\mu > 1$ from E. Borsato et al. (2024).

[f] `CASA tclean mfs`-mode-based net central frequency for a combined continuum of individual IF1 and IF2 detections at two different central frequencies.

[g] For nondetections (SNR < 2) in CO(1−0), FWHM values are from z–GAL mid-J CO line results. The upper limit on the CO(1–0) line flux of HeLMS-44 has been derived using the linewidth from the z–GAL CO(2–1) spectrum.

(This table is available in machine-readable form in the online article.)

Table 5

V*z*-GAL Pilot Program DSFGs from F. Stanley et al. (2023): CO(1–0) Line and Underlying Continuum Properties, Molecular Gas Masses, and Gas Depletion Times Adapted to $\alpha_{\rm CO} = 4M_\odot$ (K km s^{-1} pc^2)$^{-1}$

Source	$z_{\rm spec}$	$S_{\rm peak}$ (mJy)	$\Delta\nu_{\rm FWHM}$ (km s^{-1})	$I_{\rm CO(1-0)}$ (Jy km s^{-1})	$\mu L'_{\rm CO(1-0)}$[a] (10^{11} L_l)	$\left[\frac{4.0}{\alpha_{\rm CO}}\right]\mu M_{\rm H_2}$ (10^{11} $M_\odot$)	$\tau_{\rm dep}$ (Myr)	$\nu_{\rm cont}$ (GHz)		$S_{\rm cont}$ (mJy)[b]		Line Significance[c]
								IF1	IF2	IF1	IF2	
HerBS-34	2.633	0.7 ± 0.12	593 ± 112	0.44 ± 0.11	1.5 ± 0.4	6.0 ± 1.6	150 ± 40	32.0	…	<0.03	…	4σ
HerBS-43a	3.212	0.3 ± 0.06	1166 ± 249	0.37 ± 0.10	1.7 ± 0.5	6.8 ± 2.0	200 ± 70	22.2	…	0.024 ± 0.007	…	5σ
HerBS-43b	4.054	0.08 ± 0.03	744 ± 290	0.064 ± 0.033	0.4 ± 0.2	1.6 ± 0.8	110 ± 50	22.2	…	0.019 ± 0.003	…	5σ
HerBS-44	2.927	0.95 ± 0.14	377 ± 63	0.38 ± 0.08	1.5 ± 0.3	6.0 ± 1.2	50 ± 10	29.2	38.5	<0.05	<0.08	6σ
HerBS-54	2.442	0.8 ± 0.11	1087 ± 176	0.92 ± 0.19	2.7 ± 0.6	10.8 ± 2.4	450 ± 110	33.1	…	0.072 ± 0.13	…	5σ
HerBS-58	2.084	2.12 ± 0.32	363 ± 64	0.82 ± 0.19	1.8 ± 0.4	7.2 ± 1.6	410 ± 90	28.8	37.3	<0.04	<0.06	4σ
HerBS-70E	2.308	0.49 ± 0.09	622 ± 130	0.32 ± 0.09	0.9 ± 0.2	3.6 ± 0.8	90 ± 30	27.1	34.8	0.60 ± 0.02	0.47 ± 0.02	4σ
HerBS-70W	2.311	0.83 ± 0.15	197 ± 39	0.17 ± 0.04	0.5 ± 0.1	2.0 ± 0.4	230 ± 120	27.1	34.8	<0.03	<0.03	5σ
HerBS-79	2.078	1.24 ± 0.17	787 ± 125	1.04 ± 0.22	2.3 ± 0.5[d]	9.2 ± 2.0[d]	510 ± 120	28.7	37.5	<0.03	<0.04	5σ
HerBS-89a	2.949	0.64 ± 0.09	1586 ± 247	1.08 ± 0.22	4.4 ± 0.9[d]	17.6 ± 3.6[d]	610 ± 130	29.2	38.5	<0.06	<0.15	5σ
HerBS-95E	2.972	0.2 ± 0.04	658 ± 137	0.14 ± 0.04	0.6 ± 0.2	2.4 ± 0.8	210 ± 80	29.0	38.5	<0.02	<0.06	5σ
HerBS-95W	2.973	0.95 ± 0.12	522 ± 76	0.52 ± 0.10	2.2 ± 0.4	8.8 ± 1.6	550 ± 120	29.0	38.5	<0.02	<0.06	7σ
HerBS-113	2.787	1.46 ± 0.21	497 ± 81	0.77 ± 0.16	2.9 ± 0.6[d]	11.6 ± 2.4[d]	390 ± 90	30.4	38.5	<0.05	<0.07	4σ
HerBS-154	3.707	0.95 ± 0.11	384 ± 54	0.39 ± 0.07	2.3 ± 0.4[d]	9.2 ± 1.6[d]	120 ± 30	19.2	24.4	<0.07	<0.03	5σ

Notes.

[a] Given in units of L_l = K km s^{-1} pc^2.

[b] For continuum nondetections (SNR < 2), we provide the $3\sigma_c$ upper limits on the continuum flux densities (assuming an unresolved emission within a beam), where σ_c is the rms noise of a given continuum map.

[c] CO(1–0) line detection level in terms of σ, the rms noise of the integrated-intensity (moment-0) map.

[d] Line luminosities and gas masses of lensed DSFG candidates. The signatures of their lensed nature can be seen in S. Berta et al. (2021) and F. Stanley et al. (2023).

(This table is available in machine-readable form in the online article.)

Appendix B

B.1. *Comparison of the* L$_{IR}$ *(hence, Dust Temperature) and the SFE Proxy of Galaxy Populations at Cosmic Noon*

To avoid the dust temperature–redshift degeneracy, Figure 9 compares the total infrared luminosity and SFE proxy of galaxies at $z = 2$–3. Please see footnote 29 in Section 4.2 for details.

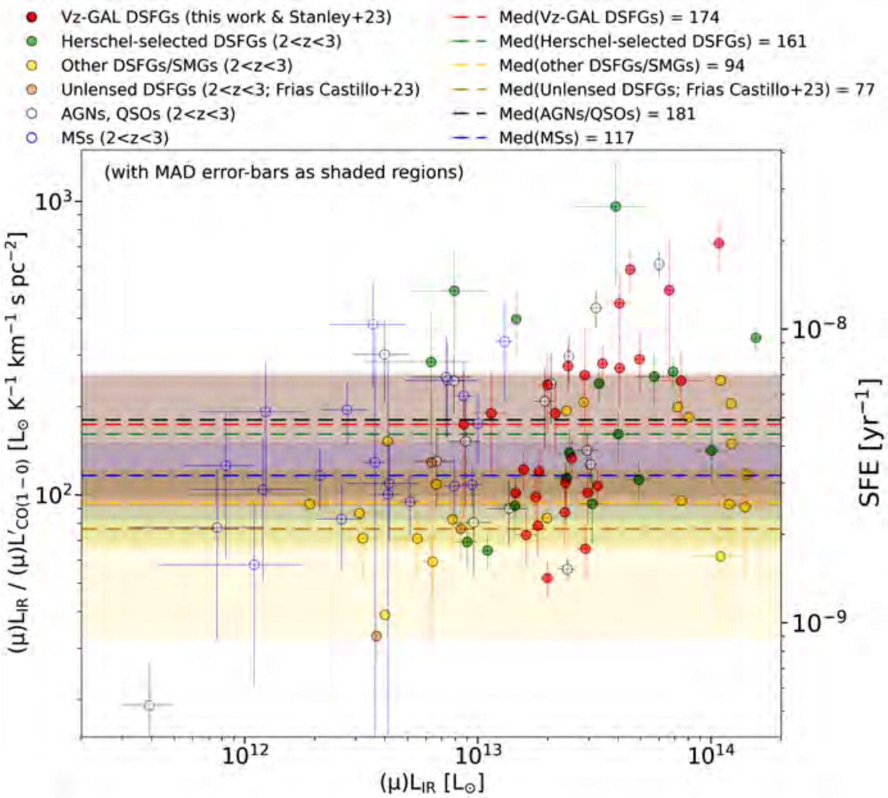

Figure 9. A comparison of $L_{\rm IR}/L'_{\rm CO}(1-0)$ ratio, a proxy for SFE, with respect to the 8–1000 μm luminosity ($L_{\rm IR}$) for various galaxy populations around cosmic noon ($z = 2$–3). The median ratios for these galaxy populations are comparable within the (unscaled) median absolute deviation (MAD) error bars, modulo a few outliers from each population.

B.2. Vz-GAL Sources with Extreme CO Line Ratios

In Table 6, we present the Vz-GAL sources that have extreme CO line ratios. Please see Section 4.4 for more details.

Table 6
Vz-GAL DSFGs with Extreme Line Ratios

	SNR > 5						SNR $\leqslant 5$					
	Superthermal			Subthermal			Superthermal			Subthermal		
	(with $r_{J1} > 1$)			(with $r_{J1} < 0.2$)			(with $r_{J1} > 1$)			(with $r_{J1} < 0.2$)		
Ratio	DSFG	Value	Detection	DSFG	Value	Detection	DSFG	Value	Detection	DSFG	Value	Detection
r_{21}	HeLMS-1	1.08 ± 0.16	6σ	…	…	…	HeLMS-19	2.14 ± 0.66	3σ	HerBS-109 S	0.19 ± 0.10	2σ
...	HeLMS-3	1.27 ± 0.21	5σ	…	…	…	HeLMS-24	1.24 ± 0.45	4σ	…	…	…
...	HeLMS-14	1.49 ± 0.22	5σ	…	…	…	HeLMS-42	1.24 ± 0.43	2σ	…	…	…
...	HeLMS-27	1.42 ± 0.23	8σ	…	…	…	HerS-11	1.28 ± 0.68	3σ	…	…	…
...	HeLMS-31	1.49 ± 0.21	6σ	…	…	…	HerBS-157	1.39 ± 0.64	2σ	…	…	…
...	HeLMS-57	1.05 ± 0.25	5σ	…	…	…	…	…	…	…	…	…
...	HerS-2	1.13 ± 0.19	9σ	…	…	…	…	…	…	…	…	…
...	HerS-7	1.78 ± 0.60	5σ	…	…	…	…	…	…	…	…	…
...	HerS-18E	1.79 ± 0.42	5σ	…	…	…	…	…	…	…	…	…
r_{31}	HeLMS-3	1.04 ± 0.17	5σ	HeLMS-28	0.17 ± 0.03	13σ	HeLMS-43	1.61 ± 0.86	4σ	HerBS-105	0.13 ± 0.08	2σ
...	HeLMS-14	1.08 ± 0.16	5σ	HerBS-108	0.10 ± 0.04	8σ	HerBS-48	1.26 ± 0.42	4σ	HerBS-109 S	0.19 ± 0.10	2σ
...	HeLMS-52	1.19 ± 0.23	7σ	…	…	…	HerBS-137	1.14 ± 0.71	2σ	…	…	…
...	HerS-13	1.13 ± 0.23	7σ	…	…	…	…	…	…	…	…	…
...	HerS-14	1.08 ± 0.16	5σ	…	…	…	…	…	…	…	…	…
...	HerS-18E	1.20 ± 0.27	5σ	…	…	…	…	…	…	…	…	…
r_{41}	HerS-14	1.13 ± 0.30	5σ	HerBS-126	0.15 ± 0.06	5σ	HeLMS-19	1.33 ± 0.42	3σ	HerBS-167	0.19 ± 0.09	3σ
...	HerS-20	1.27 ± 0.27	10σ	...	...	...	HeLMS-24	1.14 ± 0.42	4σ	…	…	…
r_{51}	...	…	…	HeLMS-48	0.20 ± 0.04	8σ	…	…	…	HerBS-105	0.06 ± 0.04	2σ
r_{61}	...	…	…	HerBS-72	0.14 ± 0.03	8σ	…	…	…	…	…	…
...	...	…	…	HerBS-193	0.15 ± 0.03	6σ	…	…	…	…	…	…

Note. Most of the superthermal ratios are consistent with being $r_{J1} \leqslant 1$ (subthermal) within the 1σ error bars and given that the total uncertainty due to the flux calibration is 10%–15% (see Section 3.1).

B.3. Comments on Individual DSFGs with Novel Spectral and Spatial Features

In this section, we comment on individual sources of the Vz-GAL survey, highlighting new aspects revealed by the VLA CO(1–0) or the continuum observations, and commenting on any characteristics found in the fields where they are located. The sources here discussed are listed in their order of appearance in the tables and figures.

HeLMS-1. This AGN-starburst galaxy is amplified by a foreground galaxy group at $z \sim 0.5$ (seen in Hubble Space Telescope, HST, imaging; E. Borsato et al. 2024), into a bright northeastern arc and a weaker image $\sim 8''$ to the southwest (P. Cox et al. 2023; E. Borsato et al. 2024). Only the northern image is clearly detected in the CO(1–0) emission line and has $3\sigma_c$ detection at 30 GHz in the continuum emission (0.03 ± 0.01 mJy). The southern image has only a 3σ upper limit in CO(1–0) of 0.43 Jy km s^{-1}, which remains compatible with the relatively weak CO(4$-$3) emission line (5.10 ± 0.45 Jy km s^{-1}).

HeLMS-3. This source has the strongest CO(3$-$2) and CO(2–1) emission lines in the z–GAL survey (11.24 ± 0.86 and 20.72 ± 1.55 Jy km s^{-1}, respectively) and also the strongest CO(1–0) emission line of the entire Vz-GAL sample with 2.22 ± 0.33 Jy km s^{-1}. HeLMS-3 is gravitationally amplified by a foreground galaxy group seen in HST F110W imaging (E. Borsato et al. 2024). The north–south extension, which was apparent in the NOEMA data, is clearly seen in the Vz-GAL CO(1–0) moment-0 map, which shows a strong image to the south and a weaker one to the north.

HeLMS-14. The CO(1–0) emission of HeLMS-14 is resolved into two arc-like structures located east and west with a separation of $\sim 4''$. This source is gravitationally lensed by a foreground galaxy at $z = 0.26$ seen in the HST F110W image that also reveals an almost complete ring of the background source with a radius of $r \sim 4''$ with clear substructures (E. Borsato et al. 2024). The two arcs seen in the CO(1–0) emission follow the extent of the rest-frame optical ring structure.

HeLMS-17. The field of HeLMS-17 contains a single source to the east with a spectroscopic redshift of $z = 2.2983$ and a double source to the west, with two close-by ($\sim 4''$) components (W1 and W2) that have the same redshift $z = 2.2972$ (P. Cox et al. 2023). The western source is aligned with a galaxy seen in the HST F110W image and is therefore probably lensed. Both the eastern and western sources are detected in the CO(1–0) emission line with broad profiles that are comparable to the higher-J CO lines ($\Delta v = 1312 \pm 273$ and 816 ± 117 km s^{-1} for the eastern and western sources, respectively). The western source shows a distinct, although weak, CO(1–0) extension to the east that corresponds to the position of the second component (W2). The continuum emission is detected at 27 GHz in the western source with a flux density of 0.16 ± 0.03 mJy, but not at 35 GHz with an upper limit of $\sigma_c = 0.11$ mJy.

HeLMS-19. This source is lensed by a foreground $z = 0.14$ galaxy into a large Einstein ring with two main arcs, separated by $\sim 5''$, that are partially traced in HST F110W imaging (E. Borsato et al. 2024). The two arcs were detected in multiple emission lines (CO(4$-$3), (5$-$4) and (7$-$6) and in the two [CI] transitions) and in the dust continuum with NOEMA (P. Cox et al. 2023). Both arcs are also seen in CO(1–0) and CO(2$-$1). The strong continuum emission, which is detected at 41.1 GHz (0.87 ± 0.10 mJy) and 20.7 GHz (1.18 ± 0.06 mJy), peaks at the center of the Einstein ring and most likely traces the radio continuum of the foreground galaxy.

HeLMS-20. The CO(1–0) emission line of this source shows a well-defined, broad (990 ± 100 km s^{-1}) double-Gaussian profile. Similar profiles are found in the CO(4$-$3) and [CI](1$-$0) emission lines from the z–GAL survey, although the weaker redshifted component was not identified in P. Cox et al. (2023). As a result, we revise the spectroscopic redshift of this source ($z = 2.1947$) reported by P. Cox et al. (2023) to $z = 2.1975$.

HeLMS-26. The two sources that were detected in the higher-J CO lines to the east and the west around the Herschel position, separated by $\sim 12''$ (corresponding to a linear distance of ~ 100 kpc), are clearly detected in CO(1–0) displaying the similar broad and narrow line widths as in the high-J CO lines for the west and east sources, respectively.

HeLMS-32. The weak central source, which was detected in CO(2$-$1) and CO(3$-$2), is also seen in the CO(1–0) emission line. At the same redshift, to the north, two other sources, N1 and N2, are tentatively detected in CO(1–0) emission. None of these sources were detected in the z–GAL survey (P. Cox et al. 2023).

HeLMS-40. Two sources were detected in the NOEMA field, W1 and W2, separated by $\sim 4''$, at slightly different redshifts of $z = 3.1445$ and $z = 3.1395$ (P. Cox et al. 2023). We detect both in CO(1–0) emission with similar profiles as in the higher-J CO transitions. The source W2 is aligned with a visible galaxy ($z = 0.821$) seen in the HST F110W imaging (H. Nayyeri et al. 2016b; E. Borsato et al. 2024). Both sources have also been been observed in the 873 μm continuum with ALMA (A. Amvrosiadis et al. 2018) and both W1 and W2 have recently each been resolved into two components (Bakx et al. 2025, in preparation).

HeLMS-47. This source is resolved in the CO(1–0) emission line showing two strong peaks to the northeast and the southwest separated by $\sim 4''$, in line with the extension that was seen in the NOEMA data (P. Cox et al. 2023).

HeLMS-49. The source is resolved in CO(1–0) , revealing an emission peak at the center and a slightly weaker peak to the southwest, separated by $\sim 5''$. Aligned with a galaxy seen in the HST F110W image (E. Borsato et al. 2024), HeLMS-49 is likely gravitationally amplified. The spectroscopic redshift of HeLMS-49 was measured based on the detection of water and atomic carbon emission lines (P. Cox et al. 2023), preventing, to date, an analysis of CO for this galaxy.

HeLMS-50. The CO(1–0) emission-line profile of this source shows a well-defined, broad (1837 ± 139 km s^{-1}) double Gaussian. A close comparison with the profiles of the CO(3$-$2) and (4$-$3) emission lines from the z–GAL survey shows that the profiles of all three lines are comparable, although the weaker blueshifted component was not identified by P. Cox et al. (2023). As a result, the spectroscopic redshift of this source is revised from $z = 2.0532$ to $z = 2.0515$.

HeLMS-51. This source is lensed as it is aligned with a galaxy seen in HST F110W imaging (E. Borsato et al. 2024). To the west of HeLMS-51, a source is detected in the 28 GHz continuum with a flux density of 0.11 ± 0.03 mJy. Aligned with another galaxy seen in the HST F110W image, this source is unrelated to HeLMS-51.

HeLMS-56. The main central source at $z = 3.391$, which was detected in z–GAL, is clearly detected in CO(1–0) emission, displaying a similar double-Gaussian line profile as the high-J CO transitions. This central source is aligned with a galaxy seen in HST F110W imaging (E. Borsato et al. 2024) and is therefore likely lensed. Two additional sources in the field of HeLMS-56, which are at the same redshift as the central source, are detected in CO(1–0)—one 12″ to the north and the other 13″ to the west, corresponding to linear distances of ∼100 kpc. Both sources have comparable line fluxes and display single Gaussian profiles, contrary to the central source.

HerS-3. This source is an Einstein cross with a fifth central image that is described in detail by P. Cox et al. (2025). The CO(1–0) emission line clearly reveals the strong northern and southern images, while the three images along the east–west axis are barely resolved apart. The continuum is also detected, mostly along the north–south elongation, at 28 GHz but remains undetected at 32.5 GHz.

HerS-7. The CO(1–0) emission of this source is dominated by a strong central component, which was also detected in the CO(2–1) and CO(4–3) emission lines (P. Cox et al. 2023). The second weaker component, ∼3.″5 to the east, is also detected in CO(1–0) with a slightly redshifted velocity of ∼250 km s^{-1}. The two other sources in the field that were only detected in the millimeter continuum emission, one ∼11″ to the north and a weaker source ∼12″ to the west, remain undetected in the current Vz-GAL data.

HerS-10. This source is aligned with a bright galaxy seen in HST F110W imaging (E. Borsato et al. 2024) and is gravitationally amplified. The CO(1–0) emission displays the same double-peaked profile as CO(3−2) and shows an extension in the east–west direction, which could be compatible with an arc-like structure or two sides of an incomplete Einstein ring, as is seen in ALMA 350 GHz imaging.

HerS-13. This source is spatially unresolved in CO(1−0). Its CO(1–0) line shape is interesting, given that it shows signatures of a potential differential magnification across the blue and red sides of the spectrum. HST F110W imaging (E. Borsato et al. 2024) of the field shows a foreground galaxy that is lensing HerS-13, which is also consistent with an incomplete Einstein ring seen in ALMA 350 GHz imaging.

HerS-18. This source also has a spatial component in the west (see P. Cox et al. 2023), which is at $z = 0.56$ and, hence, outside our observational range for the CO(1–0) transition.

HerBS-91. The CO(1–0) moment-0 map reveals two eastern and central sources that were also detected in the higher-J CO lines at the same redshift ($z = 2.4047$ P. Cox et al. 2023). To enhance the SNR, the spectra of both components have been combined.

HerBS-109. Three distinct components were detected for this source in the z–GAL survey: the northwestern and southern components, separated by 12″ and having similar redshifts of $z = 1.5850$ and 1.5843, respectively, and a component to the northeast at $z = 2.8385$ that is unrelated to the binary system (P. Cox et al. 2023). The CO(1–0) emission line is only detected in the southern component and remained undetected in the northwest component. Further, the receiver band used for these observations did not include the frequency of the redshifted CO(1–0) emission line of the northeast component.

HerBS-116. This source was resolved into two components in the 2 mm continuum emission, located in the east and west, and separated by ∼4″, which are both at the same redshift $z = 3.1573$ (P. Cox et al. 2023). The CO(1–0) emission peaks at the stronger eastern component and shows an extension toward the west that coincides with the second weaker component of this system. Since no galaxy is visible in HST FW110 imaging or in the SDSS (E. Borsato et al. 2024), this system is unlikely to be lensed.

HerBS-162. The CO(1–0) emission traces two components to the southwest and northeast, separated by ∼7″, which were also detected in CO(3−2) and (4−3). They have slightly different redshifts of $z = 2.4739$ and 2.4742, respectively (P. Cox et al. 2023).

HerBS-183. This source is located at the western edge of a bright galaxy visible in HST F110W imaging (E. Borsato et al. 2024). The CO(1–0) emission line has a broad double-Gaussian profile that is similar to those of CO(2–1) and CO(4–3). The strong radio continuum at 35 GHz, with a flux density of 0.39 ± 0.02 mJy, is shifted to the east and aligned with the central region of the foreground galaxy, indicating that the continuum emission is most likely related to the lensing galaxy.

HerBS-187. Two sources separated by ∼4″, eastern and western, were detected in this field (P. Cox et al. 2023) in the CO(2–1) and (4−3) emission lines. They also detected an additional weaker southern source in the millimeter continuum. Of these, we only detect the western source in CO(1–0).

HerBS-188. This source displays a broad CO(1–0) emission line with a shape comparable to the CO(3−2) and CO(5−4) profiles (P. Cox et al. 2023). Interestingly, the strong radio continuum, with a flux density of 0.33 ± 0.03 mJy, is offset from the CO(1–0) peak by ∼3″. Although there is no visible galaxy seen in HST F110W imaging, the VLASS image shows a 3 GHz radio source in the foreground that is aligned with this line of sight.

HerBS-194. Of the two sources that were detected in CO(3−2) and CO(4−3), only the northern source with stronger CO emission lines is detected in CO(1–0). The southern source has an upper 3σ limit that is compatible with the finding that the CO(3−2) line flux is twice as weak as the northern source (P. Cox et al. 2023).

HerBS-204. This system is the only case in the z–GAL sample that shows two galaxies that are separated by ∼6″ and are linked by a bridge of matter, with all components detected in the dust continuum and the emission lines CO(4−3) and (5−4) (R. Neri et al. 2020; P. Cox et al. 2023). The total extent of this system is ∼45 kpc. The CO(1–0) emission line is clearly detected in both the eastern and western galaxies, with profiles that are comparable to the higher-J CO transitions. However, no CO(1–0) emission could be traced in the region in between the two galaxies.

B.4. Integrated-intensity (Moment-0) Maps and Spectra of CO(1–0) and CO(2−1) of the Vz-GAL DSFGs

Here, we provide an overview of all CO(1–0) and CO(2–1) integrated-intensity maps and spectra for the newly detected Vz-GAL DSFGs from this work. Sources in the HeLMS and HerS fields are shown in Figures 10 and 11, and those in the H-ATLAS fields are shown with their HerBS IDs in Figure 12. An overview of the pilot sources is shown in Figure 1 of F. Stanley et al. (2023).

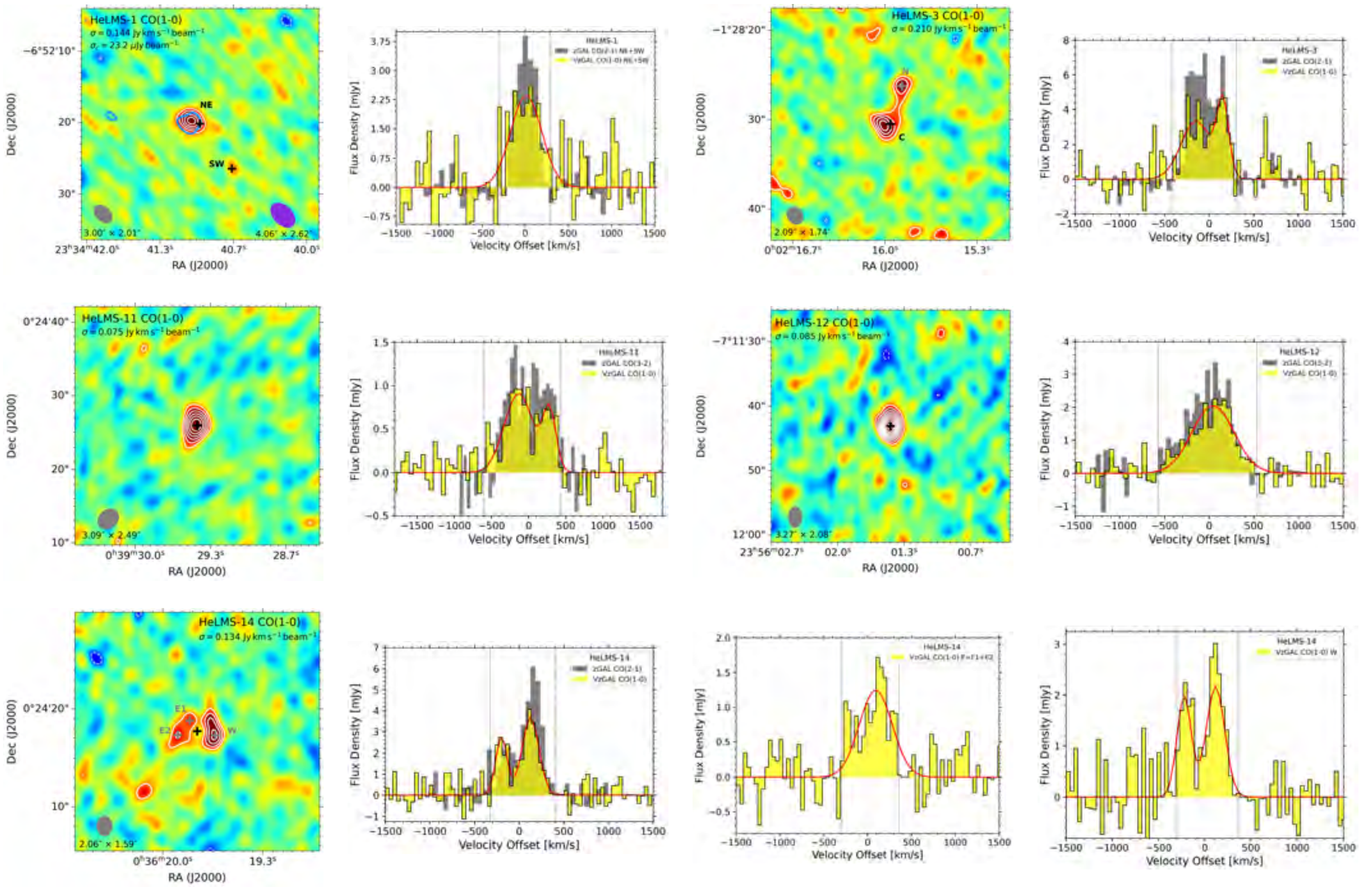

Figure 10. Moment-0 maps and spectra of low-*J* CO emission, namely CO(1–0) and CO(2–1), of the V*z*-GAL galaxies (HeLMS-1 to HeLMS-48 but HeLMS-47 here). We provide the rms noise (σ) of each moment-0 map along with the synthesized beam size (gray ellipses) in the image itself. For targets with lensed images or multiplicity, we distinctly add cross-markers identifying different spatial components on these moment-0 maps. Otherwise, the cross markers represent the central position of the DSFG as found in the *z*–GAL survey (P. Cox et al. 2023). The CO emission is shown using solid/dashed white (positive/negative) contours, starting at $\pm 2\sigma$. These contours vary in the steps of 1σ. For objects with detected continuum emission above $2\sigma_c$, we show continuum flux density levels as blue contours. In the cases where we detect a serendipitous radio source along the line of sight or in the field, we show its continuum with magenta contours instead. Please refer to Appendix A (Section A.2) for more details. The synthesized beam (purple ellipses) and noise level (σ_c) of continuum maps are depicted in the images. The extracted spectra of our CO(1–0) observations (see Section 3.2), depicted in yellow, are compared to higher-*J* CO lines shown in gray (P. Cox et al. 2023). For 10 V*z*-GAL DSFGs with additional CO(2–1) detection, we also present the CO(2–1) spectra alongside the CO(1–0) and higher-*J* CO lines. Each line spectra from V*z*-GAL detections is fitted with Gaussian profile(s) as red curves, with their fitting parameters shown in Appendix A (Tables 3 and 4). The spectra in gray are scaled to 1.5× the peak of the yellow spectrum. Black vertical dashed lines over the extracted spectra indicate the velocity range over which the moment-0 map of the CO line was integrated. Spectra of individual spatial components of lensed/multiple DSFGs are also depicted, wherever applicable.

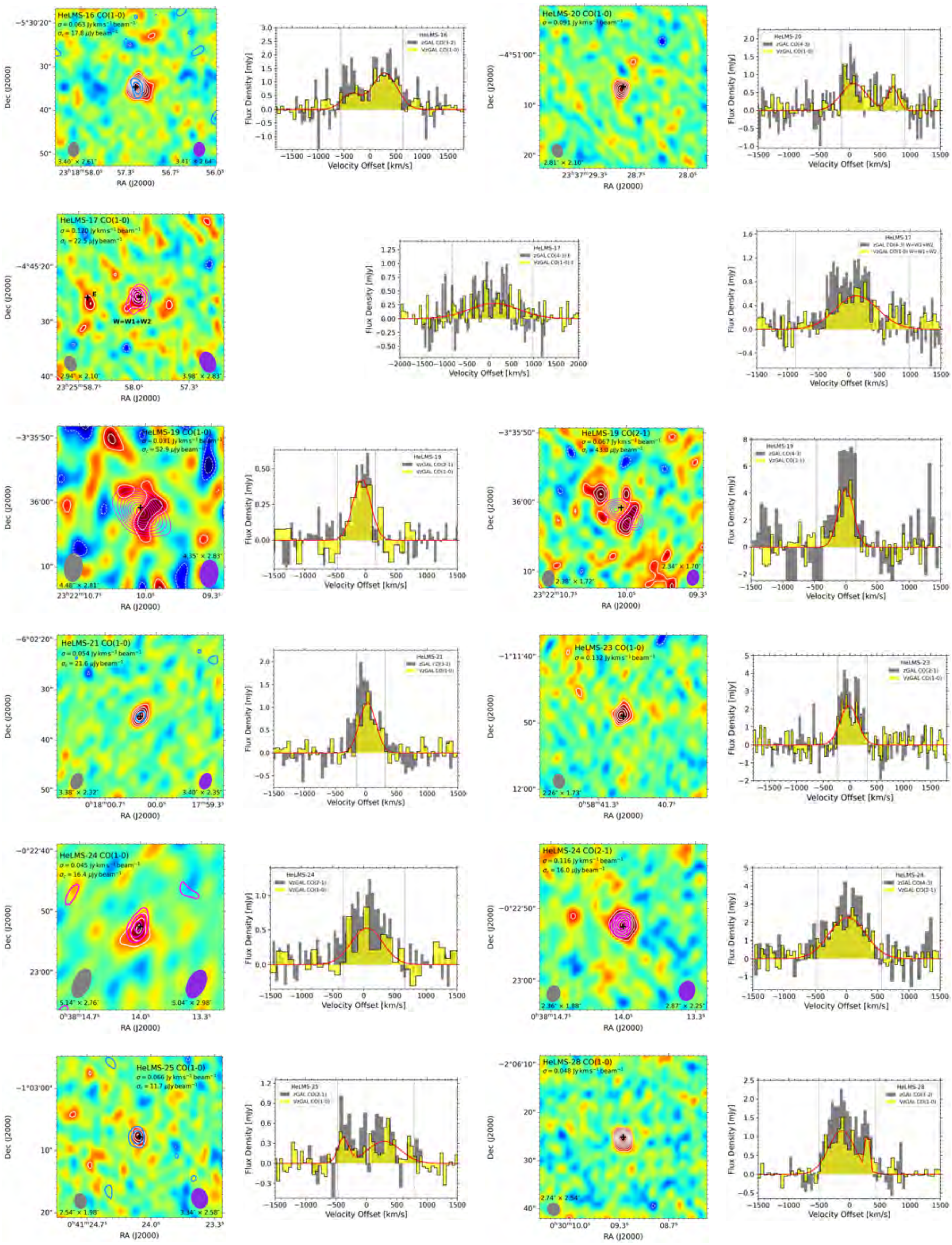

Figure 10. (Continued.)

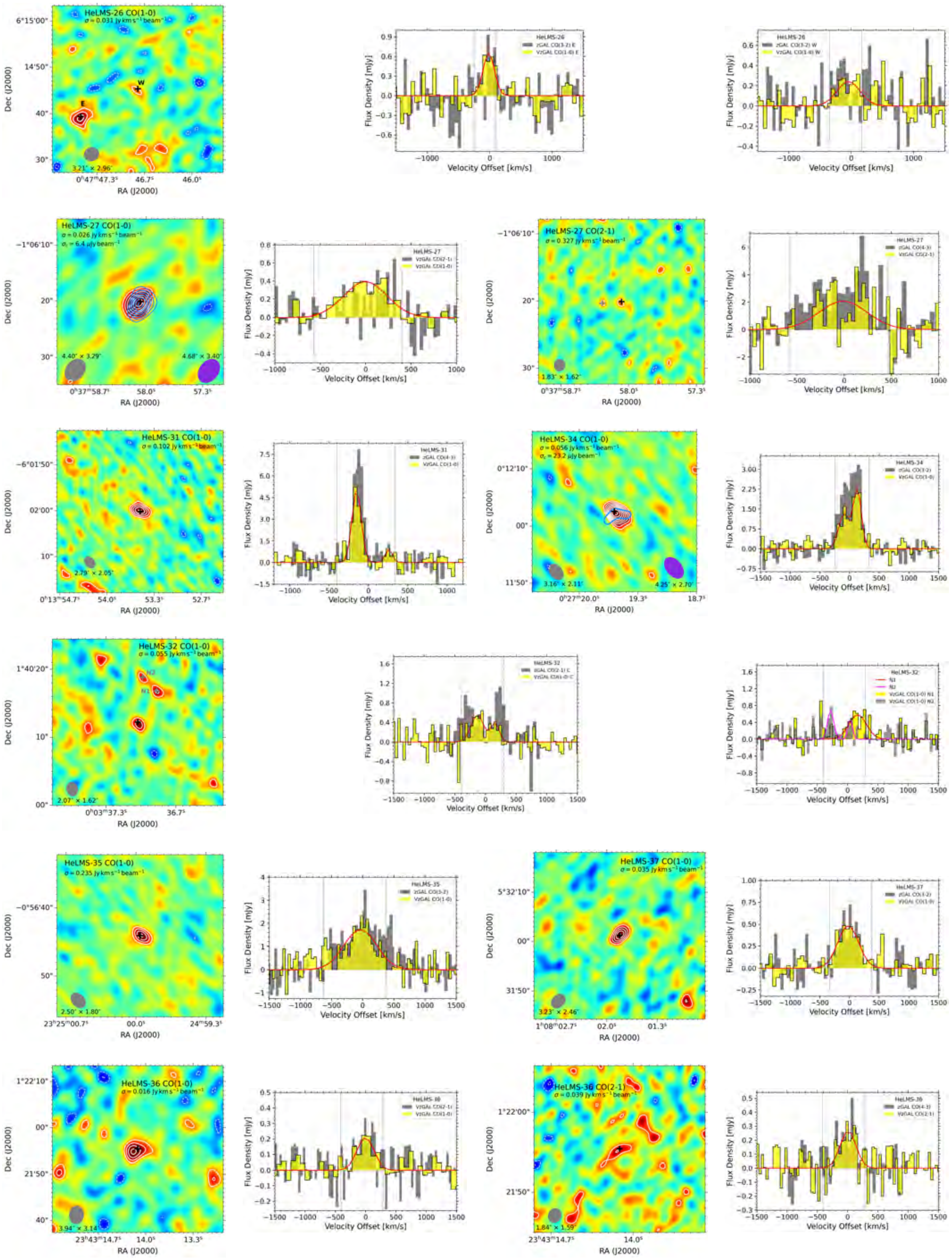

Figure 10. (Continued.)

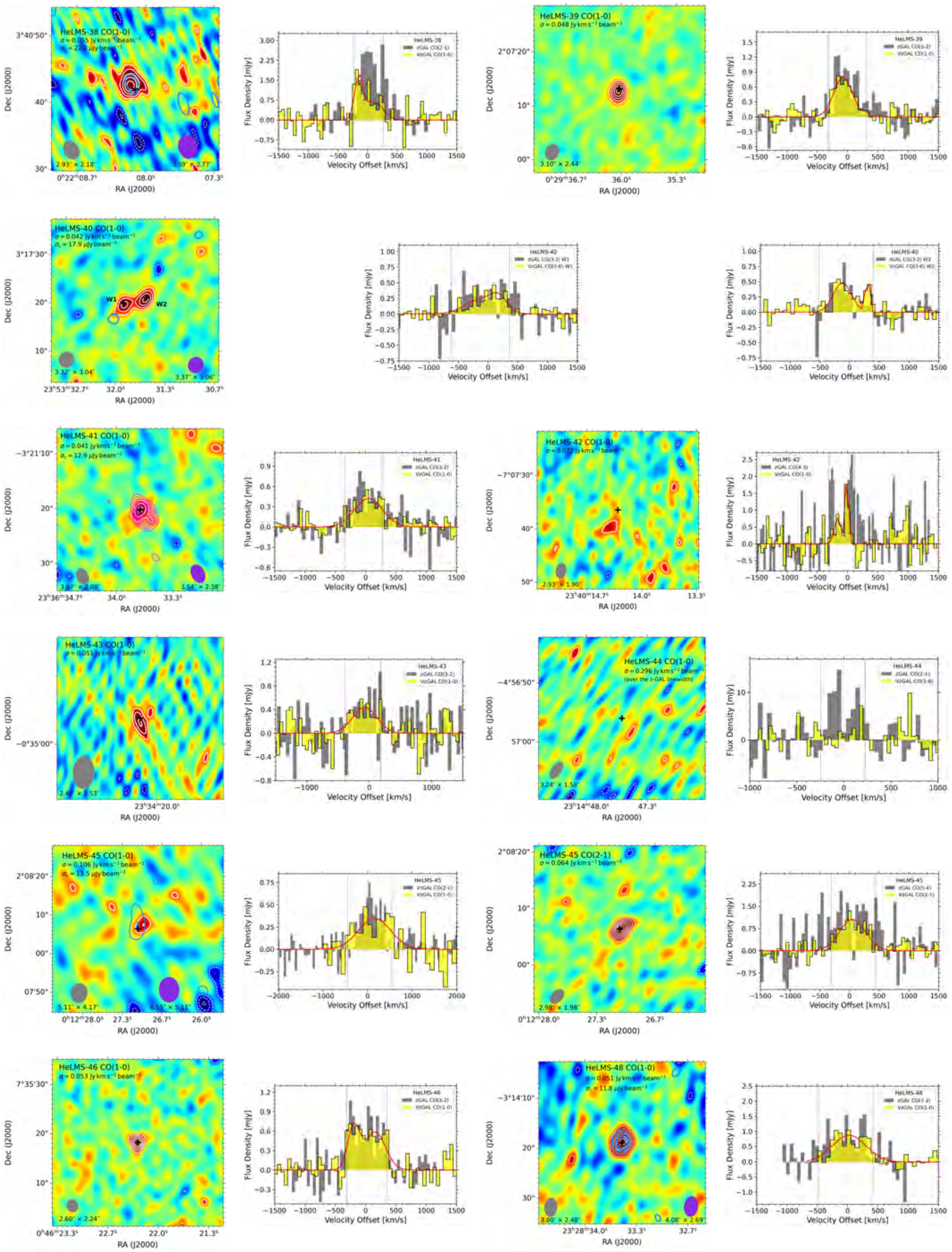

Figure 10. (Continued.)

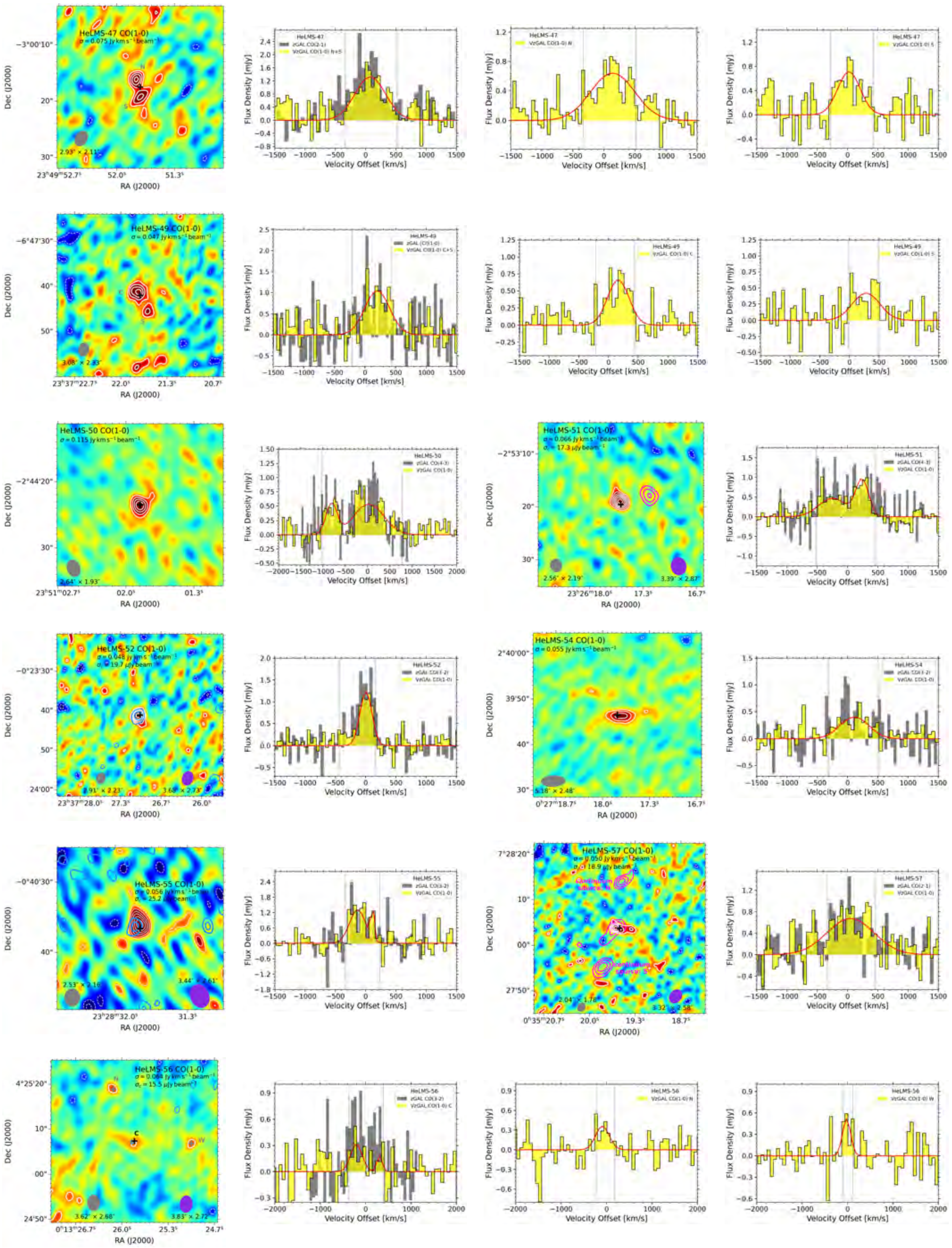

Figure 11. The same as Figure 10 with the remaining HeLMS sources (HeLMS-47 and HeLMS-49 to HeLMS-56) and all of the HerS galaxies.

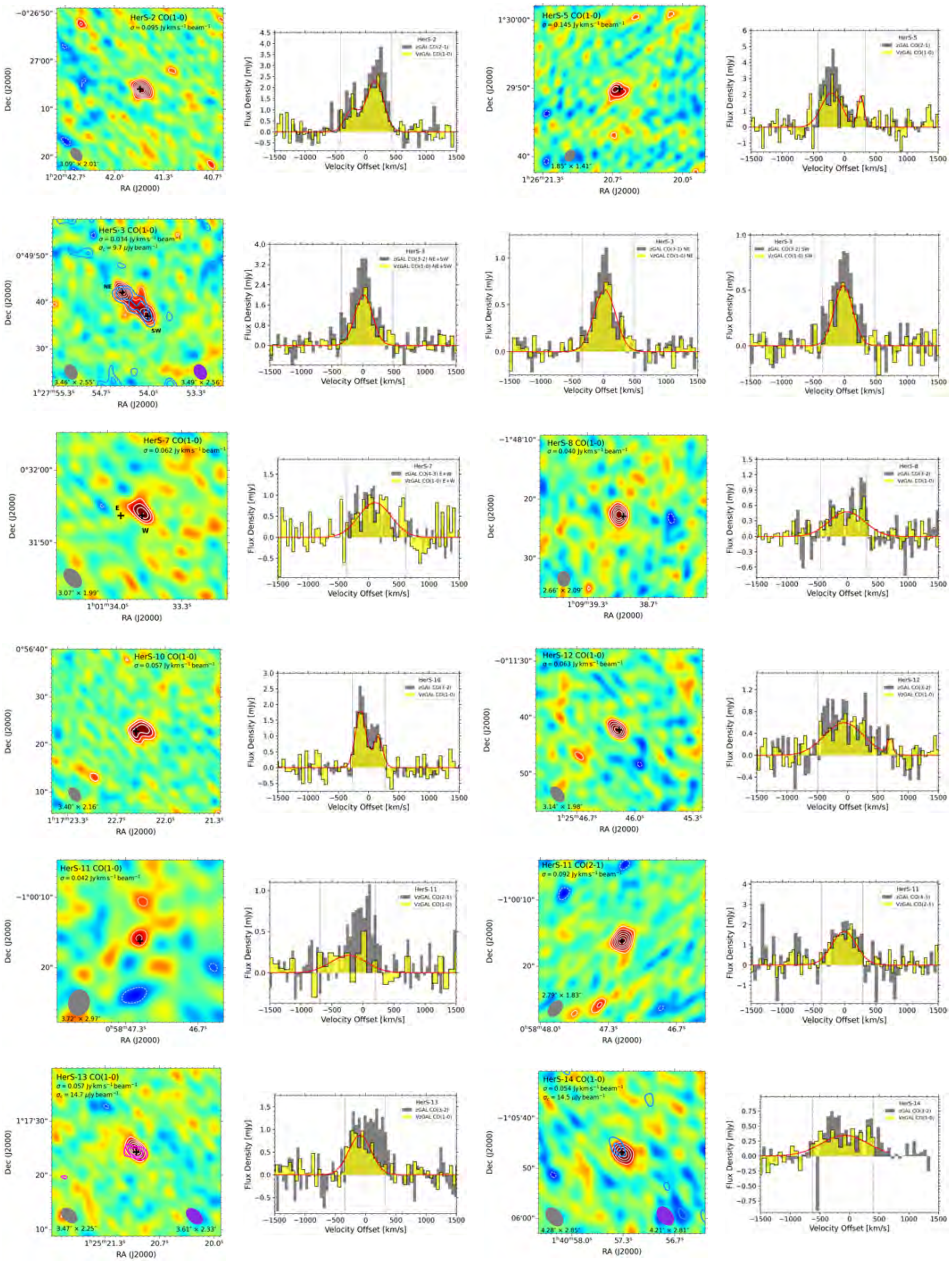

Figure 11. (Continued.)

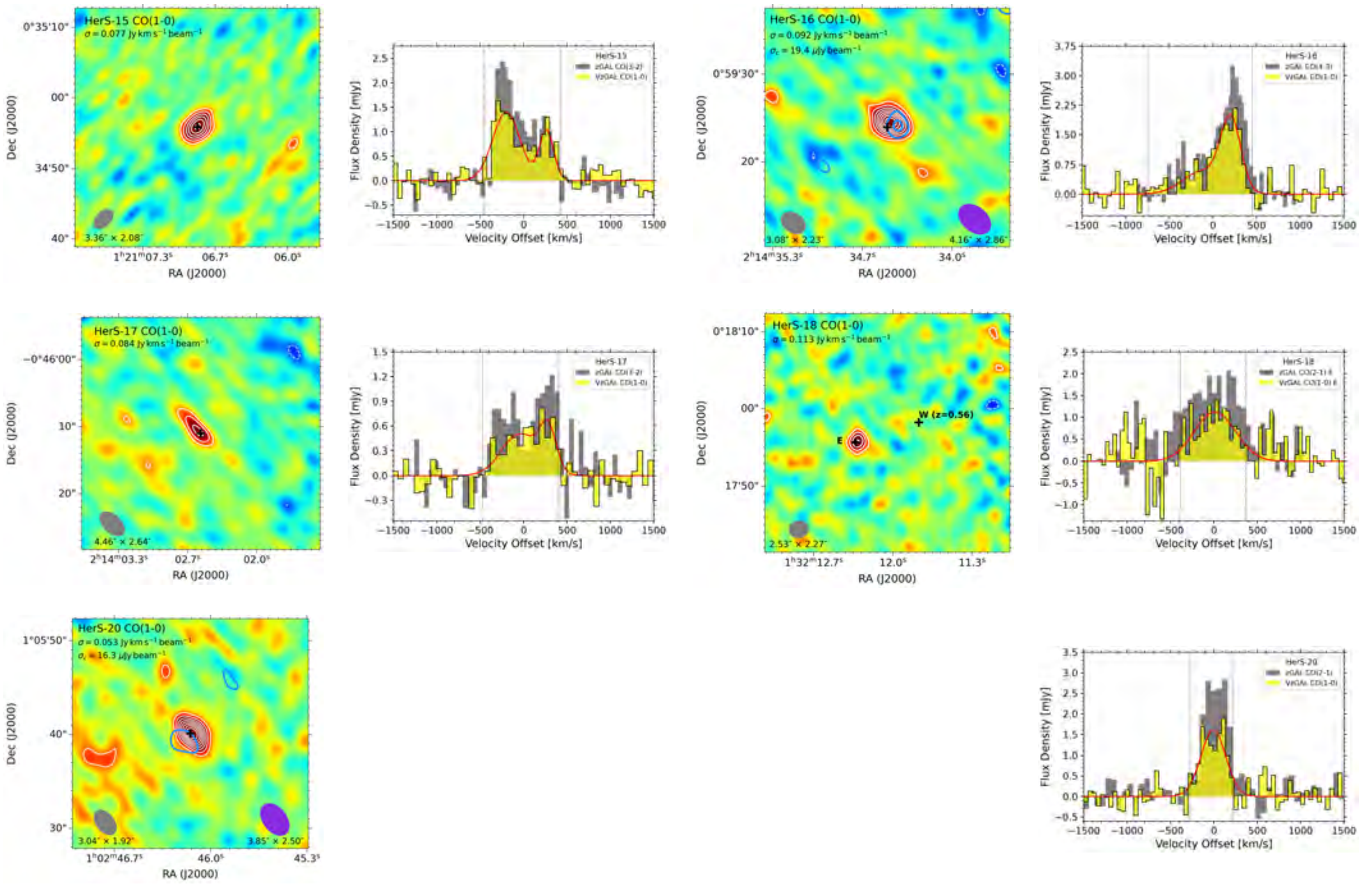

Figure 11. (Continued.)

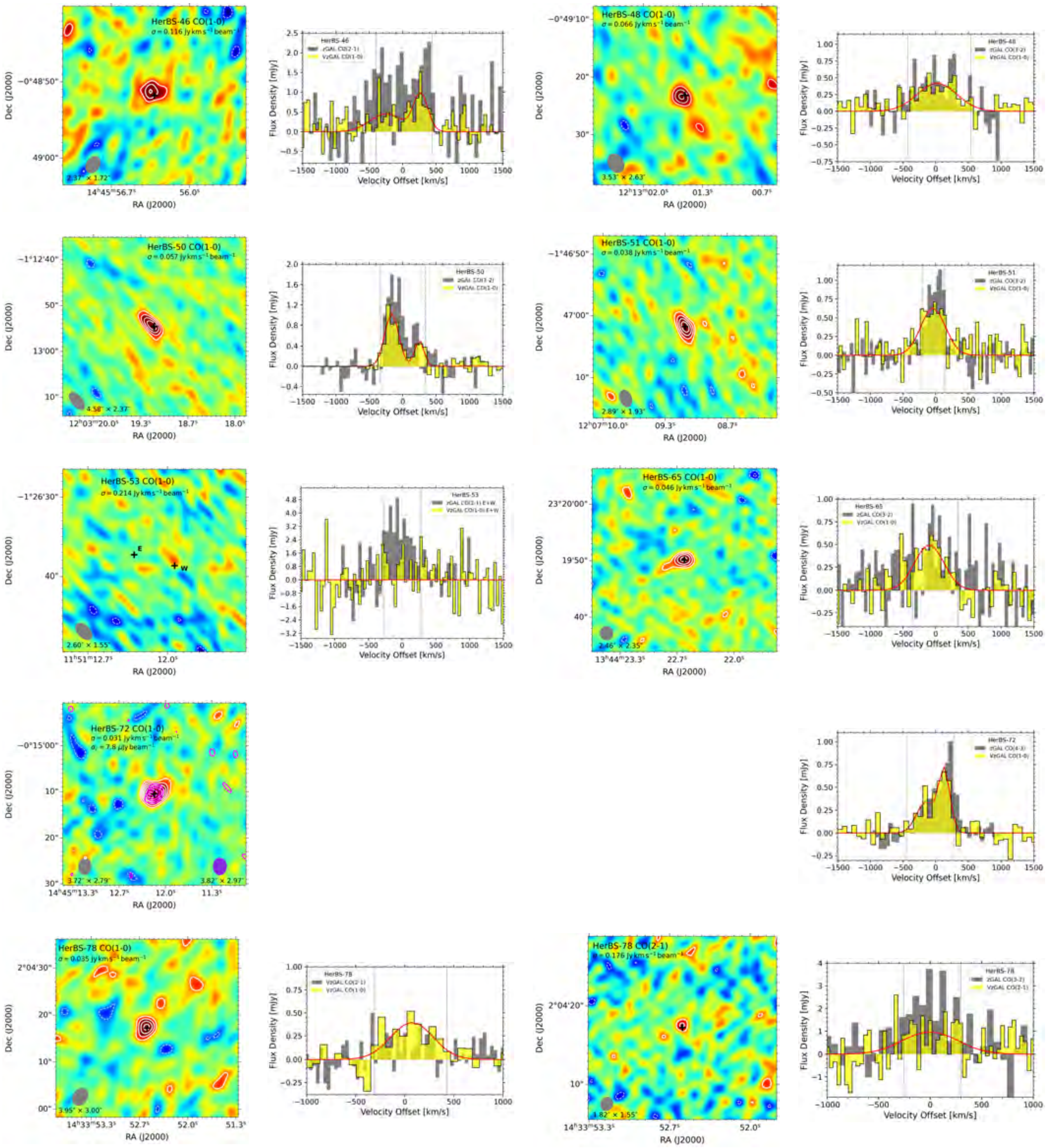

Figure 12. The same as Figure 10 with DSFGs from the HerBS fields.

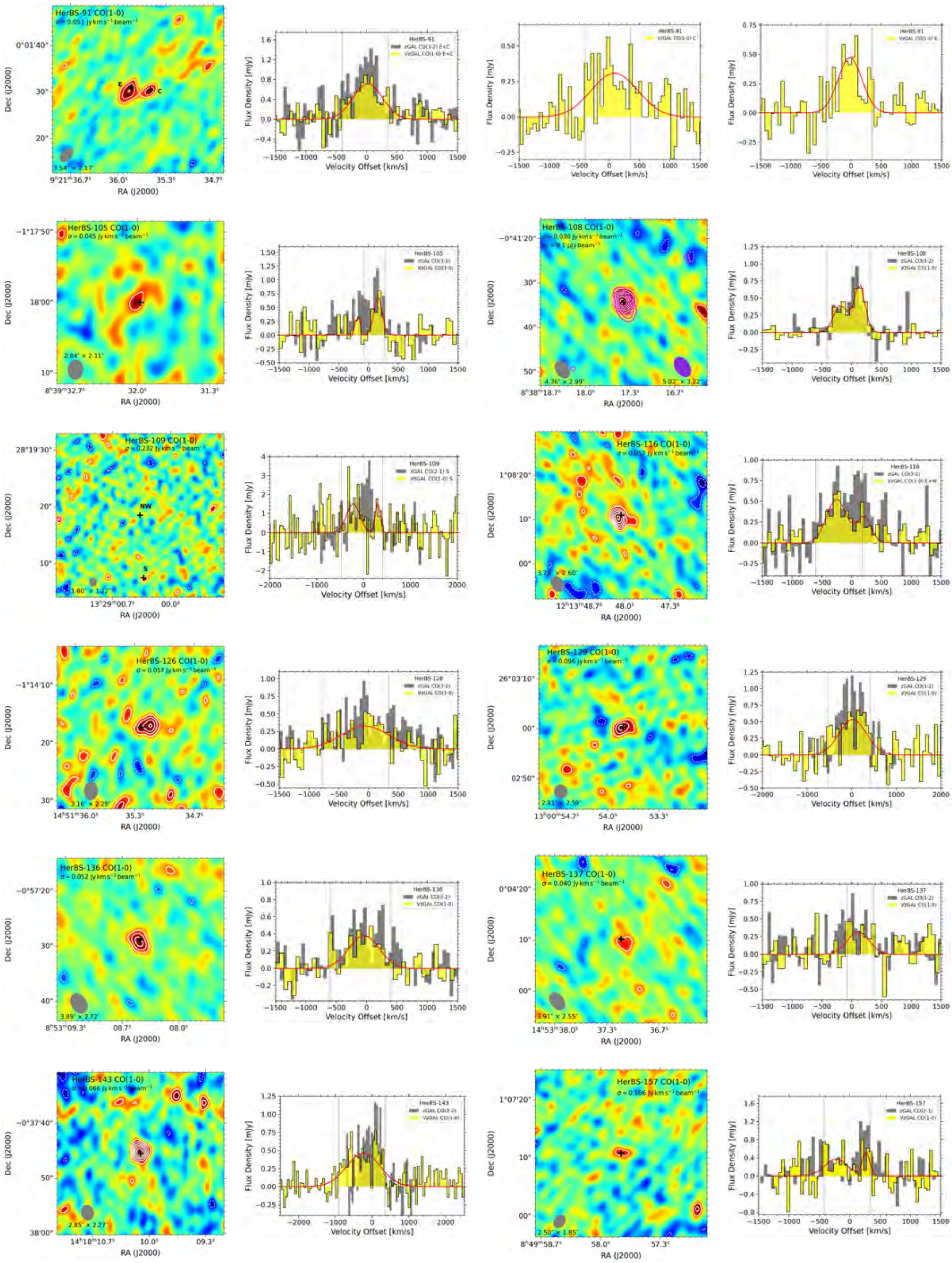

Figure 12. (Continued.)

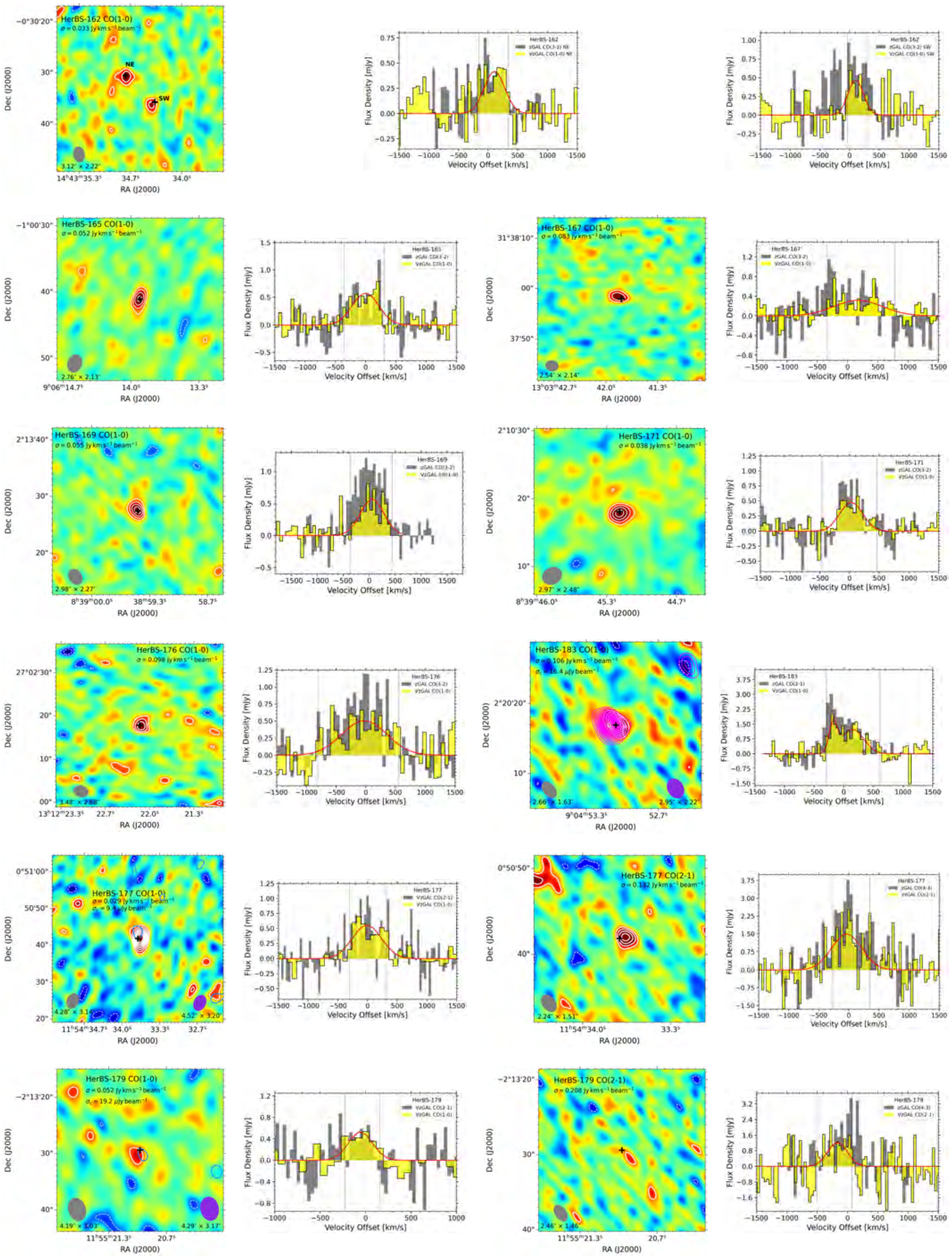

Figure 12. (Continued.)

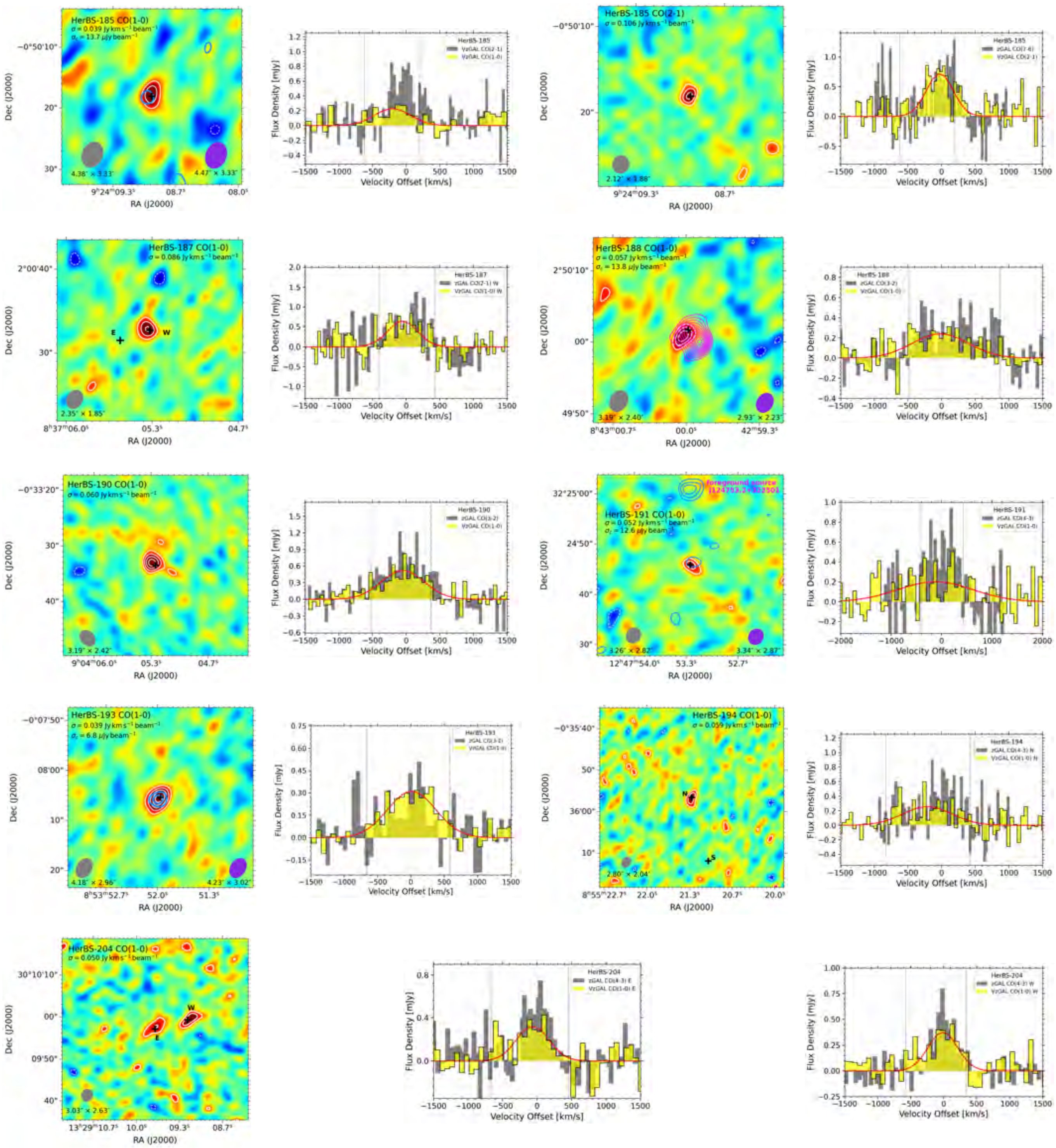

Figure 12. (Continued.)

ORCID iDs

Prachi Prajapati https://orcid.org/0000-0002-3094-1077
Dominik Riechers https://orcid.org/0000-0001-9585-1462
Pierre Cox https://orcid.org/0000-0003-2027-8221
Axel Weiss https://orcid.org/0000-0003-4678-3939
Amélie Saintonge https://orcid.org/0000-0003-4357-3450
Bethany Jones https://orcid.org/0000-0002-0675-0078
Tom J. L. C. Bakx https://orcid.org/0000-0002-5268-2221
Stefano Berta https://orcid.org/0000-0002-0320-1532
Paul van der Werf https://orcid.org/0000-0001-5434-5942
Roberto Neri https://orcid.org/0000-0002-7176-4046
Kirsty M. Butler https://orcid.org/0000-0001-7387-0558
Asantha Cooray https://orcid.org/0000-0002-3892-0190
Diana Ismail https://orcid.org/0009-0007-2281-4944
Andrew J. Baker https://orcid.org/0000-0002-7892-396X
Edoardo Borsato https://orcid.org/0009-0009-9483-8763
Andrew Harris https://orcid.org/0000-0001-6159-9174
Rob Ivison https://orcid.org/0000-0001-5118-1313
Matthew Lehnert https://orcid.org/0000-0003-1939-5885
Lucia Marchetti https://orcid.org/0000-0003-3948-7621
Hugo Messias https://orcid.org/0000-0002-2985-7994
Alain Omont https://orcid.org/0000-0002-4721-3922
Catherine Vlahakis https://orcid.org/0000-0003-3745-4228
Chentao Yang https://orcid.org/0000-0002-8117-9991

References

Agnello, A., Evans, N. W., & Romanowsky, A. J. 2014, MNRAS, 442, 3284
Alaghband-Zadeh, S., Chapman, S. C., Swinbank, A. M., et al. 2013, MNRAS, 435, 1493
Amvrosiadis, A., Eales, S. A., Negrello, M., et al. 2018, MNRAS, 475, 4939
Andreani, P., Casoli, F., & Gerin, M. 1995, A&A, 300, 43
Aravena, M., Bertoldi, F., Schinnerer, E., et al. 2008, A&A, 491, 173
Aravena, M., Carilli, C. L., Salvato, M., et al. 2012, MNRAS, 426, 258
Aravena, M., Hodge, J. A., Wagg, J., et al. 2014, MNRAS, 442, 558
Aravena, M., Spilker, J. S., Bethermin, M., et al. 2016, MNRAS, 457, 4406
Astropy Collaboration, Price-Whelan, A. M., Lim, P. L., et al. 2022, ApJ, 935, 167
Bakx, T. J. L. C., Berta, S., Dannerbauer, H., et al. 2024, MNRAS, 530, 4578
Bakx, T. J. L. C., Dannerbauer, H., Frayer, D., et al. 2020a, MNRAS, 496, 2372
Bakx, T. J. L. C., Eales, S., & Amvrosiadis, A. 2020b, MNRAS, 493, 4276
Bakx, T. J. L. C., Eales, S. A., Negrello, M., et al. 2018, MNRAS, 473, 1751
Berta, S., Stanley, F., Ismail, D., et al. 2023, A&A, 678, A28
Berta, S., Young, A. J., Cox, P., et al. 2021, A&A, 646, A122
Béthermin, M., Wang, L., Doré, O., et al. 2013, A&A, 557, A66
Blain, A. W., Smail, I., Ivison, R. J., Kneib, J. P., & Frayer, D. T. 2002, PhR, 369, 111
Bolatto, A. D., Wolfire, M., & Leroy, A. K. 2013, ARA&A, 51, 207
Borsato, E., Marchetti, L., Negrello, M., et al. 2024, MNRAS, 528, 6222
Bothwell, M. S., Smail, I., Chapman, S. C., et al. 2013, MNRAS, 429, 3047
Bourne, N., Dunlop, J. S., Merlin, E., et al. 2017, MNRAS, 470, 3249
Braine, J., & Combes, F. 1992, A&A, 264, 433
Bussmann, R. S., Pérez-Fournon, I., Amber, S., et al. 2013, ApJ, 779, 25
Bussmann, R. S., Riechers, D., Fialkov, A., et al. 2015, ApJ, 812, 43
Cañameras, R., Nesvadba, N. P. H., Guery, D., et al. 2015, A&A, 581, A105
Carilli, C. L., & Blain, A. W. 2002, ApJ, 569, 605
Carilli, C. L., Cox, P., Bertoldi, F., et al. 2002, ApJ, 575, 145
Carilli, C. L., Daddi, E., Riechers, D., et al. 2010, ApJ, 714, 1407
Carilli, C. L., & Walter, F. 2013, ARA&A, 51, 105
Carlstrom, J. E., Ade, P. A. R., Aird, K. A., et al. 2011, PASP, 123, 568
Carpenter, J., Brogan, C., Iono, D., Mroczkowski, T., Ossenkopf-Okada, V., et al. 2023, Physics and Chemistry of Star Formation: The Dynamical ISM Across Time and Spatial Scales, Proc. of the 7th Chile-Cologne-Bonn Symp. (Universitäts und Stadtbibliothekj Köln), 304
Casey, C. M., Narayanan, D., & Cooray, A. 2014, PhR, 541, 45
Chabrier, G. 2003, PASP, 115, 763
Chung, A., Narayanan, G., Yun, M. S., Heyer, M., & Erickson, N. R. 2009, AJ, 138, 858
Combes, F., García-Burillo, S., Braine, J., et al. 2011, A&A, 528, A124
Comrie, A., Wang, K.-S., Hwang, Y.-H., et al. 2024, CARTA: The Cube Analysis and Rendering Tool for Astronomy, v4.1.0, Zenodo, doi:10.5281/zenodo.15172686
Conley, A., Cooray, A., Vieira, J. D., et al. 2011, ApJL, 732, L35
Cox, P., Butler, K. M., Keeton, C. R., et al. 2025, ApJ, 991, 53
Cox, P., Neri, R., Berta, S., et al. 2023, A&A, 678, A26
da Cunha, E., Groves, B., Walter, F., et al. 2013, ApJ, 766, 13
Daddi, E., Elbaz, D., Walter, F., et al. 2010, ApJL, 714, L118
Danielson, A. L. R., Swinbank, A. M., Smail, I., et al. 2011, MNRAS, 410, 1687
Dannerbauer, H., Harrington, K., Díaz-SÃąnchez, A., et al. 2019, AJ, 158, 34
Decarli, R., Aravena, M., Boogaard, L., et al. 2020, ApJ, 902, 110
den Brok, J. S., Chatzigiannakis, D., Bigiel, F., et al. 2021, MNRAS, 504, 3221
Downes, D., & Solomon, P. M. 1998, ApJ, 507, 615
Draine, B. T., Aniano, G., Krause, O., et al. 2014, ApJ, 780, 172
Dunne, L., Maddox, S. J., Papadopoulos, P. P., Ivison, R. J., & Gomez, H. L. 2022, MNRAS, 517, 962
Dunne, L., Maddox, S. J., Vlahakis, C., & Gomez, H. L. 2021, MNRAS, 501, 2573
Eales, S., Dunne, L., Clements, D., et al. 2010, PASP, 122, 499
Emonts, B. H. C., Feain, I., Mao, M. Y., et al. 2011, ApJL, 734, L25
Emonts, B. H. C., Norris, R. P., Feain, I., et al. 2014, MNRAS, 438, 2898
Fixsen, D. J., Bennett, C. L., & Mather, J. C. 1999, ApJ, 526, 207
Förster Schreiber, N. M., Genzel, R., Bouché, N., et al. 2009, ApJ, 706, 1364
Frias Castillo, M., Hodge, J., Rybak, M., et al. 2023, ApJ, 945, 128
Frias Castillo, M., Rybak, M., Hodge, J. A., et al. 2025, ApJ, 987, 158
Fu, H., Cooray, A., Feruglio, C., et al. 2013, Natur, 498, 338
Gao, Y., & Solomon, P. M. 2004, ApJ, 606, 271
Geach, J. E., Smail, I., Moran, S. M., et al. 2011, ApJL, 730, L19
Genzel, R., Tacconi, L. J., Gracia-Carpio, J., et al. 2010, MNRAS, 407, 2091
Genzel, R., Tacconi, L. J., Lutz, D., et al. 2015, ApJ, 800, 20
Gómez-Guijarro, C., Riechers, D. A., Pavesi, R., et al. 2019, ApJ, 872, 117
Gowardhan, A., Spoon, H., Riechers, D. A., et al. 2018, ApJ, 859, 35
Graciá-Carpio, J., García-Burillo, S., Planesas, P., Fuente, A., & Usero, A. 2008, A&A, 479, 703
Greve, T. R., Bertoldi, F., Smail, I., et al. 2005, MNRAS, 359, 1165
Greve, T. R., Ivison, R. J., & Papadopoulos, P. P. 2004, A&A, 419, 99
Gururajan, G., Bethermin, M., Sulzenauer, N., et al. 2023, A&A, 676, A89
Hagimoto, M., Bakx, T. J. L. C., Serjeant, S., et al. 2023, MNRAS, 521, 5508
Harrington, K. C., Aranda, R. F., Boogaard, L., et al. 2025, A&A, 703, A216
Harrington, K. C., Vishwas, A., Weiß, A., et al. 2019, MNRAS, 488, 1489
Harrington, K. C., Weiss, A., Yun, M. S., et al. 2021, ApJ, 908, 95
Harrington, K. C., Yun, M. S., Magnelli, B., et al. 2017, MNRAS, 474, 3866
Harris, A. I., Baker, A. J., Frayer, D. T., et al. 2012, ApJ, 752, 152
Harris, A. I., Baker, A. J., Zonak, S. G., et al. 2010, ApJ, 723, 1139
Harris, C. R., Millman, K. J., van der Walt, S. J., et al. 2020, Natur, 585, 357
Hatsukade, B., Kohno, K., Yamaguchi, Y., et al. 2018, PASJ, 70, 105
Herrero-Illana, R., Privon, G. C., Evans, A. S., et al. 2019, A&A, 628, A71
Hodge, J. A., & da Cunha, E. 2020, RSOS, 7, 200556
Hughes, T. M., Ibar, E., Villanueva, V., et al. 2017, MNRAS, 468, L103
Hunter, J. D. 2007, CSE, 9, 90
Ismail, D., Beelen, A., Buat, V., et al. 2023, A&A, 678, A27
Israel, F. P., White, G. J., & Baas, F. 1995, A&A, 302, 343
Ivison, R. J., Papadopoulos, P. P., Smail, I., et al. 2011, MNRAS, 412, 1913
Ivison, R. J., Swinbank, A. M., Smail, I., et al. 2013, ApJ, 772, 137
Jin, S., Daddi, E., Magdis, G. E., et al. 2022, A&A, 665, A3
Kaasinen, M., Scoville, N., Walter, F., et al. 2019, ApJ, 880, 15
Keenan, R. P., Marrone, D. P., & Keating, G. K. 2025, ApJ, 991, 175
Kennicutt, R. C., Jr. 1989, ApJ, 344, 685
Kohno, M., & Sofue, Y. 2024, PASJ, 76, 579
Koyama, S., Koyama, Y., Yamashita, T., et al. 2017, ApJ, 847, 137
Lamperti, I., Saintonge, A., Koss, M., et al. 2020, ApJ, 889, 103
Leroy, A. K., Bolatto, A., Gordon, K., et al. 2011, ApJ, 737, 12
Leroy, A. K., Rosolowsky, E., Usero, A., et al. 2022, ApJ, 927, 149
Leroy, A. K., Walter, F., Sandstrom, K., et al. 2013, AJ, 146, 19
Lestrade, J.-F., Carilli, C. L., Thanjavur, K., et al. 2011, ApJL, 739, L30
Leung, T. K. D., Riechers, D. A., Baker, A. J., et al. 2019, ApJ, 871, 85
Lewis, G. F., Carilli, C., Papadopoulos, P., & Ivison, R. J. 2002, MNRAS, 330, L15
Liu, B., Chartab, N., Nayyeri, H., et al. 2022, ApJ, 929, 41
Liu, D., Schinnerer, E., Saito, T., et al. 2023, A&A, 672, A36
Lutz, D., Poglitsch, A., Altieri, B., et al. 2011, A&A, 532, A90
Madau, P., & Dickinson, M. 2014, ARA&A, 52, 415
Magdis, G. E., Daddi, E., Béthermin, M., et al. 2012, ApJ, 760, 6
Magnelli, B., Popesso, P., Berta, S., et al. 2013, A&A, 553, A132

McMullin, J. P., Waters, B., Schiebel, D., Young, W., & Golap, K. 2007, ASPC, 376, 127
Miller, T. B., Chapman, S. C., Aravena, M., et al. 2018, Natur, 556, 469
Montoya Arroyave, I., Cicone, C., Makroleivaditi, E., et al. 2023, A&A, 673, A13
Murphy, E. J., Bolatto, A., Chatterjee, S., et al. 2018, ASPC, 517, 3
Narayanan, D. 2011, arXiv:1112.1073
Narayanan, D., Bothwell, M., & Davé, R. 2012a, MNRAS, 426, 1178
Narayanan, D., Krumholz, M. R., Ostriker, E. C., & Hernquist, L. 2012b, MNRAS, 421, 3127
Nayyeri, H., Cooray, A. R., Calanog, J. A. B., et al. 2016a, AAS Meeting, 22, 346.02
Nayyeri, H., Keele, M., Cooray, A., et al. 2016b, ApJ, 823, 17
Negrello, M., Amber, S., Amvrosiadis, A., et al. 2017, MNRAS, 465, 3558
Negrello, M., Hopwood, R., De Zotti, G., et al. 2010, Sci, 330, 800
Neri, R., Cox, P., Omont, A., et al. 2020, A&A, 635, A7
Nesvadba, N. P. H., Cañameras, R., Kneissl, R., et al. 2019, A&A, 624, A23
Oliver, S. J., Bock, J., Altieri, B., et al. 2012, MNRAS, 424, 1614
Oteo, I., Ivison, R. J., Dunne, L., et al. 2016, ApJ, 827, 34
Oteo, I., Ivison, R. J., Dunne, L., et al. 2018, ApJ, 856, 72
Papadopoulos, P. P., & Greve, T. R. 2004, ApJL, 615, L29
Pérez-Beaupuits, J. P., Güsten, R., Harris, A., et al. 2018, ApJ, 860, 23
Perley, R. A., & Butler, B. J. 2017, ApJS, 230, 7
Pilbratt, G. L., Riedinger, J. R., Passvogel, T., et al. 2010, A&A, 518, L1
Planck Collaboration, Aghanim, N., Akrami, Y., et al. 2020, A&A, 641, A6
Planck Collaboration, Aghanim, N., Altieri, B., et al. 2015, A&A, 582, A30
Popping, G., Shivaei, I., Sanders, R. L., et al. 2023, A&A, 670, A138
Rémy-Ruyer, A., Madden, S. C., Galliano, F., et al. 2014, A&A, 563, A31
Reuter, C., Vieira, J. D., Spilker, J. S., et al. 2020, ApJ, 902, 78
Riechers, D. A. 2011, ApJ, 730, 108
Riechers, D. A., Boogaard, L. A., Decarli, R., et al. 2020, ApJL, 896, L21
Riechers, D. A., Bradford, C. M., Clements, D. L., et al. 2013, Natur, 496, 329
Riechers, D. A., Capak, P. L., Carilli, C. L., et al. 2010a, ApJL, 720, L131
Riechers, D. A., Carilli, C. L., Capak, P. L., et al. 2014, ApJ, 796, 84
Riechers, D. A., Carilli, C. L., Maddalena, R. J., et al. 2011a, ApJL, 739, L32
Riechers, D. A., Carilli, C. L., Walter, F., & Momjian, E. 2010b, ApJL, 724, L153
Riechers, D. A., Carilli, L. C., Walter, F., et al. 2011b, ApJL, 733, L11
Riechers, D. A., Cooray, A., Omont, A., et al. 2011c, ApJL, 733, L12
Riechers, D. A., Cooray, A., Pérez-Fournon, I., & Neri, R. 2021, ApJ, 913, 141
Riechers, D. A., Hodge, J., Walter, F., Carilli, C. L., & Bertoldi, F. 2011d, ApJL, 739, L31
Riechers, D. A., Leung, T. K. D., Ivison, R. J., et al. 2017, 850, 1
Riechers, D. A., Pavesi, R., Sharon, C. E., et al. 2019, ApJ, 872, 7
Riechers, D. A., Walter, F., Carilli, C. L., & Lewis, G. F. 2008, ApJ, 690, 463
Riechers, D. A., Walter, F., Carilli, C. L., & Lewis, G. F. 2009, ApJ, 690, 463
Riechers, D. A., Walter, F., Carilli, C. L., et al. 2006, ApJ, 650, 604
Riechers, D. A., Walter, F., Carilli, C. L., et al. 2011e, ApJ, 726, 50
Rosenberg, M. J. F., Kazandjian, M. V., van der Werf, P. P., et al. 2014, A&A, 564, A126
Rudnick, G., Hodge, J., Walter, F., et al. 2017, ApJ, 849, 27
Saintonge, A., & Catinella, B. 2022, ARA&A, 60, 319
Saintonge, A., Catinella, B., Tacconi, L. J., et al. 2017, ApJS, 233, 22
Sanders, D. B., & Mirabel, I. F. 1996, ARA&A, 34, 749
Sandstrom, K., Leroy, A. K., Kennicutt, R., KINGFISH Team, & HERACLES Team 2014, AAS Meeting, 223, 312.04
Schmidt, M. 1959, ApJ, 129, 243
Scott, K. S., Lupu, R. E., Aguirre, J. E., et al. 2011, ApJ, 733, 29
Scoville, N., Sheth, K., Aussel, H., et al. 2016, ApJ, 820, 83
Sharon, C. E., Baker, A. J., Harris, A. I., & Thomson, A. P. 2013, ApJ, 765, 6
Sharon, C. E., Baker, A. J., Harris, A. I., et al. 2015, ApJ, 798, 133
Sharon, C. E., Riechers, D. A., Hodge, J., et al. 2016, ApJ, 827, 18
Silverman, J. D., Rujopakarn, W., Daddi, E., et al. 2018, ApJ, 867, 92
Solomon, P. M., Downes, D., & Radford, S. J. E. 1992, ApJL, 387, L55
Solomon, P. M., Downes, D., Radford, S. J. E., & Barrett, J. W. 1997, ApJ, 478, 144
Spilker, J. S., Marrone, D. P., Aguirre, J. E., et al. 2014, ApJ, 785, 149
Spilker, J. S., Marrone, D. P., Aravena, M., et al. 2016, ApJ, 826, 112
Stanley, F., Jones, B. M., Riechers, D. A., et al. 2023, ApJ, 945, 24
Sulzenauer, N., Dannerbauer, H., Díaz-Sánchez, A., et al. 2021, ApJL, 923, L27
Sulzenauer, N., Weiß, A., Hill, R., et al. 2025, arXiv:2509.08035
Swinbank, A. M., Papadopoulos, P. P., Cox, P., et al. 2011, ApJ, 742, 11
Tacconi, L. J., Genzel, R., Smail, I., et al. 2008, ApJ, 680, 246
Tacconi, L. J., Genzel, R., & Sternberg, A. 2020, ARA&A, 58, 157
The pandas development team 2020, pandas-dev/pandas: Pandas, latest, v3.0.0rc1, Zenodo, doi:10.5281/zenodo.3509134
Thomson, A. P., Ivison, R. J., Smail, I., et al. 2012, MNRAS, 425, 2203
Urquhart, S. A., Bendo, G. J., Serjeant, S., et al. 2022, MNRAS, 511, 3017
Valentino, F., Daddi, E., Puglisi, A., et al. 2020, A&A, 641, A155
Valentino, F., Magdis, G. E., Daddi, E., et al. 2018, ApJ, 869, 27
Vieira, J. D., Crawford, T. M., Switzer, E. R., et al. 2010, ApJ, 719, 763
Viero, M. P., Asboth, V., Roseboom, I. G., et al. 2014, yCat, J/ApJS/210/22
Villanueva, V., Ibar, E., Hughes, T. M., et al. 2017, MNRAS, 470, 3775
Virtanen, P., Gommers, R., Oliphant, T. E., et al. 2020, NatMe, 17, 261
Wagg, J., Carilli, C. L., Wilner, D. J., et al. 2010, A&A, 519, L1
Walter, F., Carilli, C., Neeleman, M., et al. 2020, ApJ, 902, 111
Walter, F., Decarli, R., Carilli, C., et al. 2012, Natur, 486, 233
Walter, F., Weiß, A., Downes, D., Decarli, R., & Henkel, C. 2011, ApJ, 730, 18
Wang, T.-M., Magnelli, B., Schinnerer, E., et al. 2022, A&A, 660, A142
Ward, B. A., Eales, S. A., Pons, E., et al. 2022, MNRAS, 510, 2261
Wardlow, J. L., Cooray, A., De Bernardis, F., et al. 2013, ApJ, 762, 59
Weiß, A., De Breuck, C., Marrone, D. P., et al. 2013, ApJ, 767, 88
Weiß, A., Downes, D., Henkel, C., & Walter, F. 2005a, A&A, 429, L25
Weiß, A., Downes, D., Neri, R., et al. 2007, A&A, 467, 955
Weiß, A., Ivison, R. J., Downes, D., et al. 2009, ApJL, 705, L45
Weiß, A., Walter, F., & Scoville, N. Z. 2005b, A&A, 438, 533
Wilson, C. D. 1997, ApJL, 487, L49
Yang, C., Omont, A., Beelen, A., et al. 2017, A&A, 608, A144
Zavala, J. A., Casey, C. M., Manning, S. M., et al. 2021, ApJ, 909, 165
Zubko, V., Dwek, E., & Arendt, R. G. 2004, ApJS, 152, 211